METAMATERIAL AND METASURFACE LENSES FOR HIGH-RESOLUTION MICROWAVE IMAGING

By

Srijan Datta

A DISSERTATION

Submitted to
Michigan State University
in partial fulfillment of the requirements
for the degree of

Electrical Engineering – Doctor of Philosophy

2022

ABSTRACT

Metamaterials are engineered materials which consist of a periodic arrangement of subwavelength scatterers or unit cells, whose size is much smaller than wavelength λ of the incident electromagnetic (EM) wave. The effective EM properties of metamaterials depends on the design and arrangement of unit cells in contrast to material composition in atomic scale like that of conventional materials. Hence, they can be tailored to have specialized EM characteristics which are difficult or impossible to achieve with lenses made of conventional dielectric materials. A lens made of negative refractive index metamaterials can overcome the diffraction limited resolution of conventional lenses at far-field working distances. This dissertation focuses on the implementation of such metamaterial lenses for microwave nondestructive evaluation (NDE) applications.

In the first part of the dissertation, negative index metamaterial (NIM) lens design consisting of split-ring resonators (SRR) and thin wires unit cells is studied and implemented at two frequencies of operation in the microwave S and C bands. A novel NIM lens imaging sensor system using homodyne detection measurements is proposed in this work. Coherent homodyne detection scheme provides a simple, low-cost, and highly sensitive NIM lens imaging system that can be used in the field under practical conditions. Using the proposed sensor system, subwavelength focusing by negative refraction is verified experimentally at both frequencies of operation. Subwavelength focal spot of sizes 0.82λ and 0.65λ are obtained with the 3.5 GHz (S band) and 6.3 GHz (C band) designs respectively. Imaging resolution enhancement by a factor of 2.24 is obtained at a distance of 1.67λ with the C band lens design. The sensor system was further used to perform microwave NDE experiments of subwavelength defects inside Teflon and glass fiber reinforced (GFRP) composite samples. Defects comprising subwavelength hole of diameter

0.25λ and a groove of dimensions 0.17λ x 0.06λ placed at the focal plane of the lens was imaged both in the transmission and reflection mode using the proposed sensor system.

In the second part of the dissertation, an alternative approach using gradient index (GRIN) metasurface lens consisting of electric-LC (ELC) unit cells is studied. Metasurfaces are 2D counterparts of 3D metamaterials and provide an attractive alternative to metamaterials as they take less physical space and exhibit lower losses. Although GRIN lens operation is distinct from that of NIM lenses and does not rely on negative refraction, they offer various advantages including planar design, wideband operation, and no restrictions on source to focal plane distances. The design, simulation, and experimental validation of a GRIN metasurface lens operating at 8 GHz is reported in this dissertation. The proposed lens has an aperture of size 119 mm (3.2λ) x 119 mm (3.2λ) and thickness of only 0.6 mm (.016λ). The metasurface lens is designed and analyzed using full-wave finite element (FEM) solver. A prototype of the proposed GRIN metasurface lens was fabricated for experimental verification. A focal spot size of 1.1λ is achieved with the proposed GRIN lens with a resolution enhancement factor of 1.5 at a distance of 8.37λ. Microwave NDE imaging results of a defect of dimensions 0.4λ kept at the focal plane of the GRIN lens is also reported. The work is concluded by presenting a comparative discussion of the two approaches (NIM lens and GRIN lens) for high resolution microwave imaging along with remarks on the future direction of the work.

ACKNOWLEDGEMENTS

It is my pleasure to express my deepest gratitude to Prof. Lalita Udpa for being my advisor. Her invaluable guidance and endless support shaped my doctoral journey and I consider myself very lucky to have the opportunity to pursue my degree under her tutelage. I would also like to send my endless thanks to Prof. Yiming Deng for his constant support and inspiration in my pursuit of doctoral degree.

I would like to thank my committee members Prof. Premjeet Chahal, Prof. Satish Udpa and Prof. Mahmood Haq for reading the manuscript and providing insightful and valuable comments throughout my PhD work. Very special thanks to Prof. Edward Rothwell, from whom I have garnered invaluable wisdom and knowledge of electromagnetic theory, which helped me guide my PhD journey.

I would also like to thank my NDEL and Michigan State colleagues, who made graduate student life much more enjoyable and fun; Subrata Mukherjee, Xiaodong Shi, Xuhui Huang, Vivek Rathod, Anton Efremov, Mohand Alzuhiri, Deepak Kumar, Saptarshi Mukherjee, Bharath Basti Senoy, Zi Li, Oleksii Karpenko, Ciaron Hamilton, Rajendra Prasath, Fahres Alharbi and everyone else in NDEL. I am extremely lucky to be able to work with such a group and learn from them, which enriched this experience.

Finally, my eternal thanks to my parents, family, and friends, far away or nearby. Being in a new world so far from home, their constant love, support, and care was essential and critical to the successful completion of this journey and thank you all for being a part of my existence.

TABLE OF CONTENTS

INTRODUCTION

1.1 Motivation

Microwaves, occupying 300 MHz to 300 GHz of the electromagnetic (EM) spectrum, are widely used in a variety of imaging and sensing applications due to their ability to penetrate non-conducting or dielectric materials. The fundamental principle of operation of microwave imaging involves illuminating the test object by microwaves and capturing the scattered signal. Embedded anomalies or defects will perturb the scattered signals owing to their contrasting EM properties relative to that of surrounding dielectric material. The captured microwave signals are processed to infer information about the anomalies and image them. Biomedical imaging for cancer cell detection [1][2], ground penetrating and remote sensing for geological objects [3][4], security screening for concealed weapons detection [5] , structural health monitoring [6] and nondestructive testing [7][8] are some of the applications of microwave imaging.

Microwave imaging can be implemented in far-field and near-field modes depending on the distance between the source and test object. Near-field imaging sensors such as near-field scanning microwave microscopy depend strongly on the near-field interaction between source and the test object [9][10]. Near-field sensors can sample remnant evanescent waves containing higher spatial frequency information, thus allowing for high resolution images. However, the probe stand-off distance is generally limited to the order of $\lambda/10$, where λ is the operating wavelength [11]. Far-field imaging is typically done by synthetic aperture radar (SAR) [12] or focusing lens systems [13]. SAR implementation involves complex reconstruction algorithms to solve the nonlinear inverse problem and retrieve image content from scattering effects [14]. This leads to information loss and heavy computational processing of data. Imaging with focusing lens systems removes the

need to for computational processing. However far-field imaging resolution using lenses is diffraction limited since a conventional lens cannot focus waves onto an area smaller than square λ^2. The evanescent wave components of the scattered field, which contain the high-resolution information about an object, decay exponentially with distance from the test object. Hence, far-field sensors are ineffective in imaging subwavelength objects. Fig 1-1 shows the schematic of typical near-field and far-field microwave NDE setups. In near-field NDE, the probe is placed in close proximity (~$\lambda/10$) to the sample under test (Figure 1-1a). Far-field imaging methods instead use a lens to focus the transmitted waves on the sample under test (Figure 1-1b). Near-field and far-field microwave NDE imaging results of a Glass Fiber Reinforced (GFRP) composite sample with drilled holes of varying sizes (diameters of $\lambda/4$, $\lambda/7$ and $\lambda/15$ respectively) are presented in Figure 1-1c to demonstrate the diffraction limited resolution of far-field imaging [15], [16]. It is observed that all the three drilled holes can be imaged using near-field sensor. However, the far-field NDE results indicate that the largest hole is detected clearly, while the smallest hole with a dimension of $\lambda/15$ cannot be detected due to the diffraction limit.

These limitations motivate the development of metamaterial lenses, which hold significant promise to bridge the gap between stand-off distance limited near-field imaging and diffraction-limited far-field imaging. Lenses made of negative index metamaterials (NIM) can potentially bridge the gap between the two imaging modes by providing subwavelength resolution beyond the diffraction limit at far-field working distances. This dissertation investigates the feasibility of using such metamaterials lenses to enhance the resolution of far-field microwave imaging beyond their inherent diffraction limits for nondestructive evaluation (NDE) applications. The concept of NIM can be extended to graded metamaterials and metasurfaces, whose effective electromagnetic properties vary spatially by introducing a slight change in the properties of each successive unit

cell. The second part of the dissertation reports the design and experimental validation of such a GRIN metasurface lens. Although the proposed GRIN metasurface lenses do not provide sub-diffraction imaging resolution, they offer several other advantages over NIM lenses such as high resolution from greater working distances. Research on both the methodologies is undertaken with a view to provide a holistic discussion on the subject of metamaterials and metasurfaces for high resolution microwave imaging.

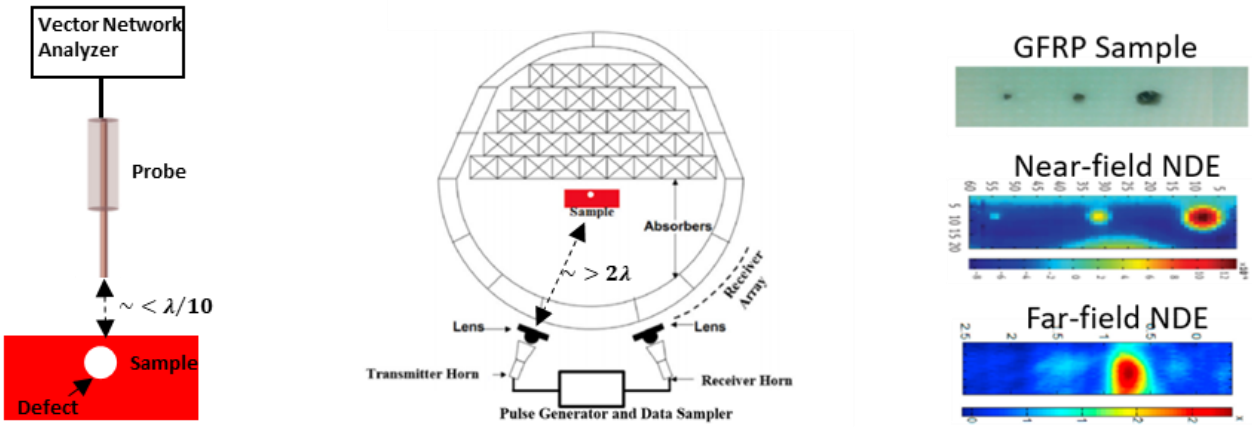

(a) (b) (c)

Figure 0-1 (a) Near-field microwave NDE schematic (b) Far-field microwave NDE schematic (c) Comparison of near-field and far-field NDE imaging results on a GFRP composite sample.

1.2 Research Scope

This research focuses on the design and evaluation of metamaterial lenses for enhancing the diffraction-limited resolution of far-field imaging so that subwavelength objects can be detected in the far-field at large stand-off distances. A novel NIM lens imaging sensor system using homodyne measurements is proposed in this dissertation. Idea of negative refractive index materials was discussed as early as beginning of the 20th century when Schuster showed that negative refraction takes place at the boundary of two media, one supporting a forward wave and the other one a backward waves [17]. Present-day research in metamaterials was stimulated by the theoretical work of Veselago et al. in the 1950s [18][19][20] and later by the realization of

engineered metamaterials by Smith et al. at the turn of the century [21]–[24]. Since then, metamaterials have been extensively researched as means of controlling the propagation of EM waves ranging from microwave to optical frequencies [25]. Pendry showed theoretically in [26] that a slab made of negative index metamaterials (NIM) can act as a "perfect lens" for a diverging source as both the propagating and evanescent wave components of the EM field will contribute to the resolution of the image. Although losses associated with engineered metamaterials makes it impossible to realize perfect lensing conditions [27][28], sub-diffraction imaging using NIM lenses is still achievable as shown by various studies [29]–[32].

While numerical studies of NIM lenses in the far field have been undertaken [33][34][33][35], the practical feasibility of their use as imaging sensors has not been widely demonstrated. Existing literature on using metamaterials for microwave NDE has mostly involved metamaterial inspired structures for near field sensing applications[36]–[43]. One prior study on using NIM lenses for far-field microwave NDE was done by Shreiber et al., where they presented the detection of subwavelength defects at a working distance of 1.9λ [44]. However, the NDE measurements was performed using a Vector Network Analyzer (VNA) in a semi-anechoic environment, which may not be practical for industrial implementation. The NIM lens was embedded in microwave absorbers to isolate the transmitter and receiver. Moreover, high frequency amplifiers were required since the directivity of diverging sources is weak and engineered NIM lenses are highly dispersive structures. This research proposes a novel system using homodyne measurement techniques with NIM lenses to provide a NDE imaging sensor that can be used in the field. The high SNR and preservation of phase information associated with such synchronous detection allows the lens to be characterized in free space and, hence, provides a system that can be used in the field under practical conditions [45].

Major part of the dissertation focuses on the design and implementation of the novel NIM lens sensor system for subwavelength microwave imaging applications. An SRR-wire unit cell based design of NIM lens is studied and implemented at two frequencies of operation in the microwave S and C band. A focal spot of dimension 0.82λ is obtained with the 3.5 GHz lens (S band). Subwavelength defect of dimension 0.17λ x 0.06λ in Teflon are shown to be detected by the sensor system. Consecutive positions of the defect with a separation of 0.23λ was resolvable using the proposed S band system. Additional imaging experiments were performed with the NIM lens operating at 6.3 GHz (C band) to determine the resolution enhancement. A focal spot of size 0.62λ is obtained for the C band lens design. Reflection mode imaging results of a subwavelength hole of diameter 0.25λ in GFRP sample and a groove of dimensions 0.31λ x 0.1λ in a Teflon sample are reported using the proposed NDE sensor system at 6.3 GHz.

Although the initial overwhelming research interest in metamaterials lied in the realization of negative refraction, which can provide sub-diffraction imaging capabilities at working distances beyond the near field, realizing them in practice is difficult due to the high losses and strong dispersion associated with the resonant responses of NIM lenses. The concept of 3D bulk metamaterials was judiciously extended to 2D metasurfaces, which consists of subwavelength unit cell placed on a surface or an interface. Planar metamaterials or metasurfaces takes less physical space than bulk metamaterials, exhibits lower losses and can be easily integrated into sensor systems due to its thin profile. And after it was shown in 2005 that metamaterials whose effective EM properties vary spatially can also be fabricated by introducing a slight change in the properties of each successive unit cell, research on metamaterials was no longer limited to realizing negative refraction.

Therefore, the last part of the dissertation investigates the use of such graded metasurfaces as alternatives for high resolution microwave imaging. The physics, design and implementation of GRIN metasurface lenses working at 8 GHz is discussed. Even though GRIN lenses do not offer sub-diffraction imaging resolution, they can still provide high resolution microwave imaging at much greater working distances. In this research work, a focal spot size of 0.65λ was obtained at a distance of 1.67λ for a NIM lens whereas a focal spot size of 0.88λ is achieved with a GRIN lens at a distance of 8.26λ. The NIM lens requires 31 PCB layers in contrast to the GRIN metasurface lens which can be implemented using a single PCB layer. Thus, GRIN lens provides a low-cost, low-profile, and lightweight solution to the high resolution microwave imaging problem and is explored in this work as an alternative approach.

Chapter 2 provides a brief theoretical discussion on the fundamental limits of microwave imaging resolution and the electrodynamics of negative index metamaterials. This is followed by a literature review of pioneering research works on experimental implementation of NIM structures. The operating principle of NIM lenses and how they can provide subwavelength focusing beyond the diffraction limited resolution is discussed in Chapter 2.

Chapter 3 presents the study of an S band NIM lens operating at 3.5 GHz. Numerical results of the proposed unit cell design obtained using commercial FEM solver Ansys HFSS is reported. A NIM lens consisting of 20x10x31 of the proposed unit cells was fabricated for experimental validation. A homodyne detection architecture was used to demonstrate negative refractive index behavior of the fabricated lens. Chapter 3 concludes with NDE results of subwavelength defects in Teflon test objects.

Chapter 4 reports the study of a C band NIM lens design operating at 6.3 GHz. The lens design is similar to the preceding chapter but scaled to work at a higher frequency. The resolution

of the lenses are dependent on the operating wavelength. Therefore, a shorter wavelength design is considered in this chapter to demonstrate the scalability of the NIM lens designs for detection of smaller defects. Source and subwavelength defect imaging with and without the proposed lens is presented to demonstrate the resolution enhancement using NIM lenses. Finally, using the C band NIM lens, novel reflection mode imaging results for microwave NDE of subwavelength defects is presented. Reflection mode imaging provides a practical system that can be used in the field, where single side access to the sample under test is more likely to occur.

Chapter 5 presents the alternative thin metamaterial (metasurface) lens design for enhancing the far-field microwave imaging resolution. The operating principle of the lens is based on GRIN optics, where a spatially varying refractive index is used to focus incident plane waves. Theory of the unit cell design and GRIN optics is discussed in this chapter. Numerical study of the focusing action of the GRIN metasurface lens is presented along with experimental verification with fabricated prototypes. Initial microwave NDE imaging results are also presented at the end of Chapter 5.

Chapter 6 provides a summary of the report. Concluding remarks are presented followed by the novel contributions of this research. A discussion on the future work of the research is also stated at the end.

1.3 Fundamental limits on microwave imaging

Microwave imaging can be implemented in two modalities, namely, the near-field and the far-field imaging. Non-propagating reactive fields dominate in the near-field region while propagating EM radiation dominates in the far-field region. The demarcation of the spatial field regions is subjective as there is no precisely defined cutoff between the two regions and the field components of the regions overlap. In study of antenna design, the Fraunhofer distance d_F, given by (0.1), is typically taken as the limit between the near-field and far-field.

$$d_F = \frac{2D^2}{\lambda} \tag{0.1}$$

where, D is the largest dimension of the radiator and λ is the operating wavelength. In order to understand the diffraction limit of far-field systems, consider a wave of frequency ω travelling along the $+z$ direction. The E component of the field can be defined as a superposition of elementary plane waves given by the equation

$$E(x, y, z; t) = \sum_{k_x k_y} A(k_x, k_y) e^{j(k_x x + k_y y + k_z z - \omega t)} \tag{0.2}$$

where, A is the amplitude of the wave, $k_z = \sqrt{\frac{\omega^2}{c^2} - k_x^2 - k_y^2}$ is the wave number in direction of propagation and c is the speed of light. For transverse wave numbers $k_x^2 + k_y^2 < \frac{\omega^2}{c^2}$, k_z is real, leading to propagating waves in the z direction. However, for larger values of transverse wave numbers, corresponding to high spatial frequency, i.e. $(k_x^2 + k_y^2 > \frac{\omega^2}{c^2})$, k_z is imaginary leading to non-propagating evanescent waves. These evanescent waves, containing the higher

spatial frequency information, attenuate exponentially with distance from the scattering object. The evanescent wave spectrum of the object is removed from images in the far-field, which generally comprise of the propagating waves only. Since propagating waves are limited to $k_x^2 + k_y^2 < \frac{\omega^2}{c^2}$, the maximum resolution in the far-field image Δ_F is given by

$$\Delta_F \approx \frac{2\pi}{k_{max}} = \frac{2\pi c}{\omega} = \lambda \tag{0.3}$$

and the diffraction limit manifests itself as an image smeared over an area of approximately one wavelength in diameter [26]. Therefore, subwavelength objects are not resolvable using far-field imaging systems.

Near imaging can be done to overcome the diffraction limited resolution of far-field systems by sampling the evanescent waves. The spatial resolution of evanescent waves from the object directly determine the resolution limit in near field imaging systems. Since the spatial resolution of the evanescent waves cannot be smaller than the smallest feature size ρ_N of the near-field imaging probe, near field imaging resolution is in the order of ρ_N and is given by

$$\Delta_N \sim \rho_N \tag{0.4}$$

Furthermore, evanescent waves decay exponentially with stand-off distance from the object. Due to these stringent requirements, the near-field probe size and stand-off distance must be considerably less than λ to break the diffraction limit.

1.4 Metamaterials theory and literature review

Metamaterials, by virtue of their negative refractive index, can help to mitigate the constraints posed by diffraction limits on resolution of microwave imaging, by allowing subwavelength resolution in far-field. The EM theory of NIMs and the application of effective medium theory in engineering such structures is briefly discussed in this section followed by a

literature review on pioneering research works involving characterization and demonstration of NIM structures.

1.4.1 EM properties of Negative Index Metamaterials

In 1968, V. Veselago theoretically introduced the electrodynamics of materials having simultaneous negative values of permittivity ϵ and permeability μ [18]. He showed that such materials will exhibit unusual properties such as negative refraction, reversal of Doppler shift and backward Cherenkov radiation. The electric field, magnetic field, and wave vector of a plane wave form a left-handed triplet in such a medium, instead of the conventional right-handed one. The word "metamaterial" was coined for such materials, alluding to their unusual properties, not generally encountered in nature.

To understand the electrodynamics of materials with simultaneous negative ϵ and μ, consider the Maxwell equations and the constituent relations,

$$\begin{aligned} \vec{\nabla} \times \vec{E} &= -\frac{1}{c}\frac{\partial \vec{B}}{\partial t} \\ \vec{\nabla} \times \vec{B} &= \frac{1}{c}\frac{\partial \vec{D}}{\partial t} \\ \vec{B} &= \mu \vec{H} \\ \vec{D} &= \epsilon \vec{E} \end{aligned} \tag{0.5}$$

Where $\vec{D}$ is the displacement field and $\vec{H}$ is the magnetizing field. For a plane monochromatic wave of frequency ω travelling in z direction, in which all quantities are proportional to $e^{j(k_z - \omega t)}$, where k_z is the wavenumber in direction of propagation, the Maxwell's equations reduce to

$$\vec{k} \times \vec{E} = \frac{\omega}{c}\mu \vec{H}$$

$$\vec{k} \times \vec{H} = -\frac{\omega}{c}\epsilon\vec{E} \tag{0.6}$$

It can be immediately seen from (2.6) that the vectors $\vec{k}$, $\vec{E}$ and $\vec{H}$ form the conventional right-handed triplet for positive values of μ and ϵ, but a left-handed one for negative μ and ϵ. For this reason, NIMs are often termed as Left-Handed Materials (LHMs).

The Poynting vector $\vec{S}$, representing the direction of power flow of the EM field, always form a right-handed triplet with the vectors $\vec{E}$ and $\vec{H}$ and is given by,

$$\vec{S} = \vec{E} \times \vec{H} \tag{0.7}$$

The direction of phase velocity $\vec{v}_{ph}$ of an EM wave coincides with the direction of wave vector $\vec{k}$ while the direction of group velocity $\vec{v}_g$ coincides with the direction of Poynting vector $\vec{S}$. Thus, $\vec{v}_{ph}$ and $\vec{v}_g$ are anti-parallel for a metamaterial with simultaneous negative μ and ϵ.

For the passage of a wave from one medium to another (medium 1 to medium 2), the following boundary conditions have to be satisfied,

$$E_{t1} = E_{t2} \quad , \quad H_{t1} = H_{t2} \tag{0.8}$$
$$\epsilon_1 E_{n1} = \epsilon_2 E_{n2} \quad , \quad \mu_1 H_{n1} = \mu_2 H_{n2}$$

where E_t and H_t denote the tangential components and E_n and H_n represent the normal components of the field and subscript denotes the medium. Equation (2.8) shows that even though the tangential field components of the refracted ray in medium 2 does not change direction, the normal field components undergo changes direction for $\epsilon_2, \mu_2 < 0$. Thus the refracted ray in NIM medium 2 follows the path in red (ray 3) as illustrated in Figure 2-1. The group velocity is along this direction whereas the phase velocity is antiparallel to this direction in medium 2.

Snell's law for medium 2 having a refractive index n is given by,

$$n = \frac{\sin\theta}{\sin\varphi} \tag{0.9}$$

Hence, for a left-handed medium having simultaneous negative μ and ϵ, the index of refraction n relative to vacuum is negative (since φ is negative for LHMs).

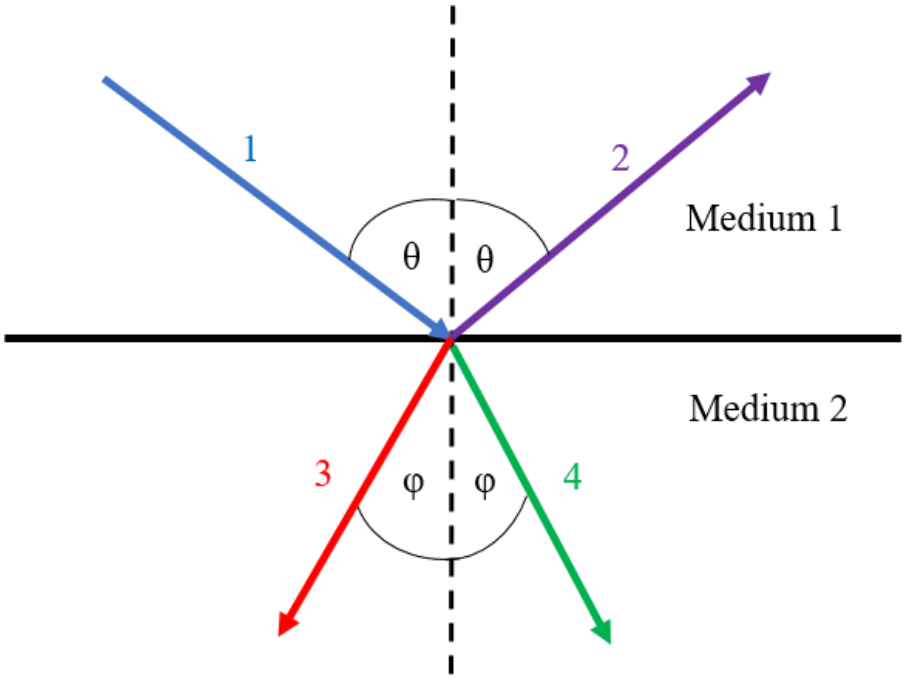

Figure 0-1 Passage of ray through boundary between two media. 1 - incident ray; 2 - reflected ray; 3 - refracted ray if medium 2 is left-handed; 4 – refracted ray if medium 2 is right-handed

1.5 Effective medium theory for Engineered Metamaterials

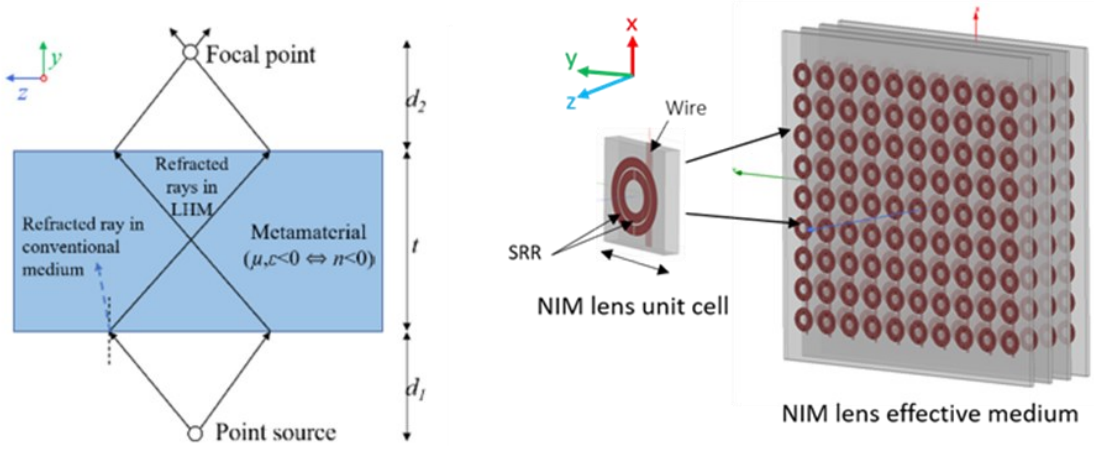

(a) (b)

Figure 0-2 (a) Homogenous NIM medium (b) Engineered NIM medium

The first LHM structure was realized by Smith et al., in their seminal paper of 2000 [21], where they showed that an alternating periodic array of SRRs and thin wires can produce an effective medium having a negative refractive index in the microwave regime. Early on, negative refractive index structures were a controversial topic, and their existence was disputed by researchers [46][47]. However, over the past two decades, there has been significant evidence that certain periodic structures can indeed have an effective negative refractive index over a limited range of frequencies [48][29][49][50]. Such periodic structures, even though inhomogeneous, can behave as a homogeneous medium in response to electromagnetic (EM) waves with appropriate wavelength [51].

A periodic array of conducting elements can act as an effective medium for EM scattering when the wavelength is much longer than the element dimensions, i.e.,

$$a \ll \lambda \tag{0.10}$$

where a is the dimension of a unit cell of the periodic array, and λ is the operating wavelength in the effective medium. The approximate lower limit for the effective medium ratio $\left(\frac{\lambda}{a}\right)$ is 4 for effective medium theory to hold [52]. EM response of an effective medium is determined by the configuration of the unit cell and can be characterized by an effective relative permeability μ_{eff} and effective relative permittivity ϵ_{eff} over a specific range of frequencies. The pioneering LHM unit cell comprises two distinct structures: an SRR element with dominant magnetic response and a thin wire element with dominant electric response (Figure 2-2b).

A periodic array of the SRR elements can exhibit an effective magnetic behavior, similar to that of magnetic plasmas, in the microwave regime [22]. Under excitation by an external magnetic field parallel to the axis of the SRRs, the array behaves as a bulk medium having an effective relative permeability given by

$$\mu_{eff}(\omega) = 1 - \frac{\frac{\pi r^2}{a^2}}{1 - \frac{3lc_0^2}{\pi^2\omega^2 ln\frac{2c}{d}r^3} + i\frac{2l\rho}{\omega r\mu_0}} \tag{0.11}$$

where, a is the lattice constant, l is the distance between layers, r,c,d are defined in Figure 2-3a, ρ is the resistance/unit length of the rings measured around the circumference, c_0 is speed of light in vacuum, u_0 is the permittivity of vacuum, and ω is frequency of incident radiation. A more generic form of the effective permeability of an SRR array is given by,

$$\mu_{eff}(\omega) = 1 - \frac{F\omega^2}{\omega^2 - \omega_0^2 + i\omega\Gamma} \tag{0.12}$$

where F is the fractional volume of the unit cell occupied by the rings, Γ is the dissipation factor, ω_0 is the resonant frequency of the SRRs, and ω is the frequency of the excitation field.

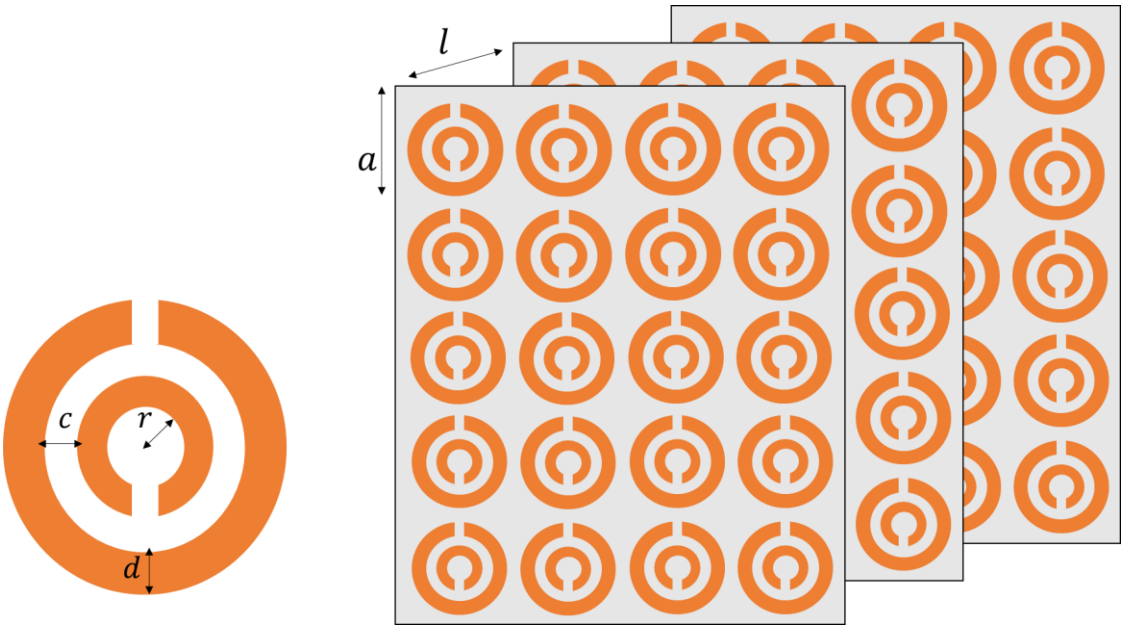

(a) (b)

Figure 0-3 (a) SRR unit cell schematic. (b) A periodic array of SRRs for negative permeability effective medium. The representative figure shows 5 × 4 × 3 unit cells of SRR.

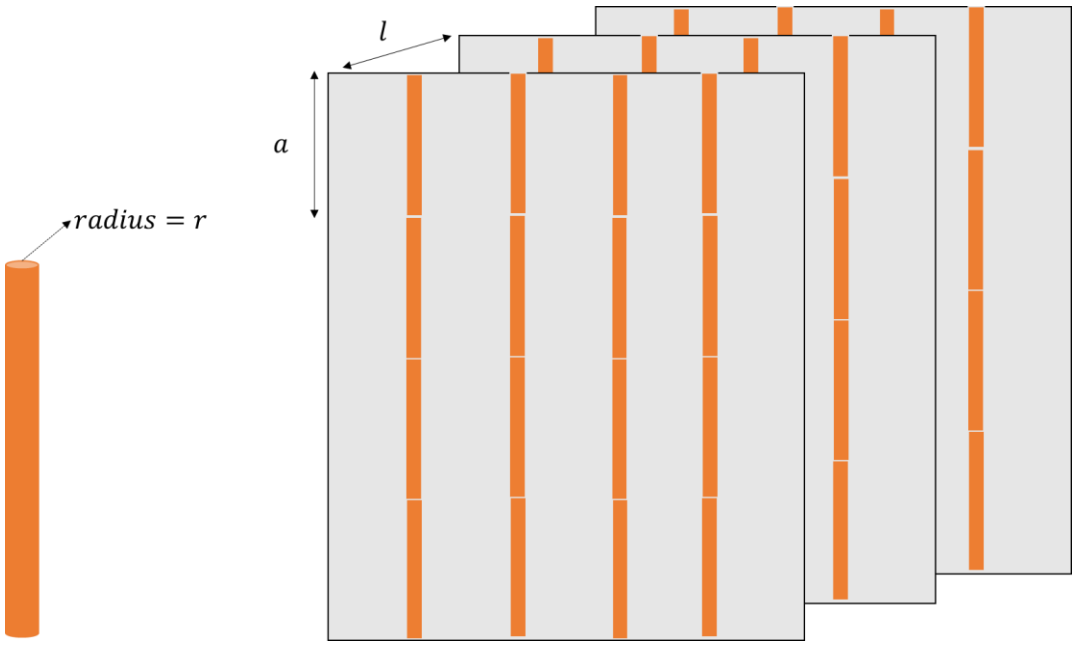

(a) (b)

Figure 0-4 (a) Thin wire unit cell. (b) A periodic array of thin wire for negative permittivity effective medium. The representative figure shows $4 \times 4 \times 3$ unit cells of thin wires.

Equation (2.12) shows that the real part of μ_{eff} is negative for frequencies ω greater than resonant frequency ω_0 and less than magnetic plasma frequency ω_{mp} given by $\omega_{mp} = \omega_0/\sqrt{1-F}$. Propagating wave modes are prohibited in this frequency band due to negative μ_{eff} of the SRR medium.

A periodic array of the thin metallic wire elements (Figure 2-4), under the influence of a time-varying electric field, can mimic an electric plasma at microwave frequencies [23]. The effective relative permittivity of such an array in the presence of an external electric field parallel to the wires is given by

$$\epsilon_{eff}(\omega) = 1 - \frac{\omega_{ep}^2}{\omega^2} \tag{0.13}$$

where, ω_{ep} is the electric plasma frequency given by,

$$\omega_{ep} = \frac{2\pi c_0^2}{a^2 \ln(a/r)} \tag{0.14}$$

where c_0 is the speed of light in free space, a is the lattice parameter, r is the radius of the wires and ω is the frequency of the excitation field.

where ω_{ep} is the electric plasma frequency of the wire medium, and ω is the frequency of the excitation field. Equation (2.13) shows that the real part of ϵ_{eff} has negative values for frequencies $\omega < \omega_{ep}$. This causes the wire medium to prohibit propagating modes in that frequency regime.

Combining both the SRR and wire elements in a periodic array gives rise to a metamaterial medium having simultaneous negative μ_{eff} and ϵ_{eff} over a certain range of frequencies (Figure 2-5). Assuming that there is no direct interaction between the SRR and wire media, the refractive index n of the resulting metamaterial is given through

$$n^2 = \mu_{eff}(\omega)\epsilon_{eff}(\omega) \tag{0.15}$$

The negative square root in the calculation of n is chosen in (2.15) when both $\mu_{eff}(\omega)$ and $\epsilon_{eff}(\omega)$ are negative to account for propagation of left-handed waves in a metamaterial []. A left-handed transmission band occurs within the previously overlapping forbidden bands of negative μ_{eff} and negative ϵ_{eff}. The combined array behaves as a medium having an effective negative refractive index in this transmission band, and the transmission peak is referred to as a left-handed peak.

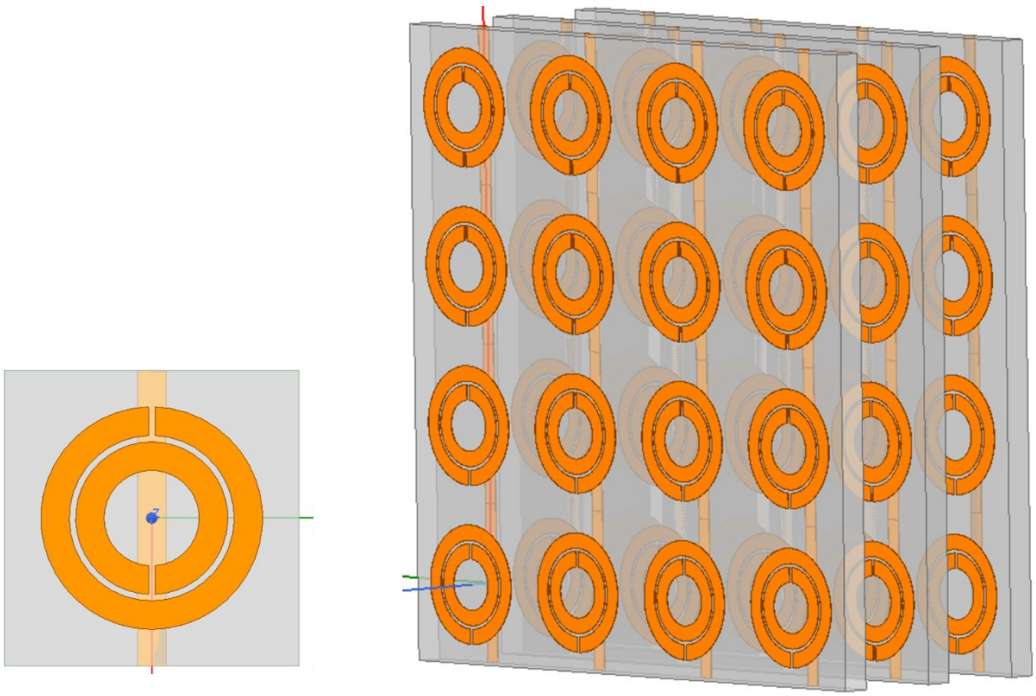

(a) (b)

Figure 0-5 (a) SRR-wire unit cell (b) A periodic array of SRR-wire unit cells for negative refractive index effective medium. The representative figure shows $4 \times 4 \times 3$ unit cells of SRR-wire.

1.5.1 Literature review on Engineered NIMs

After the first physical NIM design was realized by Smith et al. in 2000, extensive research on experimental verification of left-handed behavior followed. The transmission and reflection measurements of metamaterials reported by Smith et al. were performed in a waveguide chamber. Scattering experiments of unit cells performed in a TEM chamber provides requisite boundary conditions to mimic an infinite array of unit cells. Although experimental validation of left-handed transmission can be performed in this way, waveguide implementation limited one of the dimensions of the NIM structures in addition to practicality issues. Researchers in [53] for the first time described an EM windowing method for free space measurements of NIM structures. A typical setup for a free space S parameter measurement of a NIM structure in shown in Figure 2-6a. Figure 2-6b shows the measured S parameters of a NIM material designed to operate at 3.5 GHz.

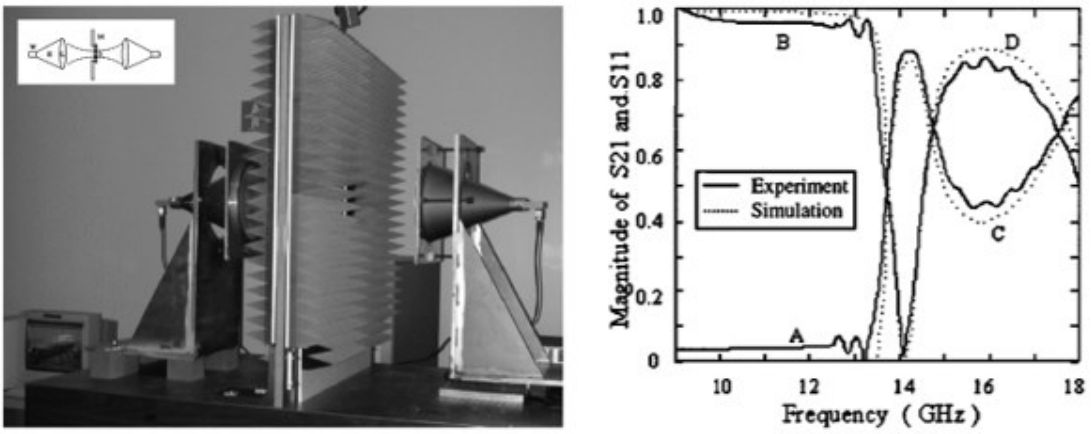

Figure 0-6 (a) Typical experimental setup used for free space S-parameter measurement of metamaterial. The setup schematic is shown in inset of figure [53]. (b) Measured and simulated S parameters for a left-handed material slab. Line A: measured transmission. Line B: measured reflection. Line C: simulated transmission. Line D: simulated reflection [53].

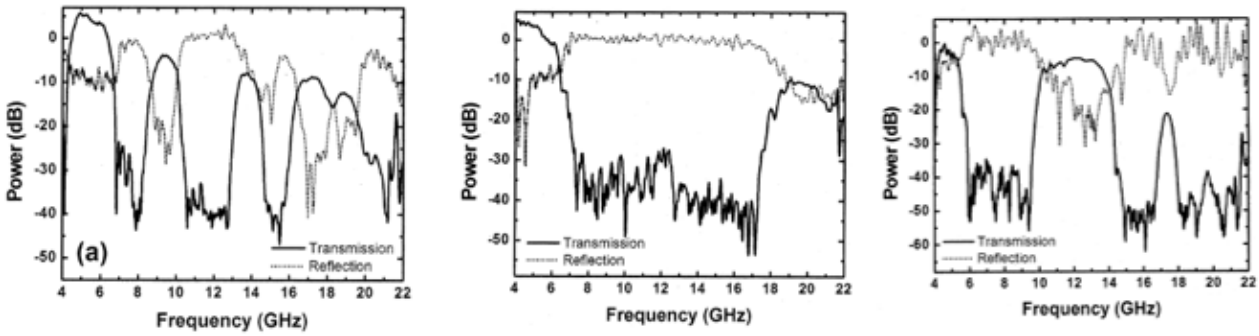

(a) (b) (c)

Figure 0-7 (a) Measured transmission and reflection spectra of SRR medium in free space. The negative permeability regions do not allow the propagation of electromagnetic waves through the SRR structure [54] (b) Measured transmission and reflection characteristics of the thin wire medium. The transmission spectrum exhibits a wide stopband extending from 7 to 18 GHz [54]. (c) Measured transmission and reflection spectra of the NIM medium. Relatively high power, -4.5 dB, is measured between frequencies 9.5 and 14.5 GHz in which both effective permittivity and permeability have negative values [54].

Ozbay et al. investigated the transmission and reflection properties of SRR medium, thin wire medium, and combined metamaterial medium separately [54]. A left-handed passband was demonstrated within the stop bands of the SRR and thin wires medium. The measured transmission and reflection characteristics for the three cases are shown in Figure 2-7.

Negative refraction in a NIM was first demonstrated in [24] using a 2D metamaterial structure (Figure 2-8). To determine the refractive index, the deflection of a beam of microwave

radiation is measured as the beam passes through a prism-shaped sample (Figure 2-8b). A positive refractive index sample will deflect the incident beam (black) will be deflected towards the right (blue) while a negative index metamaterial sample will deflect the beam towards left (red). Experiments were performed with a prism-shaped NIM sample, as well as with a similarly shaped Teflon sample as a reference. The measured $\vec{E}$ field strength (z-axis) is shown in Figure 2-8c as a function of refraction angle (x-axis) and frequency (y-axis). It is interesting to note that Teflon behaves as a positive refractive index material for all frequencies (12.5-13.5 GHz in the plot) while the engineered metamaterial behaves as a negative index medium around 13 GHz only. This demonstrates the narrowband operation of such engineered metamaterials. Negative refraction can also be demonstrated via incident beam shift experiment as described by Aydin *et al.* in [55]. This work will follow the beam shift experiment procedure for demonstration of NIM behavior. The experiment details is give in section 3.2.2.

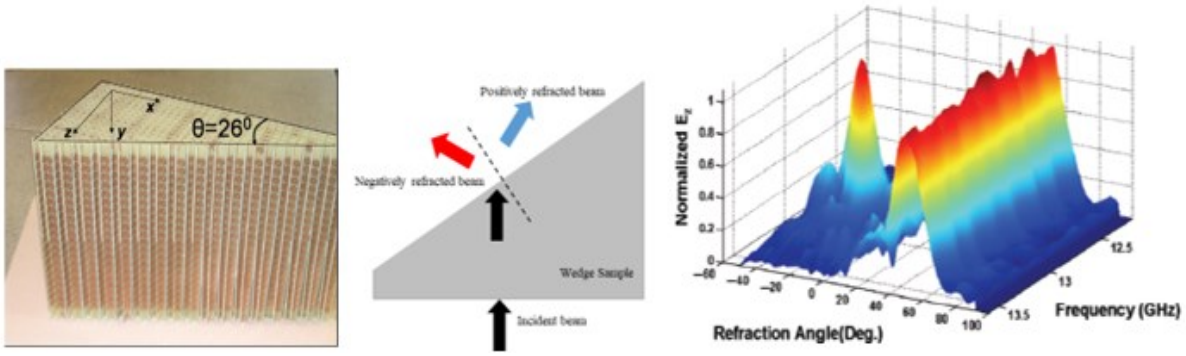

(a) (b) (c)

Figure 0-8 (a) A typical 2D prism-shaped NIM sample [24]. (b) Negative and Positive Refraction in a prism-shaped sample. (c) Surface plot of measured normalized peak amplitude of electric field component for a Teflon and a NIM prism shaped sample [24].

1.6 NIM lens for super resolution beyond the diffraction limit

An object is visible because it either emits or scatters EM radiation. The problem of imaging an object is concerned with reproducing the EM field distribution of the object in an image plane. Consider a 2D monochromatic object in the x-y plane placed at $z = 0$. The field distribution

$\psi(x, y, z)$ of the object in free space can expressed as a superposition of all possible elementary plane waves given by the 2D Fourier spectrum

$$\psi(x, y, z) = \iint_{-\infty}^{+\infty} \psi_F(k_x, k_y) e^{j(k_x x + k_y y + k_z z)} dk_x dk_y \tag{0.16}$$

where $\psi_F(k_x, k_y)$ are the spatial frequency components of the object. Maxwell's equations tell us that $k_z = \sqrt{\frac{\omega^2}{c^2} - k_x^2 - k_y^2}$, where ω is the frequency of the source and c is the speed of light. For spatial frequencies $k_x^2 + k_y^2 < \frac{\omega^2}{c^2}$, k_z is real, leading to propagating waves of the field in the z direction. As we move out of the object plane along the z direction, the field distribution will change. As a consequence, the Fourier spectrum on the observation (image) plane will no longer resemble the object Fourier spectrum. The function of a lens is to apply phase correction to the radiative Fourier components of the object so that the fields reassemble to a focus, and an image of the object appears at the focal plane of the lens. However, for larger values of transverse wave numbers, corresponding to high spatial frequency, i.e. $(k_x^2 + k_y^2 > \frac{\omega^2}{c^2})$, k_z is imaginary leading to non-propagating evanescent waves. These evanescent waves, containing the higher spatial frequency information, attenuate exponentially with distance from the object. Conventional lenses can focus only the propagating waves and the evanescent wave spectrum of the object field is essentially removed from images in the far-field. Since propagating waves are limited to $k_x^2 + k_y^2 < \frac{\omega^2}{c^2}$, the maximum resolution Δ_F achievable by a conventional lens image is given by

$$\Delta_F \approx \frac{2\pi}{k_{max}} = \frac{2\pi c}{\omega} = \lambda \tag{0.17}$$

and the diffraction limit manifests itself as an image smeared over an area of approximately one wavelength in diameter. It was shown in [20] that a slab made of negative refractive index

material can act as a "perfect lens" as it can amplify the evanescent wave components along with bringing into focus the propagating waves. Figure 2-9 describe the working principles of a negative refraction lens. Negative refraction through the flat lens will bend the diverging rays from an object towards optical axis. The rays will converge once inside the lens, and then at a focal spot outside the lens where an image of the object will be formed (Figure 2-9a). In addition to bringing into focus the propagating rays, the evanescent wave components will also be amplified by the negative index slab, and the high spatial frequency information can be recovered in the image plane (Figure 2-9b). Hence, a perfect image of the object can be obtained at the focal plane of such a lens as all the Fourier components will contribute to the resolution of the image. Using geometric optics, it can be shown that an object placed at a distance d_1(front focal length) from a slab of thickness t with an arbitrary negative refractive index n will be bought to focus at a distance d_2(second focal length) given by [43],

$$d_2 = \frac{n_s \cos(\theta)\, t}{\sqrt{n^2 - n_s^2 \sin(\theta)}} - d_1 \tag{0.18}$$

where n_s is the refractive index of the surrounding medium and θ is the angle of incidence (Figure 2-9a).

The conditions under which perfect imaging will occur is given by

$$\epsilon = -\epsilon_s, \qquad \mu = -\mu_s \tag{0.19}$$

where ϵ and μ are the dielectric permittivity and magnetic permeability respectively of the negative index slab, and ϵ_s and μ_s are the corresponding quantities of the surrounding medium. The refractive index, n of any material is given by

$$n = \pm\sqrt{\mu\epsilon} \tag{0.20}$$

The negative square root in the calculation of n is chosen in equation (5) when both ϵ and μ are negative to account for propagation of backward waves in negative index medium [41]. Therefore, the refractive index n of a perfect lens in free space equals -1 and equation (3) reduces to $d_2 = t - d_1$.

The enhancement of evanescent wave components by NIM medium is demonstrated in Figure 2-9b. For the derivation of recovery of the evanescent waves by a NIM lens, a transverse electric mode wave with z as the direction of propagation is considered. Subscript 1 indicates vacuum medium whereas subscript 2 denotes NIM medium. The $\vec{E}$ field is given

$$E_{1+} = [0,1,0]e^{j(k_x x + k_z z - \omega t)} \tag{0.21}$$

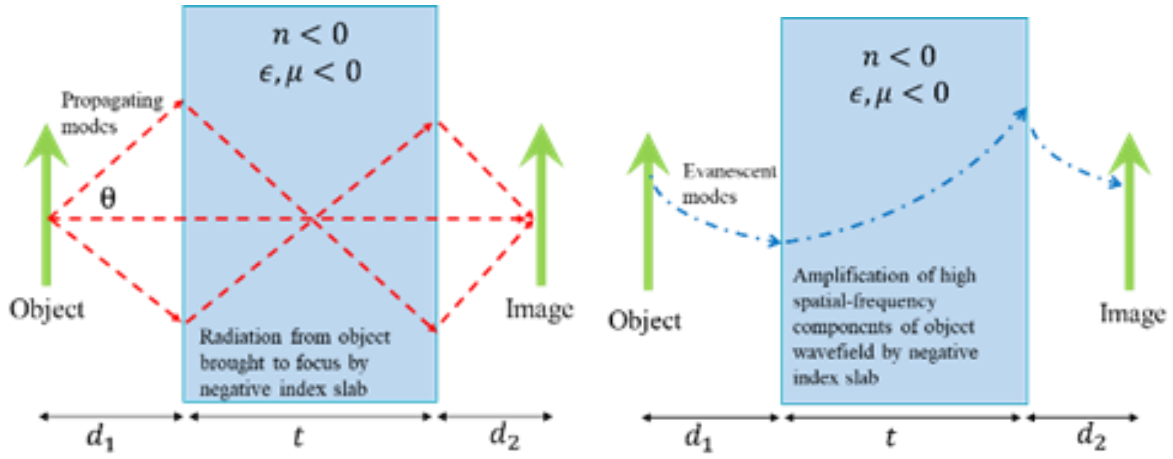

Figure 0-9 (a) Ray diagram showing focusing action due to reversal of Snell's law in a metamaterial medium. (b) Enhancement of evanescent wave components in a metamaterial medium.

For evanescent waves as discussed in Section 2.1, the wave vector k_z is imaginary and is given by $k_z = +j\sqrt{k_x^2 + k_y^2 - \frac{\omega^2}{c^2}}$, which implies exponential decay. At the boundary with medium 1, the reflected wave is given by

$$E_{1-} = [0,1,0]e^{j(k_x x + k_z z - \omega t)} \tag{0.22}$$

And the transmitted wave in medium 2 is given by

$$E_{2+} = [0,1,0]e^{j(k_x x + k_z' z - \omega t)} \tag{0.23}$$

where, $k_z' = +j\sqrt{k_x^2 + k_y^2 - \frac{\omega^2}{c^2}}$. Causality requires that this form of the wave in the medium is chosen i.e., it must decay exponentially from the interface. By matching wave fields at the interface, it can be shown that the transmission t, and reflection r, of the wave inside medium 1 is given by

$$t = \frac{2\mu k_z}{\mu k_z + k_z'}, \qquad r = \frac{\mu k_z - k_z'}{\mu k_z + k_z'} \tag{0.24}$$

The transmission t' and reflection r' of the wave inside NIM medium 2 is given by

$$t' = \frac{2k_z'}{k_z' + \mu k_z}, \qquad r' = \frac{k_z' - \mu k_z}{k_z' + \mu k_z} \tag{0.25}$$

To calculate the transmission T_s through the NIM medium of thickness$d$, the multiple scattering events have to be summed,

$$T_s = tt'e^{(jk_z'd)} + tt'r'^2e^{(3jk_z'd)} + tt'r'^4e^{(5jk_z'd)} + \cdots \tag{0.26}$$

$$or, T_s = \frac{tt'e^{(jk_z'd)}}{1 - r'^2e^{(2jk_z'd)}}$$

By substituting from 2.20 and 2.21 into 2.22 and taking the limits $\mu \to -1$ and $\epsilon \to$-1 for NIM medium, the transmission T_s is obtained as

$$\lim_{\substack{\mu \to -1 \\ \epsilon \to -1}} T_S = \frac{2\mu k_z}{\mu k_z + k_z'} \frac{2k_z'}{k_z' + \mu k_z} \frac{e^{(jk_z'd)}}{1 - \left(\frac{k_z' - \mu k_z}{k_z' + \mu k_z}\right)^2 e^{(2jk_z'd)}} \tag{0.27}$$

$$\lim_{\substack{\mu \to -1 \\ \epsilon \to -1}} T_S = e^{(-jk_z'd)}$$

Thus, even though strictly causal calculation was carried out, the result is that the NIM medium does amplify evanescent waves [26]. Such a negative index medium not only focuses propagating waves but also enhances the evanescent wave component of the angular spectrum of the incident field, which contains high-resolution information. Subwavelength focusing beyond the diffraction limit is, thus, made possible by using a negative index metamaterial lens. Pendry's seminal paper discussed the theoretical possibility of obtaining subwavelength imaging by virtue of metamaterial lens, which then led to experimental work on demonstration of subwavelength focusing [55][30][31][56][30].

Although in theory a perfect image reconstruction of an object can be obtained in this way using a lossless $n = -1$ slab, it is impossible to achieve these idealized conditions in practice. Losses associated with engineered metamaterials degrades the perfect resolving capabilities of NIM lenses. However, overcoming the diffraction barrier is still achievable using engineered NIM lenses [45].The EM metamaterial concept was extended to acoustic engineering as well [46], with several studies demonstrating subwavelength imaging using acoustic metamaterial lenses [47-48].

[28]. The focal distance of NIM lens is related to the image resolution Δ in the presence of losses stemming from imaginary permittivity (ϵ ") and imaginary permeability (μ "), and geometrical factor ξ = 0.6 by the equation [57]

$$f = \Delta \frac{ln\left[\frac{4\left(\xi^2\frac{\lambda^2}{\Delta^2}-1\right)}{\{\epsilon\}'' + \left(2\xi^2\frac{\lambda^2}{\Delta^2}\right)\{\mu\}''}\right]}{4\pi\sqrt{\xi^2 - \frac{\Delta^2}{\lambda^2}}} \tag{0.28}$$

The relationship specifically calculates the resolution Δ as the full width at half maximum of the image. Equation (2.24) does however assume real part of μ = -1 and ϵ = -1. Despite this, (2.21) provides a more robust model for the assessment of focal spot of a planar NIM lens with

real losses. Periodicity associated with a fabricated metamaterial also forces it to deviate from Pendry's perfect lens condition. The limitations for subwavelength imaging by a NIM lens have been studied by Smith et al. in detail [28].

Theoretical background and a literature review for effective medium of metamaterials is provided in this chapter, which guides this research. Imaging theory of NIM lenses and how they enhance the far-field resolution are also presented in this chapter. The following two chapters discuss the implementation of such NIM lenses at microwave S and C bands respectively.

S BAND NIM LENS FOR SUBWAVELENGTH DEFECT DETECTION

This chapter discusses the design of an S Band NIM lens and its experimental implementation for far-field microwave detection of subwavelength defects. Detailed numerical and experimental characterization of the lens design and its feasibility for far-field subwavelength defect detection is presented. Existing literature on using NIMs in the far-field employs electromagnetic windowing techniques to realize subwavelength focusing or defect detection. Microwave absorbers are typically used to create a window of the size of the NIM. The NIM structure is embedded in the window to ensure that waves pass through the NIM only. In this chapter, a homodyne receiver-based architecture is proposed to be used in conjunction with the NIM lens for far-field measurements. The high SNR and preservation of phase information associated with such synchronous detection allows the lens to be characterized in free space and, hence, provides a system that can be used in the field under practical conditions. The results of this chapter is published in [58][59].

The first section provides a numerical study and EM parameter retrieval of the lens design using the commercial software HFSS. The second section presents the experimental characterization of the metamaterial lens and its implementation for detection of subwavelength defects using the homodyne system.

1.7 Simulation

A metamaterial can be modeled by simulating an infinite periodic array of unit cells using periodic boundary conditions. Figure 3-1a shows an HFSS model of the proposed unit cell along with incident field polarization and direction of propagation. The Perfect E and Perfect H boundary conditions of HFSS were applied on the y-z and x-y boundaries, respectively, to mimic an infinite

array of unit cells and ensure correct polarization of the incident wave. FR4 ($\epsilon_r = 4.4, \tan\delta = 0.02$) of thickness 1.6 mm was used as the substrate for the PCB. Copper of thickness 35 micron was used as the conducting material. Wave ports were assigned on the z-x boundary to excite the model with a plane wave and obtain the S-parameters of the metamaterial medium. Figure 3.1b shows the dimensions of the unit cell. The dimensional parameters for the proposed design at 3.45 GHz are as follows: r = 1.5 mm, $c = g$ = 0.2 mm, $t = w$ = 0.9 mm, and a = 9.3 mm. The distance between consecutive PCB layers (length of unit cell model along z direction) is 6.5 mm.

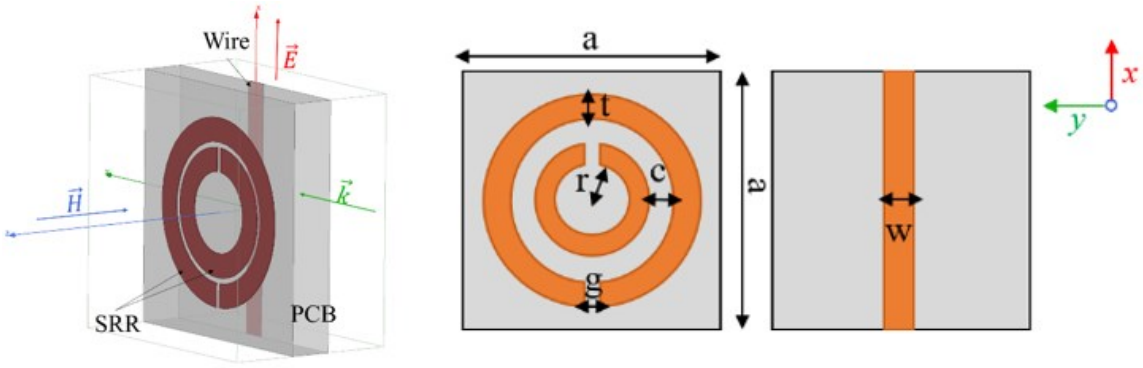

(a) (b)

Figure 0-1 (a) HFSS unit cell model. (b) Schematic of the metamaterial unit cell showing both sides of the PCB

1.7.1 Scattering Parameters

Figure 3-2 shows the simulated S-parameters for three cases—an SRR-only medium, a wire-only medium, and a medium that combines both wires and SRRs. For the SRR-only medium,

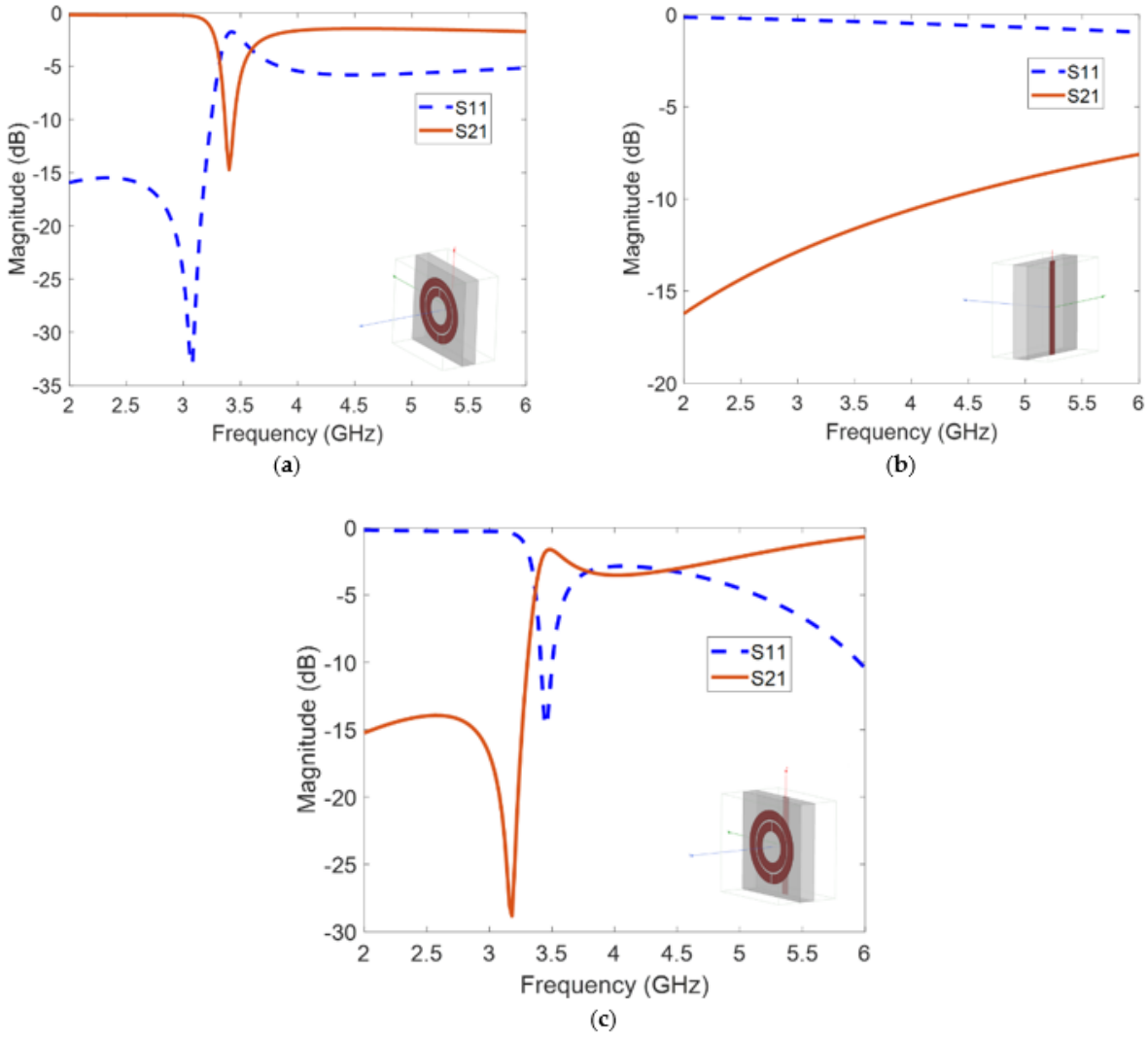

Figure 0-2 HFSS S-parameter results for (**a**) SRR-only medium, (**b**) wire-only medium, and (**c**) SRR and wire combined metamaterial medium. The respective HFSS models are shown in the insets of the figures.

a dip in the transmission parameter S_{21} is observed around the resonant frequency of 3.45 GHz of the SRR (Figure 3-2a). This is due to the prohibition of propagating waves by the negative μ of the medium. Figure 3-2b shows that the wire-only medium allows transmission (with less than 10 dB of insertion loss) above 5.5 GHz, which is the electric plasma frequency ω_{ep}. Propagating waves below this frequency are prohibited due to the negative ϵ of the wire medium. Figure 3-2c shows that after combining both the SRR and wire, a transmission band is observed around 3.45

GHz with a peak of -2 dB. Left-handed waves are allowed to propagate in the frequency region where both μ and ϵ are simultaneously negative.

Figure 0-3 HFSS S-parameter results for (**a**) SRR-only medium, (**b**) wire-only medium, and (**c**) SRR and wire combined metamaterial medium. The respective HFSS models are shown in the insets of the figures.

1.7.2 Electromagnetic Parameter Retrieval

Extraction of the EM parameters from S-parameter data of the metamaterial design was done to verify left-handed nature of the transmission band. Estimation of permittivity and permeability of an engineered material from its S-parameters is a well-established method, first proposed in the original work of Nicolson and Ross [60] and Weir [61]. Using this approach, an inhomogeneous metamaterial structure, assumed to be a homogenous medium under the effective medium theory, can be characterized by a refractive index n and normalized impedance z [62], [63].

The normalized impedance z of a metamaterial unit cell is related to its S parameters by the equation

$$z = \pm\sqrt{\frac{(1+S_{11})^2 - S_{21}^2}{(1+S_{11})^2 + S_{21}^2}} \tag{0.1}$$

Since the metamaterial is a passive device, the reflected power cannot exceed the incident power. Therefore, the real part of z is positive, which in turn resolves the sign ambiguity in (3.1).

The refractive index of a metamaterial unit cell of dimension d is related to the S-parameters by the following equation

$$e^{jnk_0 d} = \frac{S_{21}}{1 - S_{11}\dfrac{z-1}{z+1}} \tag{0.2}$$

The value of refractive index n can be evaluated from (3.2) as

$$n = \frac{1}{k_0 d}\left[\{Re\left(\ln\left(e^{jnk_0 d}\right)\right) + 2m\pi\} - j\{Im\left(\ln(e^{jnk_0 d})\right)\}\right] \qquad (0.3)$$

where *Re*(.) and *Im*(.) are the real and imaginary operators, respectively, k_0 is the free space wavenumber, and m is an integer. The ambiguity in the branch selection of the multi-valued complex logarithmic function in (3.3) can be resolved by choosing correct integer value m, which is dependent on the electrical length of the unit cell. Due to the small electrical length of the proposed unit cell design (9.3 mm) compared to the homogenized wavelength (38 mm), the fundamental branch ($m = 0$) is chosen for calculation of material parameters from the simulation model for the S band design [64].

The extracted material properties for the combined SRR and wire medium simulation results are shown in Figure 3-3. From the normalized impedance curve in Figure 3-3a, a resonance near the two plasma frequencies (3.45 GHz and 5.5 GHz) of the metamaterial medium is observed as expected. Figure 3.3b shows that the real part of the extracted refractive index is negative, thus verifying the left-handed transmission band in this frequency region. The value of real part of n at the resonant frequency of 3.45 GHz is −2.18. The real parts of the extracted μ_{eff} and ϵ_{eff} are also simultaneously negative in the frequency region, as expected (Figure 3-3c, d). It should be noted that above 5.5 GHz, both μ_{eff} and ϵ_{eff} are simultaneously positive, rendering the refractive index to be positive above this frequency.

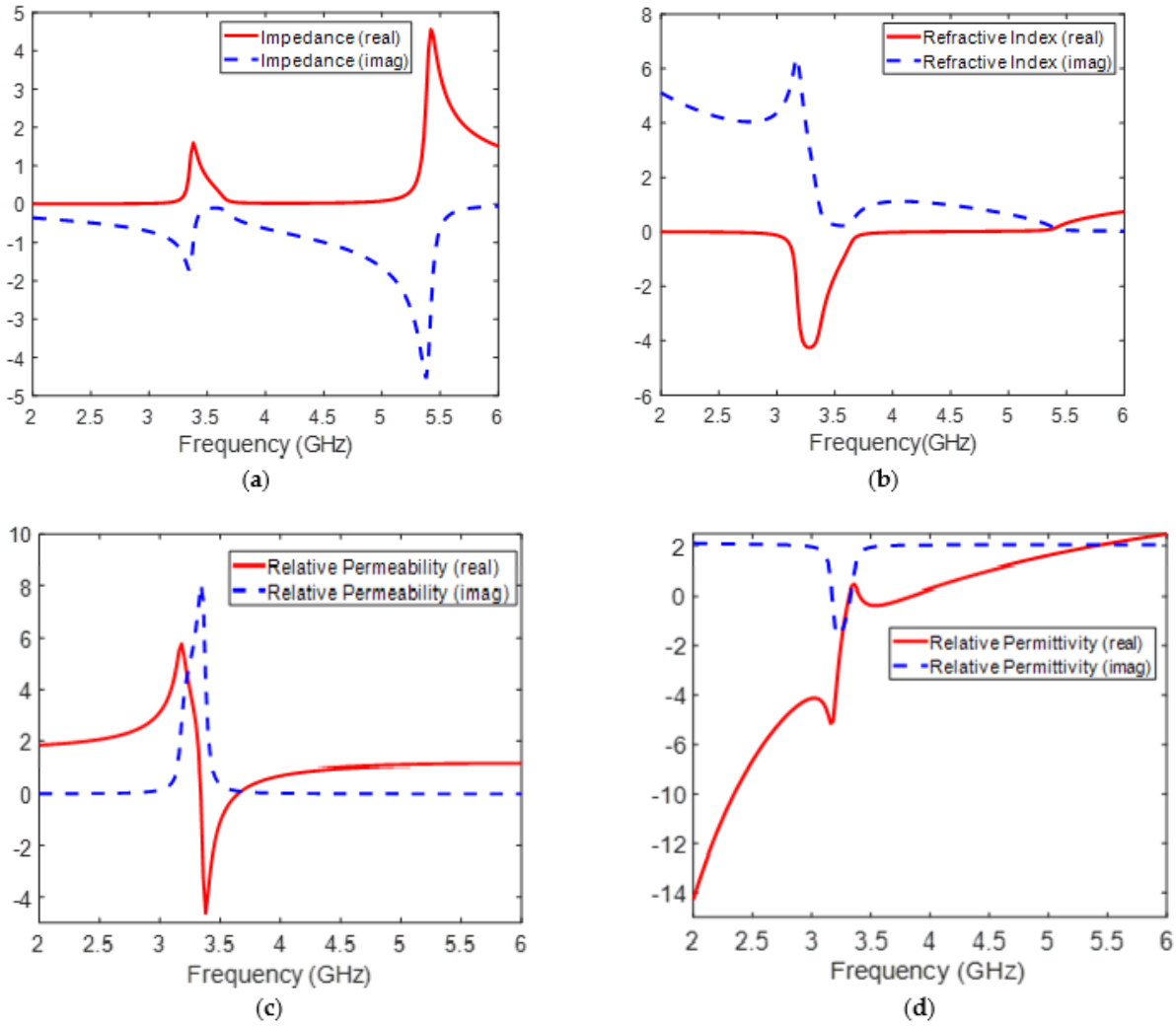

Figure 0-4 Extracted simulated EM parameters of the metamaterial design: (**a**) impedance, (**b**) refractive index, (**c**) permeability, and (**d**) permittivity.

1.8 Experimental Validation

A metamaterial lens, consisting of $N_x = 20$, $N_y = 10$ and $N_z = 31$ unit cells, was fabricated for experimental validation. Figure 3-4 presents the fabricated metamaterial lens. An array of 20 × 10 unit cells in the *x*-*y* plane were printed in a single FR4 PCB of thickness 1.6 mm, and 31 such boards were stacked in the *z* direction at an interval of 6.5 mm. The magnetic and electric field vectors are polarized along the *z* and *x* axes, respectively, while the wave propagation vector is along the *y* axis. The thickness of the lens, *t*, in direction of propagation is 100 mm. Frequency sweep measurements using a VNA were done at first to confirm the presence of left-handed transmission peak of the fabricated lens, which are presented in section 3.2.1. A homodyne detection-based scheme was used to experimentally validate the negative refractive index and determine the subwavelength focal spot at the left-handed transmission peak frequency. The implementation details and left-handed experimental results of the fabricated NIM lens with the homodyne architecture is discussed in section 3.2.2. NDE results for a set of dielectric test samples are presented to show the feasibility of using an LHM lens for the detection of subwavelength defects.

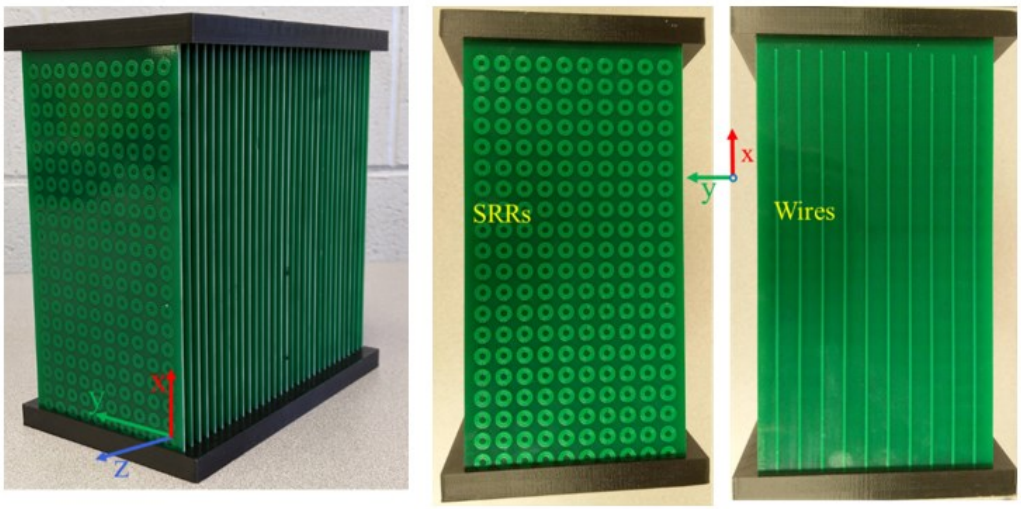

Figure 0-5 Fabricated metamaterial lens consisting of 20x10x31 unit cells and operating in S band.

1.8.1 Transmission characteristics

A large metallic screen (~10λ) with an appropriate aperture was used to obtain the transmission characteristics of the fabricated metamaterial lens. The metallic screen was implemented by mounting an aluminum sheet ono a styrofoam board. An aperture of the size of the lens was cut in the middle of the board to allow for waves to pass through the lens only []. Wideband (675 MHz to 12 GHz) Vivaldi antennas were used as transmitter and receiver to illuminate the lens with a uniform plane wave. The antennas were placed 40 cm apart to ensure far-field measurements. The frequency sweep measurements were done using an Agilent EB070B vector network analyzer (VNA). Figure 3-5a shows the schematic of experimental set up. The measurements of S_{21} in Figure 3-5b clearly indicate the presence of a left-handed transmission band with a peak transmission of −16 dB around 3.5 GHz (Figure 3-5b). The slight shift in frequency between the simulated and experimental results can be attributed to fabrication tolerances. Above 5.5 GHz, the metamaterial acts as a conventional medium having positive μ_{eff} and ϵ_{eff}. Conventional right-handed waves are allowed to propagate in this frequency regime, and hence, the transmission band is observed. The regions of negative and positive refractive index can be verified from Figure 3-3b.

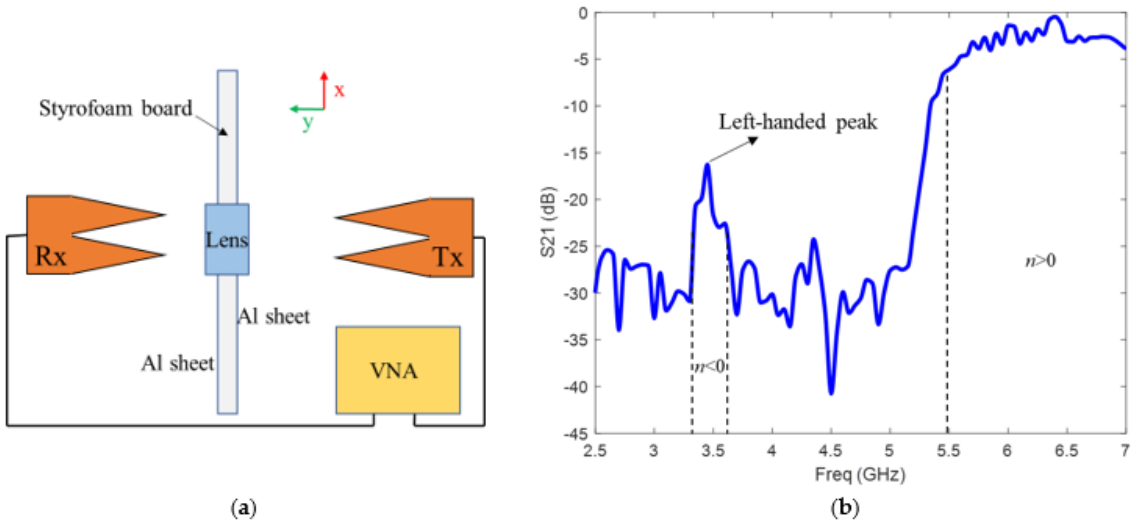

(a) (b)

Figure 0-6 (a) Free space transmission experiment schematic. (b) Experimental transmission response of the metamaterial lens. The measurements were calibrated with respect to transmission in free space.

1.8.2 Left-Handed Characteristics

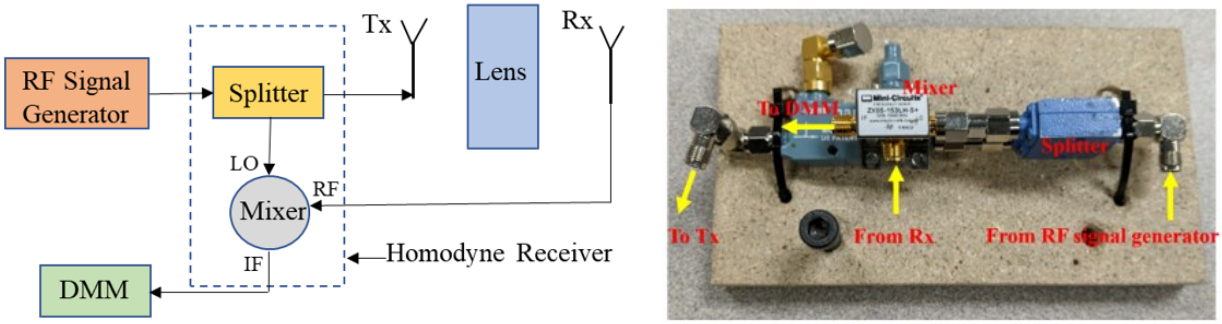

(a) (b)

Figure 0-7 (a) Schematic of homodyne architecture-based setup for single frequency measurements. (b) Homodyne receiver used in experiment setup

After experimentally confirming the left-handed transmission peak at 3.5 GHz, single frequency measurements using a homodyne receiver architecture were used to facilitate fast characterization of the metamaterial lens at 3.5 GHz. The schematic of the homodyne architecture is shown in Figure 3-6. The RF signal generator produces a continuous sinusoidal wave of frequency 3.5 GHz. The generated signal is passed through a splitter with one channel to the transmitting antenna and the other channel to the local oscillator (LO) port of the mixer. The RF port of the mixer is connected to the receiver antenna. The DC signal produced at the intermediate

frequency (IF) of the mixer is read by a digital multimeter (DMM) and is proportional to the strength of the received signal. The homodyne detection technique suppresses excessive noise components and provide stable access to information that is encoded into the phase of the received signal. This allows the fabricated NIM lens to be implemented in free space under practical conditions without the need for the windowing used in the frequency sweep measurements. Moreover, using homodyne detection obviates the need for the use of expensive RF instruments such as a VNA.

The operating principle of a homodyne detection system can be understood from the following equations. The sinusoidal output V_{LO} of the RF signal generator, which is used to excite the experiment setup and feed the LO port of the mixer is of the form

$$V_{LO} = V_{ref}(\sin \omega_{ref} t + \theta_{ref}) \tag{0.4}$$

where, V_{ref}, ω_{ref} and θ_{ref} are the amplitude, frequency, and phase of the RF signal generator output respectively. The received signal V_{RF} at the RF port of the mixer will be a sinusoid of the same frequency but different amplitude and phase given by.

$$V_{RF} = V_{rec}(\sin \omega_{rec} t + \theta_{rec}) \tag{0.5}$$

where, V_{rec}, and θ_{rec} are the amplitude, and phase of the received signal at the RF port respectively. The output V_{IF} at the IF port of the mixer is the product of the two sine waves given by,

$$V_{IF} = V_{LO} V_{RF} \tag{0.6}$$

$$V_{IF} = V_{ref}(\sin \omega_{ref} t + \theta_{ref}) V_{rec}(\sin \omega_{ref} t + \theta_{rec})$$

$$V_{IF} = \frac{1}{2} V_{ref} V_{rec} \cos\big([\omega_{ref} - \omega_{ref}]t + \theta_{rec} - \theta_{ref}\big) - \frac{1}{2} V_{ref} V_{rec} \cos\big([\omega_{ref} + \omega_{ref}]t + \theta_{rec} + \theta_{ref}\big)$$

It can be seen from (3.3) that the first term is a DC signal of the form

$$V_{DC} = \frac{1}{2} V_{ref} V_{rec} \cos\big(\theta_{rec} - \theta_{ref}\big) \tag{0.7}$$

V_{DC} produced at the IF port of the mixer is read in by the digital multimeter and is proportional to the received signal amplitude.

Negative Refraction Behavior of MM

An imaging experiment was carried out to demonstrate negative refraction by the metamaterial lens and to calculate its effective refractive index. A standard gain horn antenna at 3.5 GHz was used as the transmitter, while a quarter wavelength monopole was used as the receiving probe. Outgoing spherical waves from the horn are incident at an angle θ_i at the first air-LHM interface. After undergoing negative refraction through the LHM of thickness *t*, the waves are shifted towards the side of the transmitter by a distance *d* at the second LHM–air interface. The angle of refraction can be determined by scanning the received signal amplitude and calculated as $\theta_r = \tan^{-1}(d/t)$. The top view of the experimental setup is shown schematically in Figure 3-7.

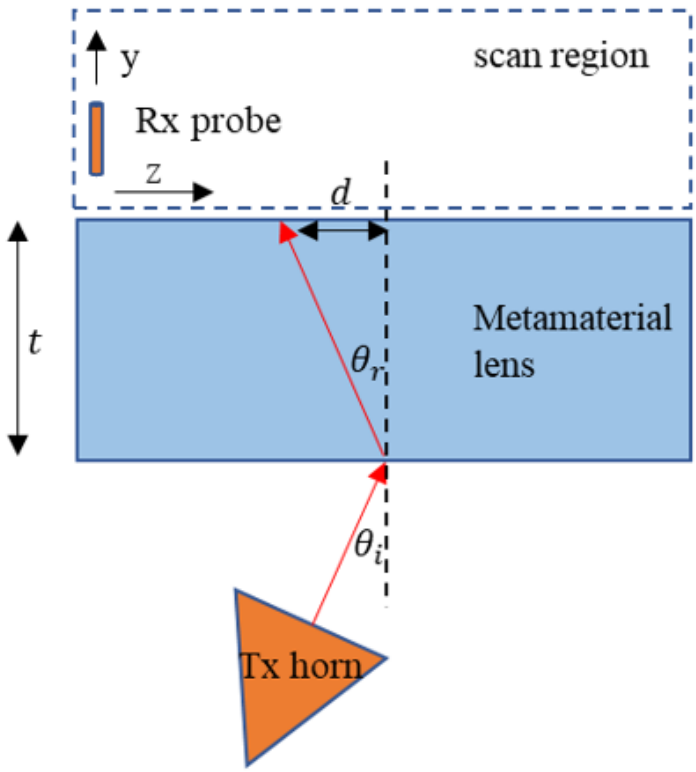

Figure 0-8 Negative refraction experiment schematic top view.

The receiving probe was mounted on a 2D scanner, moved in the *y*-*z* plane, and the received amplitude distribution was measured. A step size of 5 mm was used in both the *z* and *y* directions. The transmitting horn was placed at a distance of 12 cm (1.4λ) from the first air–LHM interface with an angle of incidence θ_i = 10°. The normalized amplitude distribution measured is shown in Figure 3-8a. The outgoing wave from the metamaterial lens has a beam profile centered towards the transmitting antenna. The angle of refraction, θ_r, through the lens of thickness t = 100 mm and beam shift d = 15 mm is calculated to be 8.53°. The real part of effective refractive index is thereby computed using Snell's law and is equal to −1.17 at 3.5 GHz.

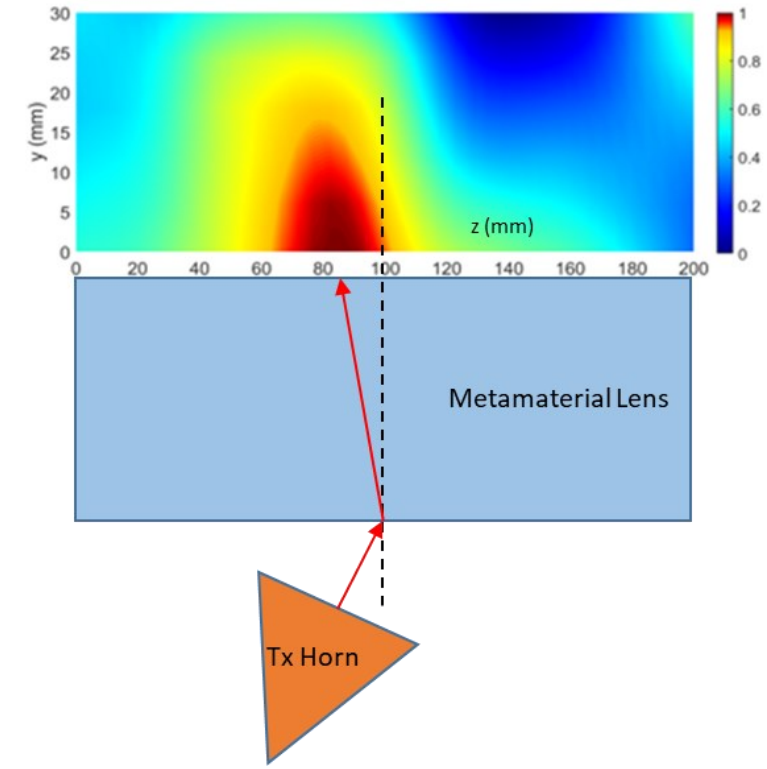

(a)

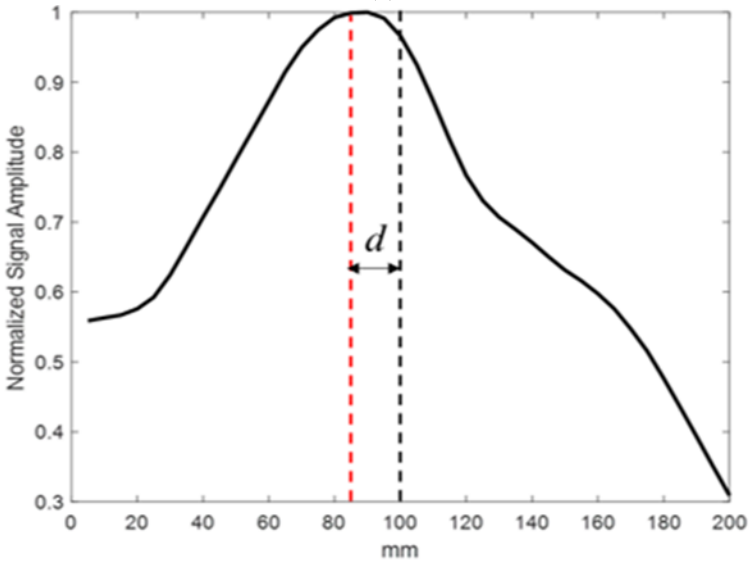

(b)

Figure 0-9 (a) Normalized received signal amplitude scan. The outgoing wave from the NIM lens has a beam profile centered at 85 mm. (b) Normalized line scan of the received signal amplitude at y = 0. The beam shift d is measured to be equal to 15 mm.

Subwavelength Focusing

The presence of negative refraction allows the possibility of using the fabricated metamaterial structure as a lens for subwavelength focusing. A monopole antenna produces an azimuthally symmetric field pattern, as does an ideal isotropic radiator. Therefore, a monopole with a resonant frequency of 3.5 GHz was used as the transmitter to demonstrate subwavelength focusing. Due to the negative refractive index of the metamaterial lens, diverging beams from the monopole antenna, placed at an appropriate distance, will be brought to focus outside the lens according to (2.13). Figure 3.9 presents the schematic top view of the experimental setup.

A quarter wavelength monopole was used as the probe for measuring the received signal. The receiving probe was mounted on a 2D scanner and moved on the *y*-*z* plane and the received amplitude distribution was measured. A step size of 5 mm was used in both the *z* and *y* directions. The transmitting monopole was placed at 60 mm (d_1) from the air–LHM interface. Figure 3-10a shows normalized received signal amplitude. A focal point is observed at a distance 30 mm (d_2) from the second LHM–air interface. The measured focal spot distance satisfies the relation in (2.13) for the fabricated lens of thickness 100 mm (t). Figure 3-10b shows the normalized line scan at the focal plane (y = 30 mm). The full width at half maxima (FWHM) for the focal spot is found to be 70 mm (0.82λ).

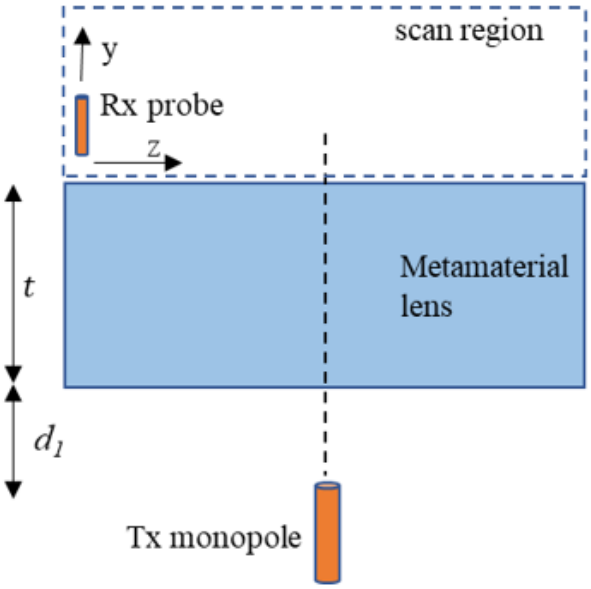

Figure 0-10 Subwavelength focusing experiment schematic top view.

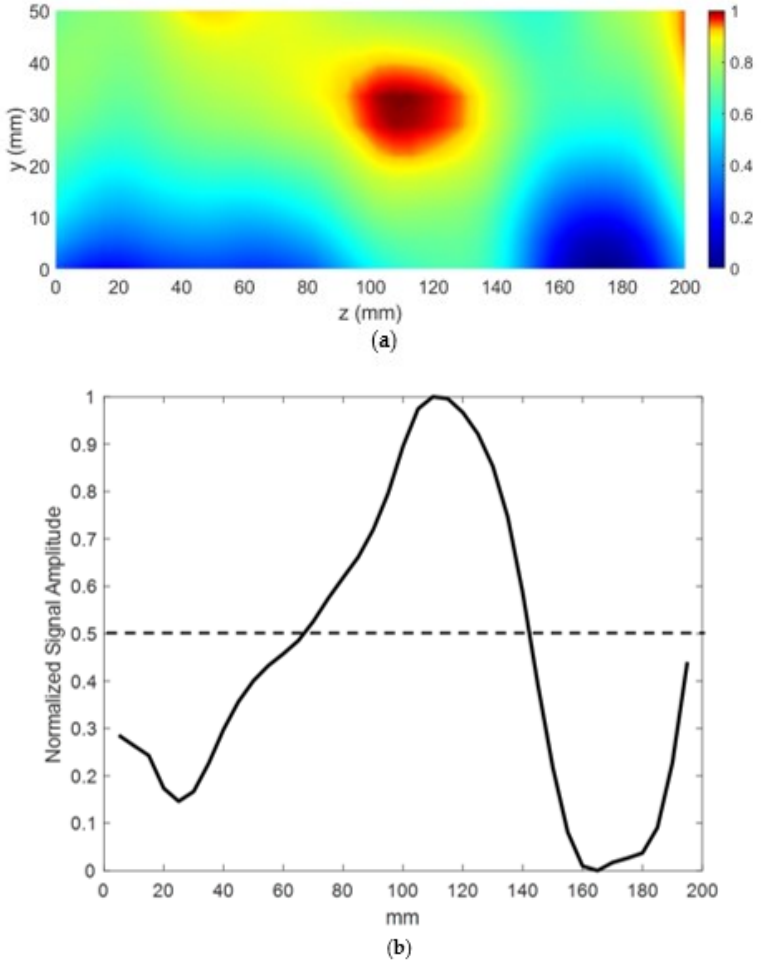

Figure 0-11 (**a**) Normalized received signal amplitude. A focal spot is observed at a distance of d_2 = 30 mm from the lens. (**b**) Normalized line scan at y = 30mm. The dashed lines indicate −3 dB point.

Microwave NDE

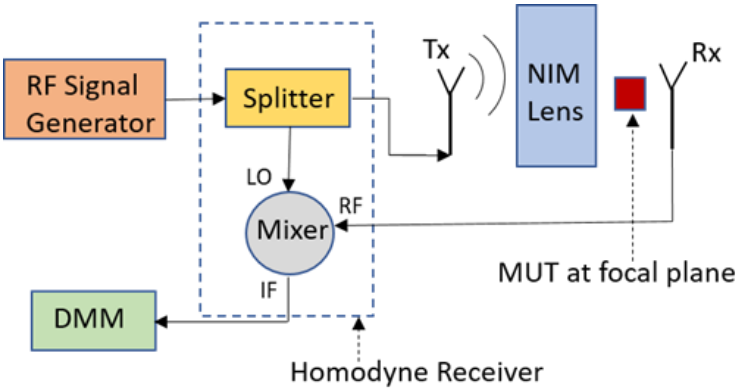

(a)

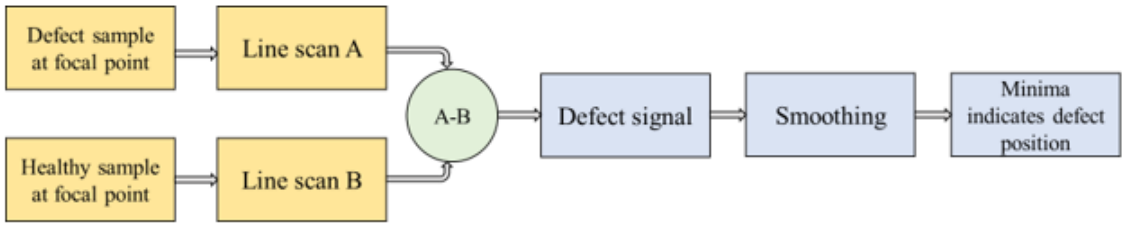

(b)

Figure 0-12 (a) Microwave NDE with NIM lens schematic (b) Calibration and defect detection flowchart.

Natural fiber reinforced composites have seen increasing use over the past few years due to their lower cost, preferable mechanical properties and environment sustainability over conventional materials such as metals and synthetic fibers. Composites can be tailored to have enhanced characteristics which has facilitated their growing application in industries such as aerospace, automotive and structural engineering [65][66][67]. However, composites are susceptible to defects due to manufacturing issues or damages incurred in usage. Hence, there is a need for NDE sensors for composites which can reliably detect these flaws that can affect the performance of crucial engineering structures [68].

Microwaves have the ability to penetrate deep into low loss dielectrics and hence are suitable for inspection of electrically insulated low loss composites. In addition to this, a microwave NDE system offers various advantages over other existing NDE techniques such as non-contact, no requirement for couplants, relatively low cost and one-sided scanning [7].

Therefore, the capability of the fabricated NIM lens for detection of subwavelength defects with far-field microwave NDE data is demonstrated. The Microwave NDE schematic is shown in Figure 3-12a. The calibration and detection procedure are shown in Figure 3-12b and is summarized as follows:

i Samples for testing are placed at the focal plane of lens, and line scans are performed to obtain the scattered data

ii Contributions due to a defect is measured by changes in the test signal relative to baseline signal (found by measuring a similar healthy sample)

iii Position of defect is determined by the minima in the line scans

The experimental setup for this study is shown in Figure 3-12, and the schematic top view is shown in Figure 3-13a. Figure 3-13b shows the schematic of sample under test. Teflon samples are used as the dielectric test object that is inspected for defects. A groove of size 15mm (0.17λ) × 5 mm (0.06λ) is machined along the length of the sample and serves as the anomaly. A similar Teflon sample with no machined groove is treated as the healthy sample for background subtraction. The samples are placed at the focal plane of the lens. Three sets of measurements were taken at three positions of the sample by following the described calibration and detection procedure. The distance *p* between consecutive defect positions was set to be 20 mm (0.23λ).

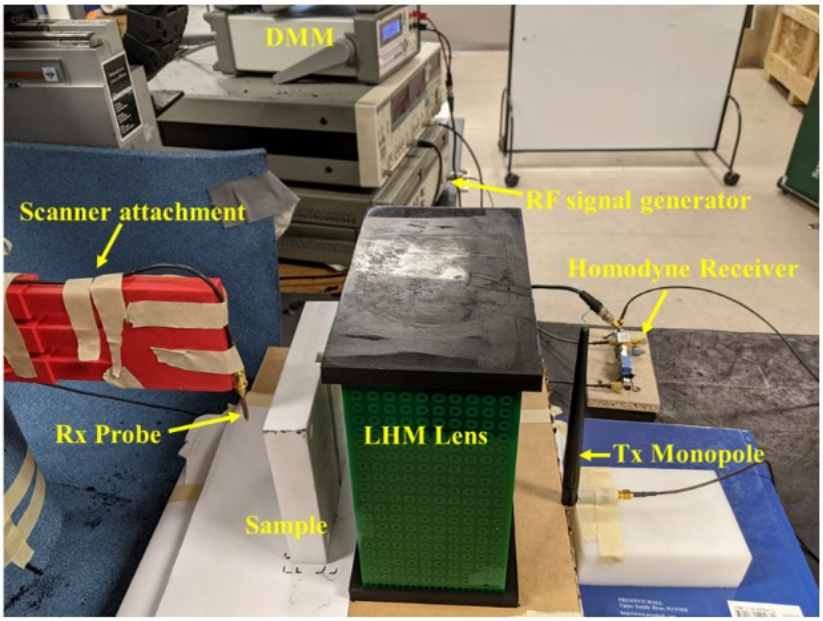

Figure 0-13 Proposed microwave NDE sensor. The sample is kept at the focal point of the LHM lens to allow for subwavelength defect detection.

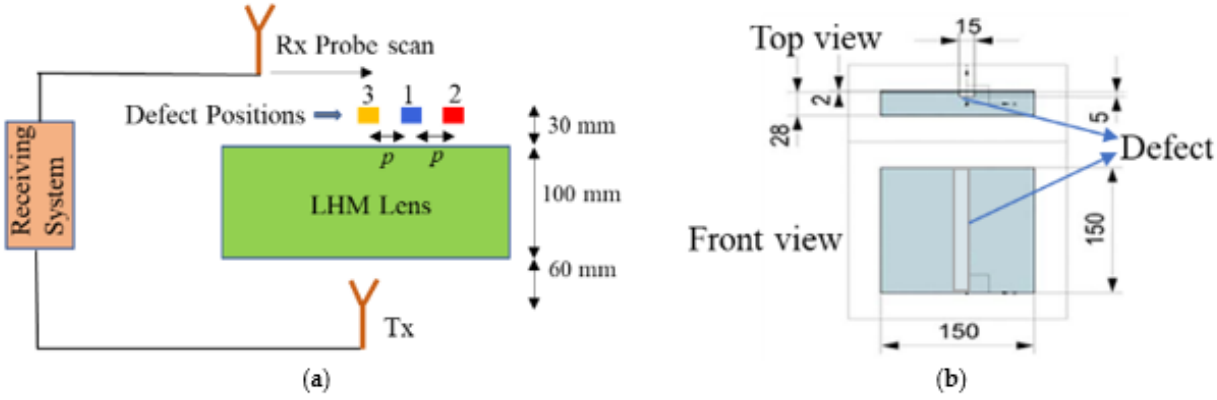

Figure 0-14 (a) NDE experiment schematic top view. (b) Sample under test schematic. All dimensions are given in mm.

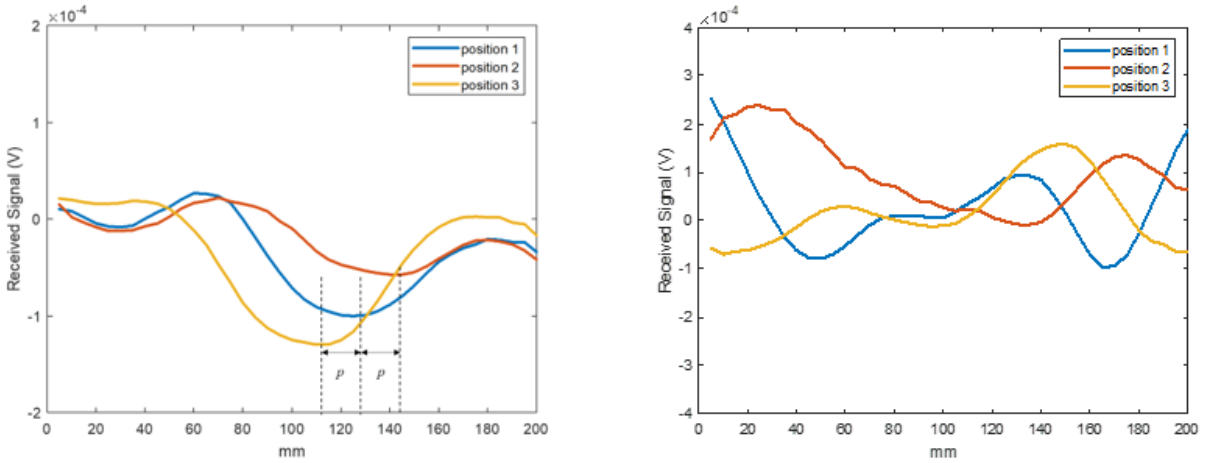

Figure 0-15 NDE line scan results. (**a**) Measurements using the LHM lens. The minimum of the plot gives the defect position. (**b**) Measurements without the LHM lens. Waves are not focused in free space. Subwavelength defects position cannot be determined.

Figure 3-14a shows the defect signal for the three measurements. The received line scans were fitted with smooth curves to obtain the minima. The minima in the three line scans are shifted with repositioning of the defect location, thus indicating the position of the subwavelength defect. This demonstrates the proposed system is sensitive to a $0.17\lambda \times 0.06\lambda$ defect and can determine the defect positions with a separation of 0.23λ. The NDE measurements were repeated without the NIM lens to illustrate that the subwavelength defects are not detectable without the lens. Figure 3-14b shows the resulting received line scan signals without the lens. Since waves from the monopole transmitter are not focused, the received signal strengths are dominated by edge effects and scattering from the background. Therefore, no clear minima, as in the case of the NIM lens, are observed. Hence, these initial results clearly demonstrate that subwavelength defects, which are undetectable in free space in the far field, can be detected using a properly designed metamaterial lens.

C BAND NIM LENS FOR SUBWAVELENGTH MICROWAVE IMAGING

This chapter describes the design of a C band microwave imaging system using a negative index metamaterial (NIM) lens for nondestructive evaluation (NDE) applications. The imaging system consists of a split ring resonator (SRR)-wire based NIM lens, operating at 6.3 GHz, used in conjunction with a homodyne detection system. The lens design is similar to the preceding chapter but scaled to work at a higher frequency band. The resolution of the lenses are dependent on the operating wavelength. Therefore, a shorter wavelength design is considered in this chapter to demonstrate the scalability of the NIM lens designs for detection of smaller defects in composite samples. The unit cell design reported in this chapter has an improved left-handed transmission with a peak of -1.08 dB (S band design transmission peak was -2 dB). Hence, a smaller focal spot is obtained for this C band NIM lens design. Simulation studies of the unit cell design are presented followed by experimental verification of left-handed focusing by the NIM lens with a focal spot of size 0.65λ. Further, 2D NDE scans are reported in this chapter to demonstrate the ability of the proposed system for imaging defects in addition to detection capabilities reported in Chapter 3. A subwavelength hole of diameter 0.25λ in a glass fiber reinforced polymer (GFRP) sample is imaged at a stand-off distance of 1.67λ using the proposed system. High SNR and preservation of polarity and phase information associated with synchronous detection provides a NIM lens imaging system that can be used in the field for rapid inspection at large standoff distances.

1.9 Simulation

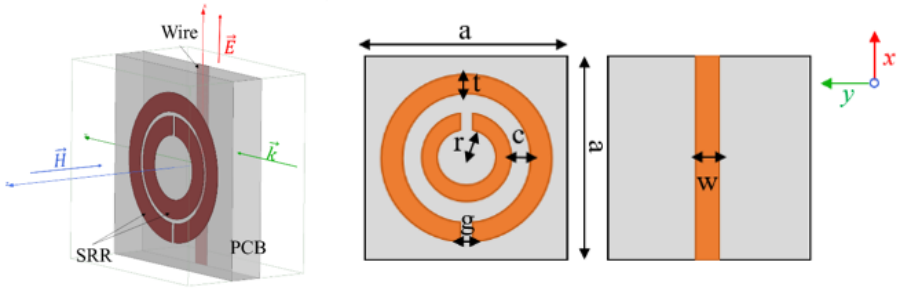

Figure 0-1 NIM lens unit cell model with incident wave polarization and unit cell schematic.

The unit cell schematic along with the incident wave polarization is shown in Figure 4-1. The $\vec{H}$ field is polarized into the plane of the SRRs (z direction) while the $\vec{E}$ field is polarized parallel to the wires (x direction) to generate the required EM response for negative refractive index. A left-handed ($\vec{E}$, $\vec{H}$ and $\vec{k}$ form a left-handed triplet) transmission band is obtained in the frequency region where the refractive index is negative. The dimensional parameters for the unit cell to operate around 6.3 GHz is given by a = 4mm, r = 0.9 mm, t = 0.4 mm, w = 0.4mm, g = 0.2 mm, c = 0.2 mm. FR4 of thickness 0.6 mm is used as the PCB substrate. The distance between consecutive PCB layers is set to be 3.4 mm. The simulated S parameters for the unit cell design using commercial solver Ansys HFSS is shown in Figure 4-2a. A transmission band is obtained around 6.3 GHz with a transmission peak of -1.08 dB. To verify the left-handed nature of the transmission band, EM parameter retrieval from the simulated S parameters is performed. The parameter retrieval method is described in section 3.1.2. The real part of μ_{eff} and ϵ_{eff} are simultaneously negative in this band, rendering the refractive index n to be negative (2.15). The refractive index for the proposed NIM lens is -3.33 at the operating frequency of 6.3 GHz (Figure 4-2b).

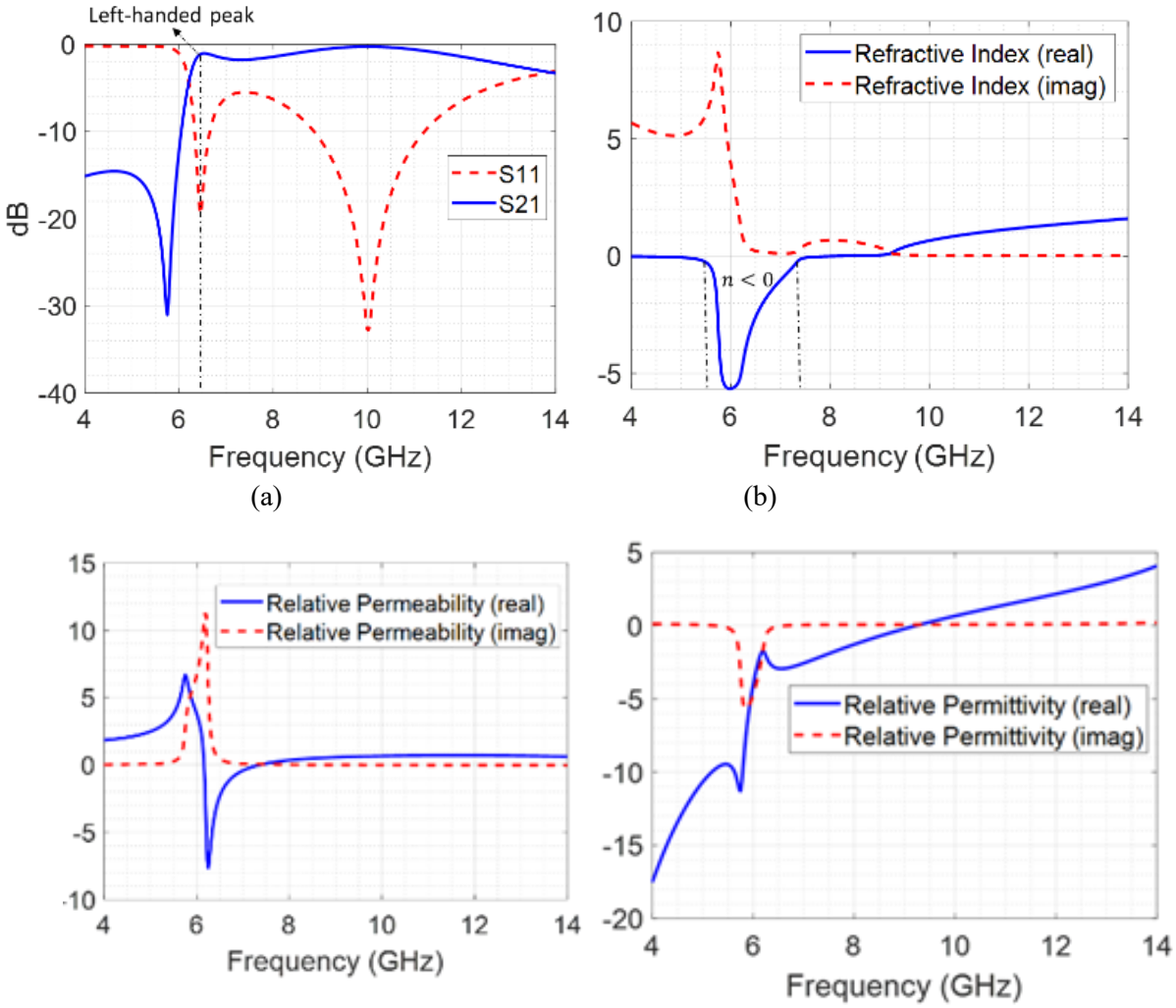

Figure 0-2 (a) Simulated S parameters using Ansys HFSS (c) Refractive index calculated from simulated S parameters

1.10 Experimental Validation

A NIM lens, consisting of $N_x = 20$, $N_y = 10$ and $N_z = 30$ unit cells, was fabricated for experimental validation. Figure 4-3a presents the fabricated metamaterial lens. Each PCB layer consists of 20x10 unit cells and 30 such layers were stacked at intervals of 3.4 mm using 3D printed holder with slots. The final dimensions of the lens are $80\ mm\ (1.67\lambda) \times 40mm\ (0.83\ \lambda) \times 100\ mm(2.08\lambda)$.

1.10.1 Transmission Characteristics

Frequency sweep measurements were performed at the beginning using an Agilent EB070B VNA to experimentally determine the left-handed transmission peak of the fabricated lens. Two horn antennas were used as the transmitter and receiver to ensure correct polarization of the incident EM waves. The antennas were kept at a distance of 20 cm to ensure far-field measurements. A large metallic screen with a window of the size of the lens was used to perform the measurements (Figure 4-3b). The S_{21} normalized to peak transmission are shown in Figure 4-3c. A left-handed peak transmission of -1.5 dB is observed around 6.3 GHz. Conventional right-handed transmission band is obtained above 9.5 GHz. The refractive index of the lens is positive in that frequency region as shown in Figure 4-2b.

The differences between the simulated and experimental transmission characteristics can be attributed to the following factors. The simulation study considers an infinite array of unit cells with periodic boundary conditions whereas the experimental study consists of a finite number of unit cells. In this study, to estimate the bulk parameters using unit cell simulations, periodic boundary conditions in the directions perpendicular to the wave propagation direction, is implemented. Along the direction of propagation, the model uses one unit cell as it can estimate the effective parameters without complicating the calculation of effective parameters. One unit cell in the propagation direction produces nearly the same scattering parameters as a thicker material, and estimation of bulk parameters using this simulation model becomes less cumbersome. Depending on the value of bulk parameters and frequency of a metamaterial design, there is a certain "critical length" of unit cells after which, the simulation model will closely resemble the scattering parameters of a finite metamaterial array structure. This is because the transmission in a single unit cell model along the direction of propagation includes contribution

from additional polarized waves in addition to the incident wave polarization. The contributions from these additional polarized waves, due to perturbation inside the structure, are not observed after the "critical length" of unit cells. Therefore, the simulation transmission characteristics will closely follow finite array experimental characteristics only if multiple unit cells in direction of propagation are simulated. However, in that case, the branch selection in the estimation of bulk parameters from scattering parameters will be more involved and out of scope for this thesis work. For this study, 3 unit cells in direction of propagation will result in transmission characteristics that closely match that of experimental results. The result of such a simulation model is reported in figure 6 of [59]. Another reason for the deviation from simulated results reported in this work is the use of EM windowing experiments. Performing the experiments in an anechoic chamber will remove the noise in the experimental transmission characteristics reported in this study for NIM lenses.

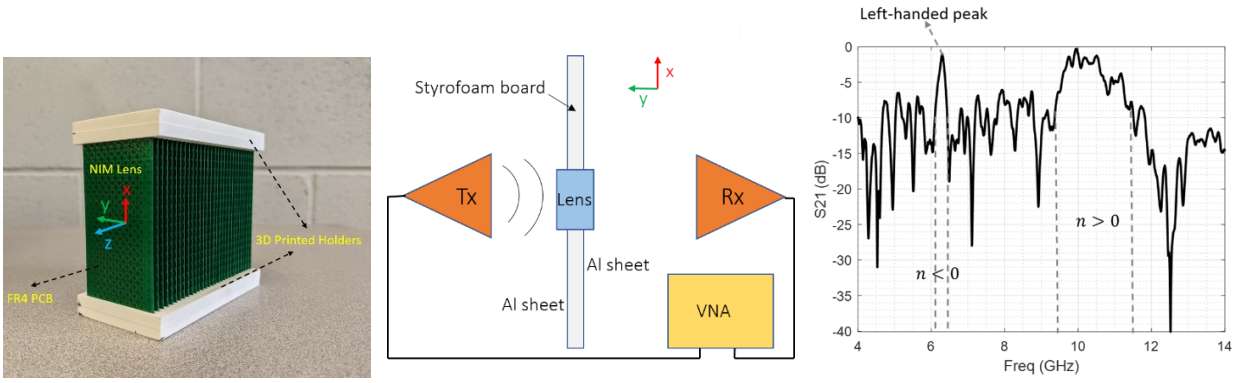

(a) (b) (c)

Figure 0-3 (a) Fabricated NIM lens (b) Transmission experiment schematic (c) Measured transmission characteristics

1.10.2 Source Imaging

After the left-handed peak frequency was determined, single frequency measurement using synchronous detection was done to provide a low-cost practical imaging system without the need for EM windowing. The setup for the source imaging experiment is shown in Figure 4-4. A

monopole with resonant frequency of 6.3 GHz was used as source. A monopole antenna produces an azimuthally symmetric field pattern, as does a point source. Left-handed focusing of the incident omnidirectional waves by the NIM lens allows source imaging at the focal plane of the lens. A quarter wavelength monopole was used for measuring the received signal. The receiving probe was mounted on a 2D scanner and moved on the *y*-*z* plane and the received signal distribution was measured. A step size of 5 mm was used in both the *z* and *y* directions. The transmitting monopole was placed at 10 mm from the air–NIM interface. Figure 4-5a shows normalized received signal distribution. A focal point is observed at a distance 35 mm from the second NIM–air interface. The measured focal spot distance is consistent with NIM lens imaging theory [1]. The source imaging experiment was performed without the NIM lens as well and the results are shown in Figure 4-5b. The received signal distribution shows the radiation pattern of an omnidirectional source as expected. Figure 4-5c displays the cross-range intensity profiles for the two cases. The full width at half maxima (FWHM) for the focal spot is found to be 30 mm (0.62λ). The FWHM at the focal plane without the lens is 67 mm (1.39λ) indicating resolution enhancement by a factor of 2.24 ($\Delta_{lens}/\Delta_{free}$) is achieved with the lens.

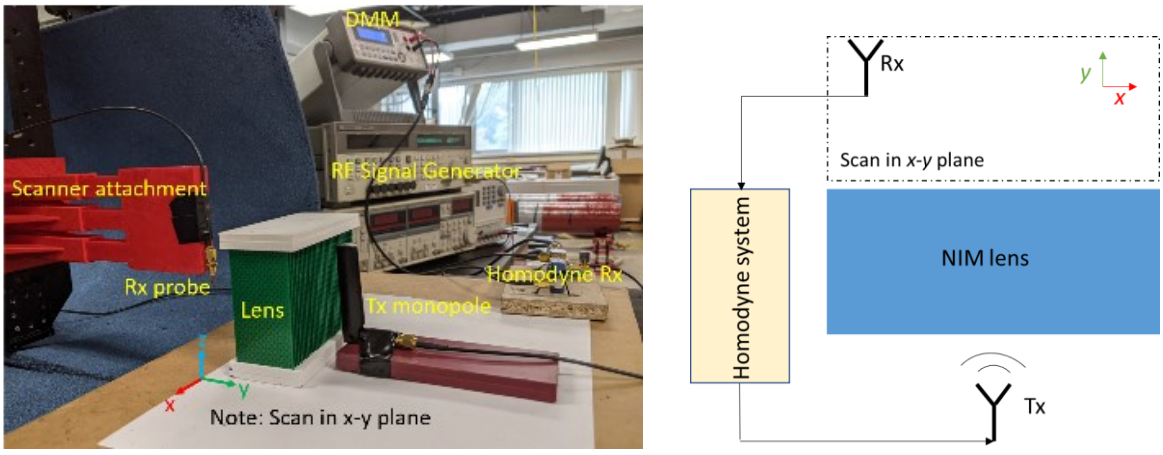

(a) (b)

Figure 0-4 Source imaging experiment (a) setup and (b) schematic

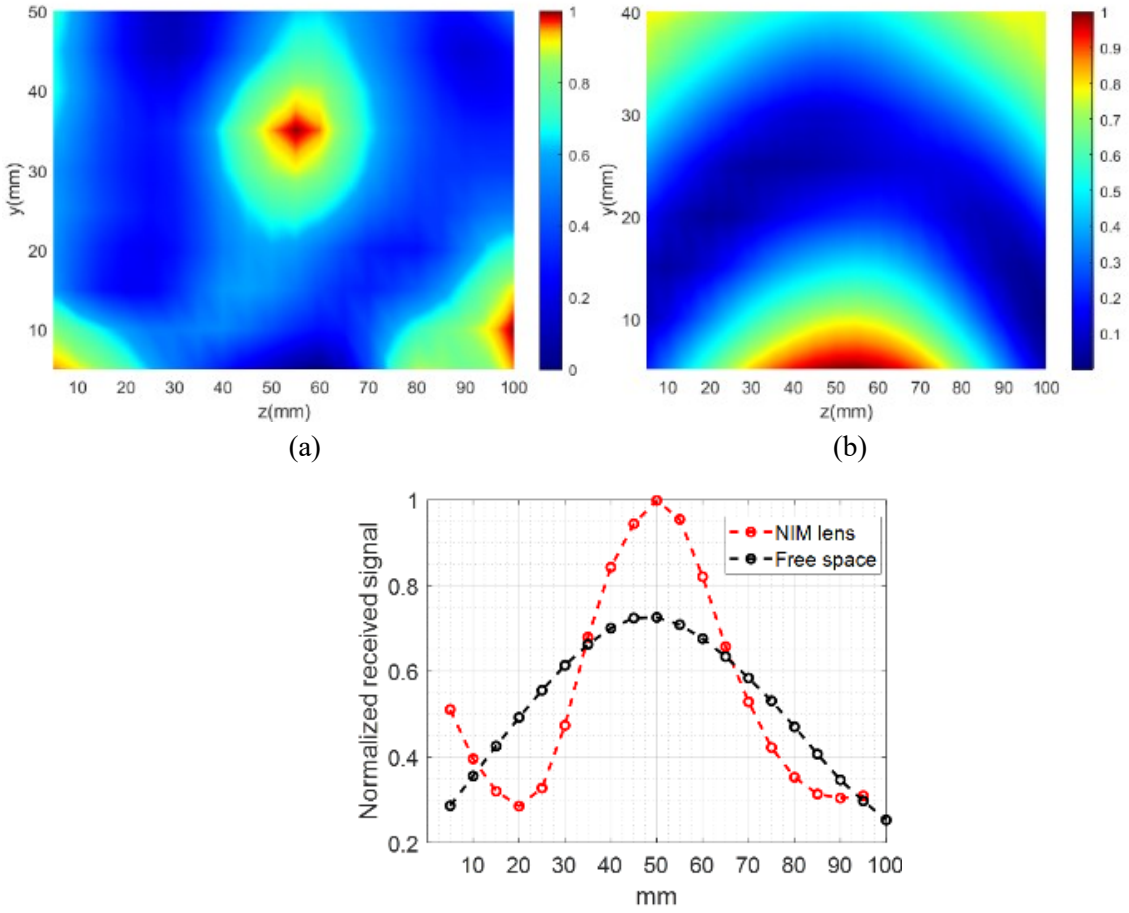

Figure 0-5 (a) Measured intensity distribution with lens (b) Measured intensity distribution without lens (c) Lateral intensity profile comparison at the focal plane for with and without lens.

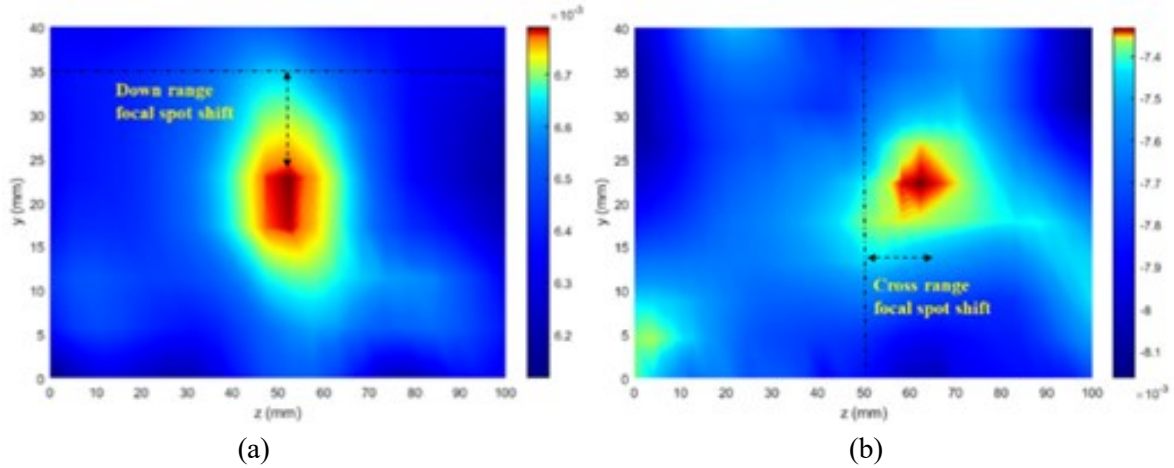

Figure 0-6 (a) Focal spot shift in (a) Down range direction (b) Cross range direction

The focal spot position of a NIM lens can be adjusted in the cross-range and down-range directions by moving the source object. This is an added novelty to the operation of NIM lenses,

as focal spot scanning can be achieved without any complex tuning methods [50]. The source was first moved away from the NIM lens and kept at a distance of 15 mm (d_1). The focal spot in this case is found to be at 20 mm(d_2), clearly indicating a shift in the down-range direction (Figure 4-6a). The focal spot moves closer to the lens as the source is moved away from the lens, which is consistent with the imaging theory discussed in Section 2 (equation 3). Also, laterally shifting the source shifts the focal spot laterally. This was demonstrated by moving the source right of the optical axis (along z direction) by 10 mm.

The imaging results for this case show a cross-range shift of the focal spot by approximately the same distance (Figure 4-6b). These results signify that the NIM lens system can be used for source (or defect) localization techniques as well when the position of the source is unknown. It is important to note that the focusing performance degrades as the source is moved away from the optical axis, as seen in the comparison in Figure 4-6a and Figure 4-6b. This is due to the increase of diffraction effects from the edges of the lens as the source is moved towards the sides. Therefore, the range of movement of the focal spot is restricted by the thickness of the lens in the down range direction (equation 3) and by the aperture of the lens in the cross range direction (edge effects).

1.10.3 Subwavelength defect imaging

Next, the capability of imaging subwavelength defects beyond the diffraction limit is demonstrated for NDE applications. The experimental setup is shown in Figure 4-7a. GFRP samples are used as dielectric test objects. The samples are shown in the inset of the Figure 4-7a. A hole of diameter 12 mm (0.25λ) is drilled in the sample of dimensions 100 mm x 100 mm x 8 mm. A similar GFRP sample without the drilled hole is used for deriving a baseline or reference signal (Figure 4-7b). The samples are placed at the focal plane of the lens and C scans are

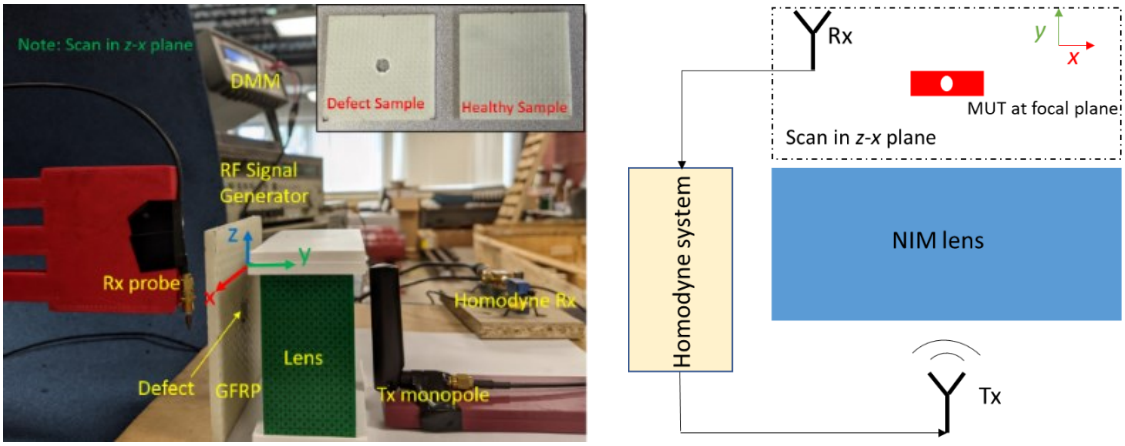

(a) (b)

Figure 0-7 Defect imaging experiment (a) setup and (b)

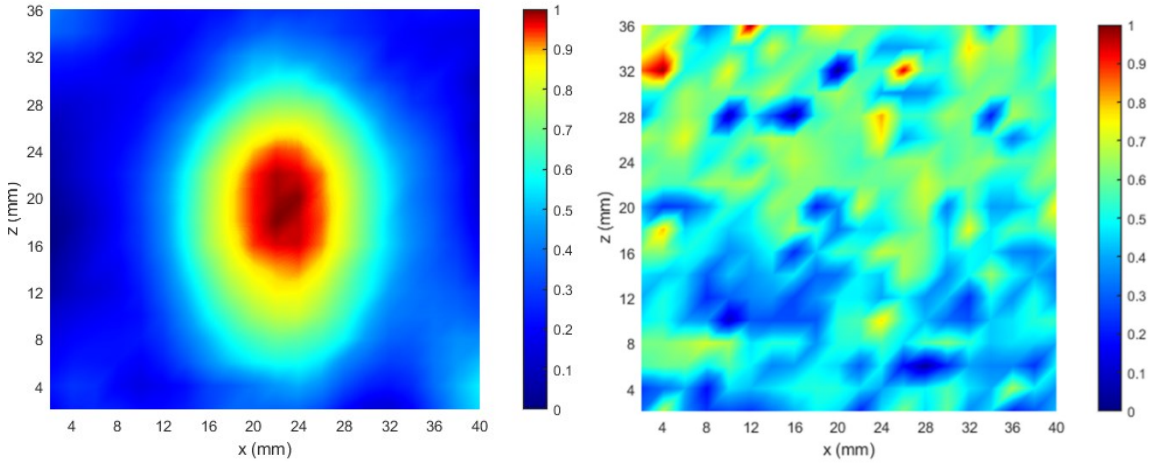

(a) (b)

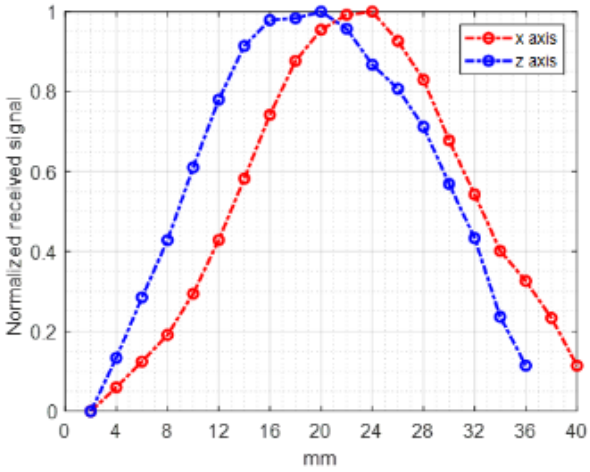

(c)

Figure 0-8 (a) Defect imaging with NIM lens (b) Defect imaging without NIM lens (c) Comparison of cross-range intensity profiles of the images with and without lens.

performed in the *z*-x plane with a step size of 2 mm. The source to test object distance is 80 mm (1.67λ). The contribution due to the defect is measured by the changes in the test signal relative to the baseline signal.

The NDE imaging measurements were repeated without the NIM lens to illustrate that subwavelength defects are not detectable without the lens. The imaging results are displayed in Figure 4-8. It is seen that the subwavelength defect is undetectable without lens (Figure 4-8b) and is imaged using the NIM lens (Figure 4-8a). The lateral intensity profile of the defect image in *x* and *z* direction is shown in Figure 4-7c. The average FWHM of the defect image is 20 mm (0.41λ).

1.11 Proposed NIM Lens Sensor System

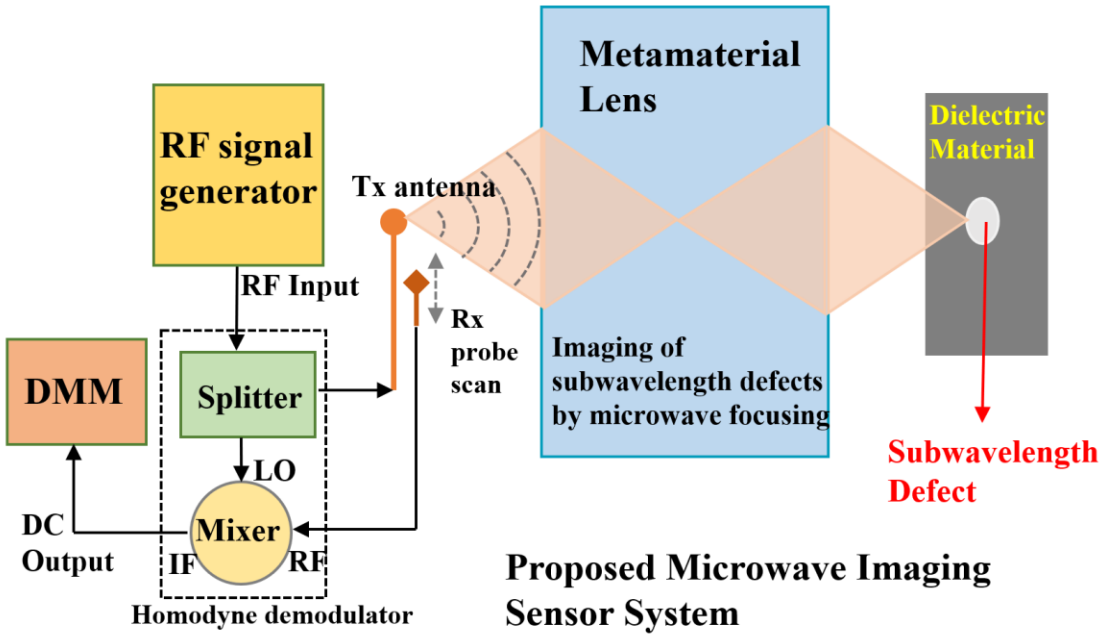

Figure 0-9 (a) Subwavelength defect image with lens (b) Subwavelength defect image without lens (c) Lateral intensity profile of defect image at the focal plane

Using the proposed system, subwavelength defect imaging of dielectric materials in transmission mode has already been reported [38-39]. The system was also used for imaging of subwavelength defects in reflection mode to demonstrate the feasibility of using the system for imaging in single side access. Figure 4-9 presents the schematic of the proposed microwave NDE

sensor for imaging of subwavelength defects. A transmitting monopole antenna is placed in the front focal plane of the NIM lens. The diverging waves from the antenna are bought to focus by the lens at its second focal plane where the dielectric material under test is positioned. The reflected rays from the dielectric material can be sampled at the front focal plane in reflection mode to collect high spatial frequency information and image subwavelength defects. Coherent homodyne detection provides stable access to the information encoded in the phase data by suppressing the excessive noise components [40-41]. High signal to noise ratio associated with such synchronous detection allows the implementation of dispersive NIM lenses in free space under practical conditions without the use of amplifiers or microwave absorbers. Demodulating the image signal into a measurable dc signal also reduces the complexity of the imaging system and hence provides a rapid, low cost solution.

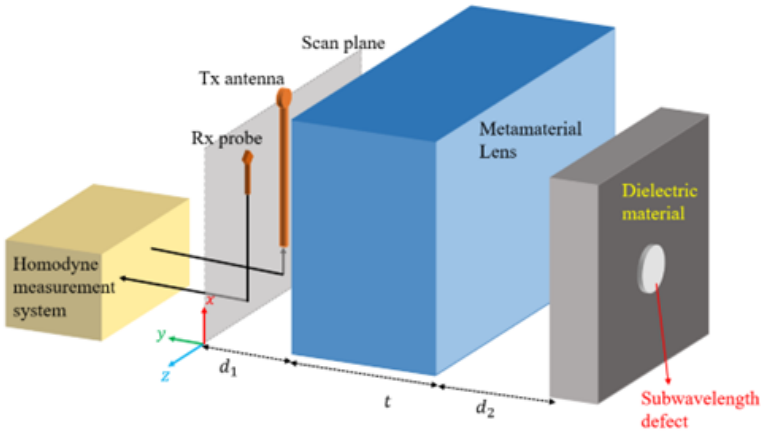

Figure 0-10 Schematic of Microwave NDE experimental setup

The schematic of experimental setup for microwave NDE in reflection mode is shown in Figure 4-10. The reflected waves from the material under test placed at second focal plane (d_2 distance from lens) can be imaged at the first focal plane (d_1 distance from lens) , where the transmitter and receiver are placed. Subwavelength defects inside the dielectric sample can be imaged by performing background subtraction of signals from a healthy sample. The measured

voltage difference at the focal plane will correspond to the contributions due to the defect and can be plotted in a 2D graph to obtain the image of the defect. Two sets of NDE experiments are performed on two types of subwavelength defects: holes and grooves.

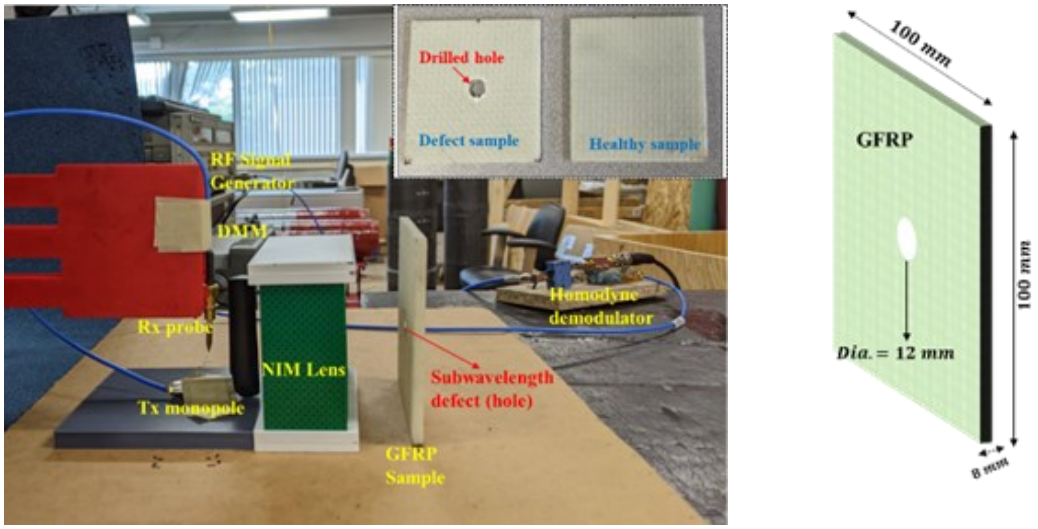

(a) (b)

Figure 0-11 Experiment setup for subwavelength hole imaging (b) GFRP composite sample under test

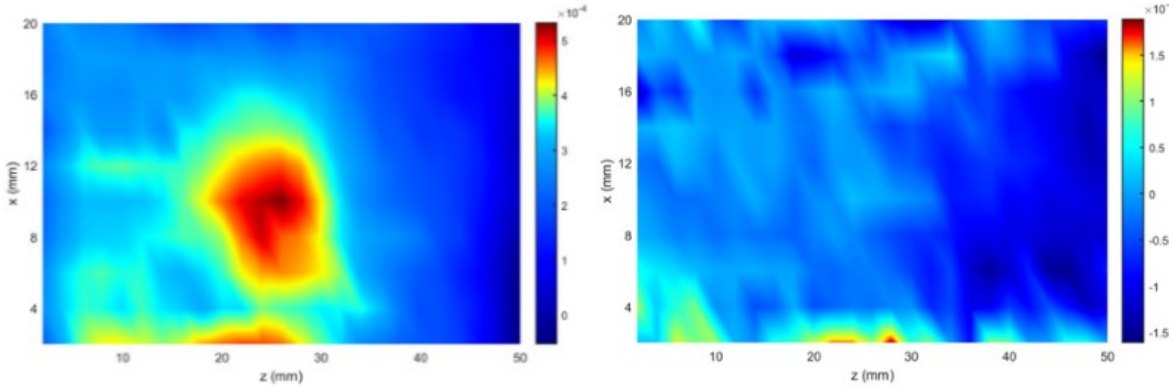

(a) (b)

Figure 0-12 Imaging results (a) with lens and (b) without lens

A drilled hole of diameter 12 mm (0.25λ) in a glass fiber reinforced polymer (GFRP) composite sample is tested first. The GFRP sample is of dimensions 100 mm x 100mm with a thickness of 8 mm. The experiment setup is shown in Figure 4-11a and the sample schematic is shown in Figure 4-11b. A similar sample without any drilled hole is treated as the healthy sample for obtaining the baseline signal for subtraction (inset of Figure 4-11a). The receiver is scanned in

the first focal plane (x-z at d_1) near the source with a step size of 2 mm in both directions. The imaging result for the drilled hole is reported in Figure 4-12a. The presence of subwavelength defect is clearly imaged as indicated by the maxima (location y = 35 mm, z = 50 mm) of the image. The probe to defect standoff distance is 80 mm (1.67λ), which is in the far-field. The experiment was performed without the NIM lens to demonstrate that the subwavelength defect is not detectable in the far-field at large stand-off distances. The imaging result in free space is shown in Figure 4-12b. No detectable variation in measurements is observed in this case and the subwavelength defect goes undetected.

It is observed that the reflection mode imaging results of the same GFRP hole (Figure 4-12a) is worse than the transmission mode imaging results of the same defect (Figure 4-8a). This can be attributed to two reasons. First, in transmission mode imaging, waves have to pass through the lens only once whereas it has to propagate twice in the case of reflection mode imaging. Since NIM lenses are lossy, more losses are introduced in the case of reflection mode imaging, thereby reducing the imaging quality. Introducing amplifiers in case of reflection mode imaging can be a solution to improve the SNR. Second, in case of reflection mode imaging, the transmitter and receiver are placed in close proximity to each other, which results in mutual coupling between the two antennas. Hence, the omnidirectional radiation pattern of the transmitter is affected, resulting in a shift at the focal spot. This ultimately contributes to the degradation of the image as the defect might not be exactly at the focal point. Implementing a receiver antenna with orthogonal polarization to the transmitter antenna can be done to reduce the mutual coupling. Multiple scanning of the samples by placing it at different locations to obtain a better image can be a potential solution to tackle the issue of transmitter receiver coupling.

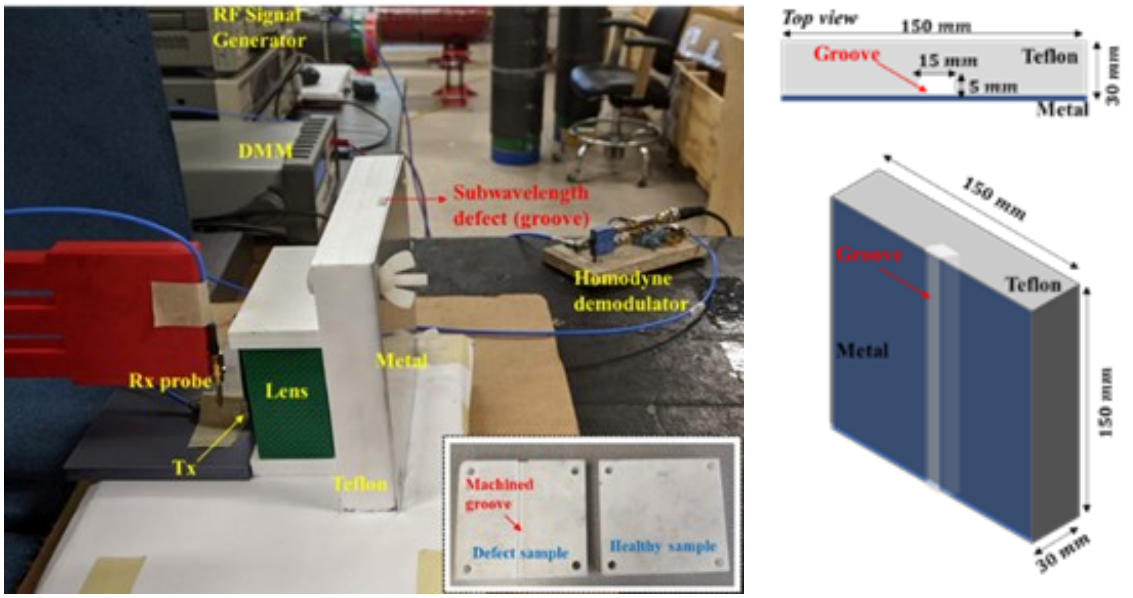

(a) (b)

Figure 0-13 a) Experiment setup for embedded groove imaging (b) Teflon with attached metal sample under test

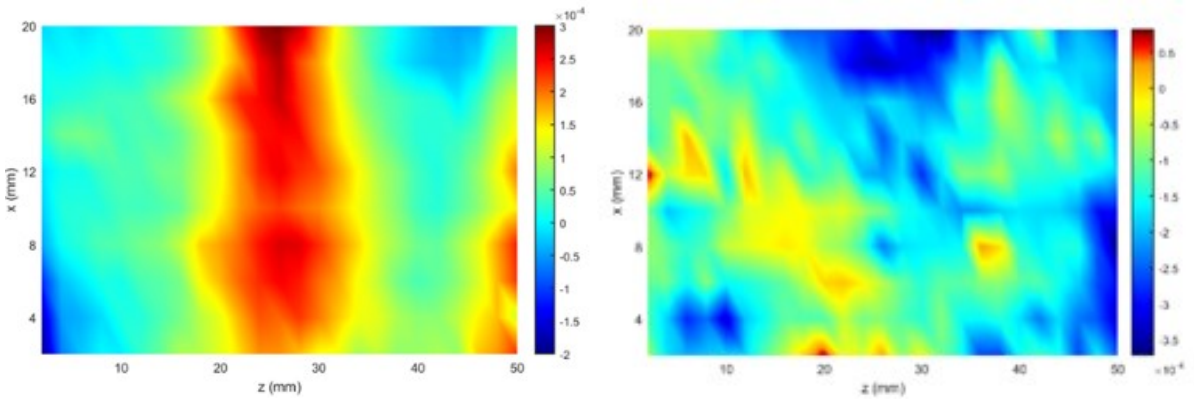

(a) (b)

Figure 0-14 Imaging results (a) with lens (b) without lens

Next, imaging study of a groove of subwavelength dimensions was performed. The sample under test is composed of a Teflon block of dimensions 150 mm x150 mm and a thickness of 30 mm, mounted on an aluminum sheet to simulate a metal-composite joint [51]. Metal-composite joints are prone to disbond defects since air gaps can be introduced in the bonding epoxy layer during manufacturing or usage. Microwaves offer an attractive solution to detect such disbonds in metal composite joints and has been undertaken by various studies [52-54]. The purpose of this

study is to show that subwavelength grooves, which are not typically detectable in the far-field, can be imaged using the proposed system in reflection mode. The simulated disbond is created by machining a groove of dimensions 15 mm (0.31λ) x 5 mm (0.1λ) along the entire length of the sample. The experiment setup and sample schematic are presented in Figure 4-13. Similar to the earlier experiment, the sample with defect is placed at the second focal plane of the lens and the receiver is scanned in the first focal plane with a step size of 2 mm. A Teflon sample without any groove is treated as the healthy sample for baseline subtraction. The defect image results with the lens is plotted in Figure 4-14a. A 1D strip maxima is observed at the center, indicating the presence of the groove. The NDE experiment is repeated without the lens and the corresponding results are shown in Figure 4-14b. Absence of any discernable maxima in free space measurements further validate that subwavelength defects in dielectric materials, which are undetectable in far-field, can be imaged using a properly designed NIM lens.

NIM lens designs discussed in Chapter 3 and 4 provide access to the evanescent wave components due to their negative refractive index. Subwavelength imaging at large stand-off distances is possible using NIM lenses. However, such NIM lenses have some limitations, which restrict their usage and implementation.

The source and focal spot distance is limited by the thickness of the lens according to (2.6). This restricts the stand-off distance for NDE imaging using NIM lenses. The lens designs discussed are also bulky in nature and losses associated with fabricated NIM lenses restricts the “super resolution” capability. The SRR-wire NIM lens designs are also narrowband device since negative refractive index phenomena is observed over a small range of frequencies. Due to these limitations of NIM lenses, an alternative metamaterial lens design is investigated and its feasibility for imaging is studied in the following chapter.

GRADIENT-INDEX METASURFACE LENS

In the preceding work, metamaterial lenses have been constructed from periodic array of identical unit cells, and the resulting effective medium can be considered homogeneous in the sense that the averaged electromagnetic response does not vary over the structure. However, metamaterials whose effective electromagnetic properties vary spatially can also be fabricated. Such functionally graded metamaterials can be used for lensing applications. This chapter discusses metamaterial lens design based on ELC resonator unit cells, in which a spatially varying refractive index is introduced by a slight change in the properties of each successive unit cell. The parameters of the metamaterial lens medium are chosen in a way such that a relatively constant gradient in the index occurs along one axis of the metamaterial, perpendicular to the direction of propagation [69].

Despite their super resolution capabilities, NIM lenses discussed in previous chapters still have one fundamental limitation: inability to focus plane waves into a focal spot which forms the basis of Fourier transform and imaging capabilities of a conventional lens [35]. NIMs also tend to be narrowband and highly dispersive structures since they operate in the resonant region of the unit cells. In 2005, the concept of NIM was extended to graded metamaterials, where it was shown that metamaterials whose effective electromagnetic properties vary spatially can also be fabricated by introducing a slight change in the properties of each successive unit cell [36]. This paved the way for numerous unprecedented applications of metamaterials including GRIN metamaterial lenses, which can provide phase compensation mechanisms and bring plane waves into focus [37]. A GRIN metamaterial lens also operates in non-resonant regions of its unit cells and hence overcomes the narrowband and large transmission losses associated with NIM lenses [38].

The idea of GRIN lenses was theorized by Maxwell back in 1854, when he described remarkable imaging capabilities of a sphere with a radially symmetric refractive index [39]. Such gradual refractive index variation can be used to construct flat lenses, where bending of incident waves is achieved through the refractive index contrast rather than the curved surface of conventional lenses. Classic examples of GRIN lenses include the Fresnel lens, Wood lens and Luneburg lens [40-43]. The advent of metamaterials and metasurfaces have renewed interest in research of GRIN lenses and inspired numerous works [44-50]. The tailorable properties and flat geometry of metasurfaces has provided ground-breaking engineering potential for GRIN lens designs, which was not possible with conventional dielectrics.

ELC resonators provide an attractive alternative to the conventional metamaterial designs based on SRRs [70][71]. The propagation vector of the incident wave in ELC designs is into the plane of the unit cell, in contrast to SRR designs where the propagation vector is parallel to the plane of the unit cell. This allows design of planar metamaterial structures or metasurfaces, which are desirable in terms of fabrication as well as implementation [72][73]. Although negative index physical properties are not utilized in GRIN lens design, the source and focal distance is not limited by the thickness of lens as is the case for NIM lens (2.16). Further, high gain horn antennas instead of monopole antennas can be used as the source in the case of GRIN lens design, resulting in much greater stand-off distances in comparison to NIM lenses operating at similar frequencies. In addition to this, GRIN lenses are also wideband devices in contrast to the narrowband NIM lenses, making them more suitable for imaging a wide range of defect sizes.

This chapter presents the design of a GRIN metasurface lens operating at 8 GHz. The resonant frequency, and consequently the refractive index of the ELC unit cell is gradually varied by varying the split-gap dimensions of the ELC resonator. A spatially varying refractive index

profile perpendicular to the direction of incident wave is generated by appropriate variations in parameters of the ELC unit cell. Theory behind the operation of GRIN lenses and ELC unit cells is discussed to guide the design procedure. A lens of thickness 0.6 mm (.016λ) and a focal spot distance of 110 mm (2.93λ) was chosen for the design. The desired gradient phase profile of the lens is generated using numerical parametric study of the ELC unit cell. Extraction of refractive index profile from the parametric numerical results was done to verify with geometric optics calculations. Numerical simulation of the full lens design consisting of 10x18 unit cells in Ansys HFSS was done to study the performance of the lens.

1.12 Theory

1.12.1 ELC Unit cell

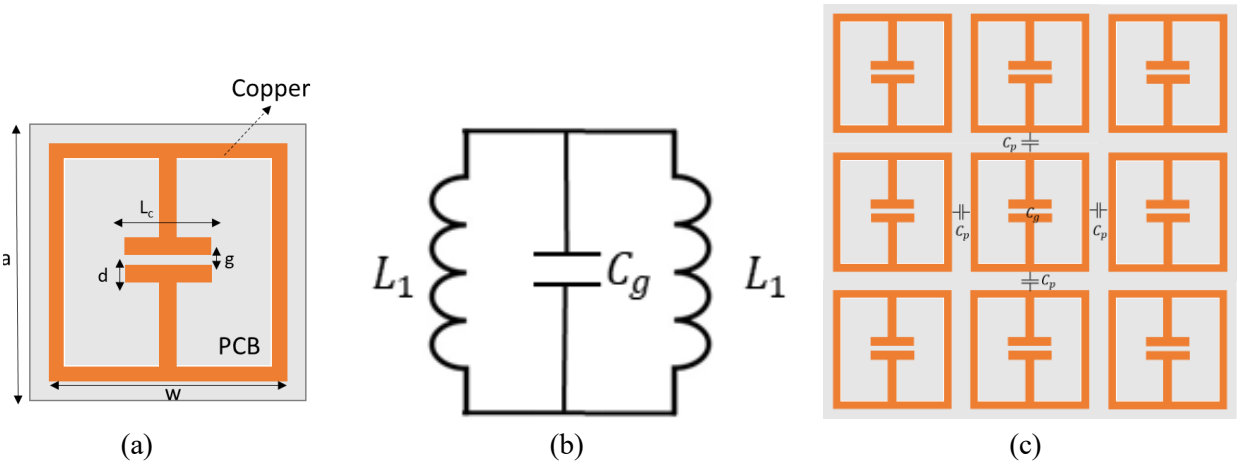

(a) (b) (c)

Figure 0-1 (a) ELC unit cell resonator with dimensional parameters (b) Equivalent circuit of single ELC resonator. (c) A 3x3 array of ELC resonators showing the inter cell capacitance C_P

Schurig et al. proposed an inductive - capacitive resonator also known as electric-field-coupled LC (ELC) resonator as shown in Figure 5-1a [70] . This resonator has a split gap at the center of the structure providing capacitance (which couples strongly to an applied electric field parallel to the split gap) and two loops in parallel at the sides to provide inductance in the structure. An equivalent circuit of the resonator has been shown in Figure 5-1b. The resultant resonant frequency ω_o can be expressed as

$$\omega_o = \frac{1}{\sqrt{LC}} \tag{0.1}$$

where L and C are the total inductance and capacitance of the structure respectively. When the resonator is excited by a uniform magnetic field parallel to the split-gap, current induced in the two loops are in opposite direction leading to zero magnetic moment. Thus, the structure does not provide magnetic coupling and only the capacitive C element drives its fundamental resonance by (5.1).

The total capacitance C of the ELC unit cell is related to the gap capacitance C_g and inter cell capacitance C_{po} by [74]

$$C = \frac{C_g C_{po}}{C_g + C_{po}} \tag{0.2}$$

The gap capacitance C_g is given by

$$C_g = \frac{\epsilon_{reff} 10^{-3}}{18\pi} \frac{K(k)}{K'(k)} L_c \tag{0.3}$$

where, ϵ_{reff} is the effective permittivity of the unit cell, L_c is shown in Figure 5-1a. ϵ_{reff} is given by the equation

$$\epsilon_{reff} = \epsilon_0 \left(1 + \frac{(\epsilon_r - 1)}{2} \frac{K(k_1)}{K'(k_1)} \frac{K'(k)}{K'(k)}\right) \tag{0.4}$$

The approximated ratio between the elliptic integrals of first kind $K(k)$ and its complement $K'(k)$ reads

$$\frac{K(k)}{K'(k)} = \begin{cases} \frac{1}{\pi} ln\left[2\frac{1+\sqrt{k}}{1-\sqrt{k}}\right] \; for\; 0.707 \leq k < 1 \\ \frac{\pi}{ln\left[2\frac{1+\sqrt{k'}}{1-\sqrt{k'}}\right]} \; for\; 0 \leq k < 0.707 \end{cases} \tag{0.5}$$

The variables k and $k'$are related to the ELC resonator dimensions by the following equations

$$k = \frac{g}{2d+g} \tag{0.6}$$

$$k' = \sqrt{1-k^2}$$

$$k_1{}' = \frac{\tanh\left(\frac{\pi g}{4h}\right)}{\tanh\left(\frac{\pi\left(d+\frac{g}{2}\right)}{2h}\right)}$$

$$k_1{}' = \sqrt{1-k_1{}^2}$$

g and d are shown in Figure 5-1a and h is the thickness of the substrate. The inter cell capacitance C_p shown in Figure 5-1c can be calculated the same way and the total inter-cell capacitance in equation (5.2) is given by $C_{po} = 4C_p$.

The total inductance L in the unit cell is related to the ELC dimensions by the equation,

$$L \approx \mu_0 h\left(2\frac{d}{w} + 2\frac{w}{d} + \frac{w-2d-g}{d}\right) \tag{0.7}$$

where w is shown in Figure 5-1a. It can be clearly observed from these equations that the split gap dimensions g can be varied to change the ϵ_{reff} and hence the refractive index ($n^2 = \mu_{eff}\epsilon_{eff}$) and resonating frequency ω_o of the unit cell.

1.12.2 GRIN Lens

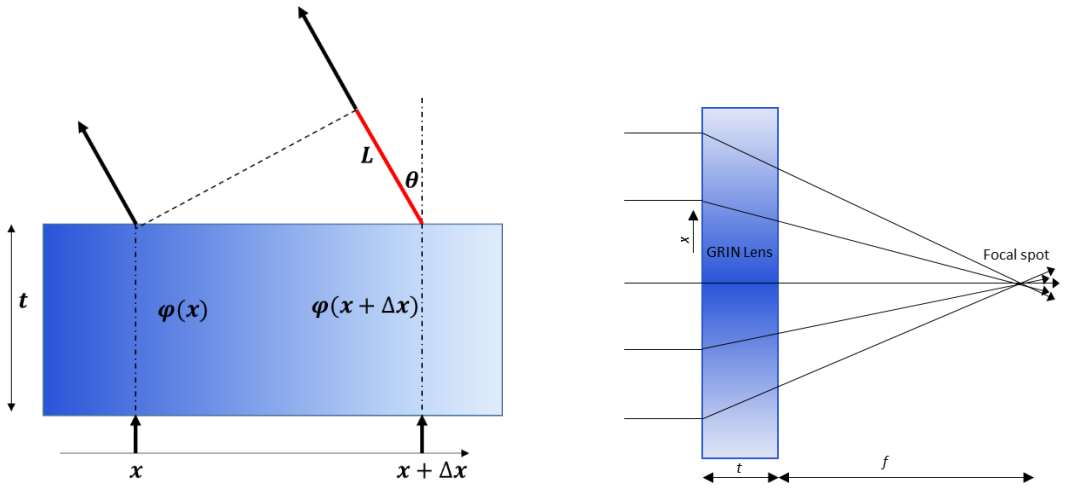

(a) (b)

Figure 0-2 (a) Deflection of a beam by a structure whose refractive index possesses a gradient that is constant. Shading of the sample indicates the gradient in the index: darker shading corresponds to a higher index value. (b) GRIN lens operating with a lens thickness t and focal spot f

The operation of a gradient index lens can be understood by observing the deflection of a beam incident on a planar metamaterial slab whose refractive index varies linearly in a direction perpendicular to incident radiation. To calculate this deflection, two normally incident but offset rays entering a gradient index planar slab of thickness t, as shown in Figure 5-2a. The rays will undergo different phase changes as they propagate through the slab. Assuming the two rays enter at locations x and $x + \Delta x$ along the slab face, then the phase difference of the two beams with thickness into the slab is given by [69],

$$\varphi(x + \Delta x) - \varphi(x) \sim kt \frac{dn}{dx} \Delta x \tag{0.8}$$

where k is the propagation constant and $\frac{dn}{dx}$ is the index gradient. The acquired phase difference must be equal to the phase advance across the path L marked in Figure 5-2a. Therefore,

$$\sin\theta \sim t \frac{dn}{dx} = t \frac{dn}{d\omega_o} \frac{d\omega_o}{dg} \frac{dg}{dx} \tag{0.9}$$

which shows that if the split-gap $g(x)$ is varied gradually as a function of distance along the metamaterial slab, a spatial gradient index can be generated so that an incident beam is deflected by an angle θ.

A GRIN lens consists of such a metamaterial slab with spatially varying refractive index as shown in Figure 5-2b. Using geometric optics, the optical path $p(x)$ of an arbitrary ray located at x can be written as [75],

$$p(x) = \sqrt{f^2 + x^2} + n(x)t \tag{0.10}$$

where f is the focal point and $n(x)$ is the spatial distribution of the refractive index. For all the rays to converge to a single focal point, the optical path lengths of arbitrary off-axis rays should equal to those passing exactly at the optical axis. This results in the profile of gradient index $n(x)$ for GRIN lens expressed as,

$$n(x) = n_0 - \frac{1}{t}\left[\sqrt{f^2 + x^2} - f\right] \tag{0.11}$$

where n_0 is the maximum refractive index at the center of the lens. For ELC resonators, a smaller split gap will correspond to a larger capacitance and consequently a higher refractive index. Hence, a symmetric array of such ELCs, with increasing split-gap from the middle, will generate the required refractive index profile for focusing. Incident waves from both the edges of the lens will be refracted towards the higher refractive index unit cells at the center, thus allowing for focusing to occur. For bending and focusing of waves using graded refractive index lenses, the spatial distribution of the phase shift, φ across the lens should obey the following equation [73]

$$\varphi(x) = \frac{2\pi\left(\sqrt{f^2 + x^2} - f\right)}{\lambda} \tag{0.12}$$

where x is the position on the lens in the x-direction and the center of the lens is at $x = 0$, f is the focal length of the lens, and λ is the operating wavelength.

1.13 Simulation

1.13.1 Unit cell

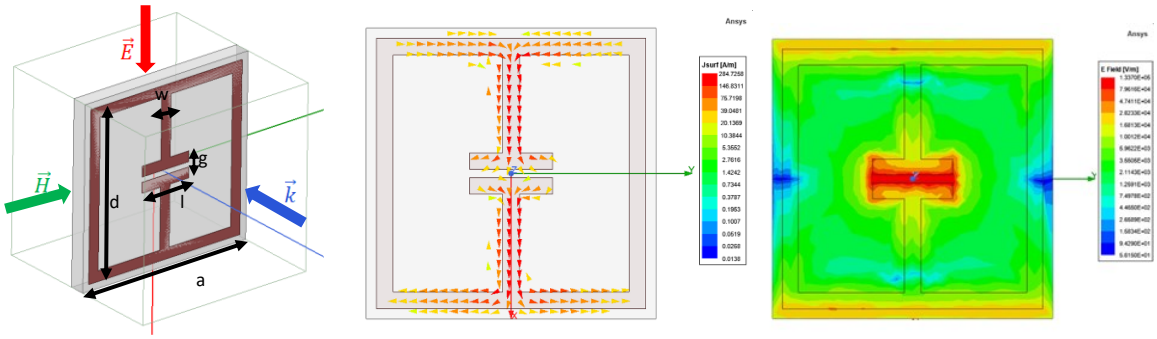

(a) (b) (c)

Figure 0-3 (a) GRIN Lens Unit Cell schematic and incident wave polarization (b) Transmission magnitude parametric simulation results (c) Phase shift parametric simulation

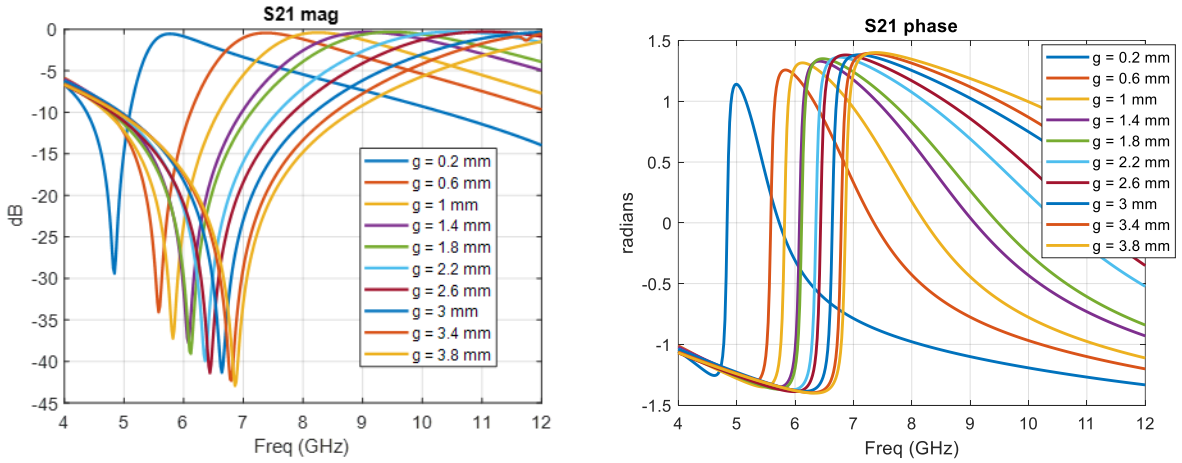

(a) (b)

Figure 0-4 (a) GRIN Lens Unit Cell schematic and incident wave polarization (b) Transmission magnitude parametric simulation results (c) Phase shift parametric simulation results.

The ELC unit cell HFSS model, with the incident wave polarization and dimensional parameters, is shown in Figure 5-3a. The dimensional parameters for the unit cell design are: a = 7mm, d = 6.5 mm, l = 2 mm. Periodic boundary conditions are used to obtain the scattering parameters for the unit cell in a metamaterial arrangement. Figures 5-3b and 5-3c plot the surface current density and electric field distribution, respectively, as obtained from HFSS numerical

results. The surface current density plot shows that there is no net circulation of current in the unit cell due to clockwise and counterclockwise components in adjacent areas of structure as expected. The electric field distribution plot shows a strong local field enhancement in the capacitive gap at the center of the unit cell. The frequency response of the unit cell is varied by varying the split-gap *g*. The nominal split-gap *g* for highest refractive index unit cell is taken as 0.2 mm due to fabrication limits. The PCB material used is FR4 with a thickness of 0.6 mm and trace width (*w*) of 0.4 mm. Parametric unit cell study was done for varying values of split-gap *g,* ranging from 0.2mm to 4 mm to obtain varying phase shifts and determine the frequency of operation of the lens. Figures 5-4a,b show the parametric S_{21} magnitude and phase results for 10 representative cases obtained using HFSS. 8 GHz was chosen as the frequency of operation from the parametric results to maximize transmission through the lens (S_{21} magnitude) and achieve high phase shift between the individual unit cells (S_{21} phase) simultaneously.

1.13.2 GRIN lens

The desired phase profile of the lens of thickness 0.6 mm operating at 8 GHz for a focal distance of 110 mm follows (3) and is plotted in Figure 5-5a. The numerical phase shift results from the model-based parametric study were used to determine unit cells with appropriate split-gaps and obtain an approximation to the desired phase profile. The proposed GRIN metasurface lens design consists of 18x20 unit cells in the x-y plane as shown in Fig. 5c. The lens has a total dimension of 126 mm (3.36λ) x 140 mm (3.72λ) x 0.6 mm (.016λ). The simulated phase profile of

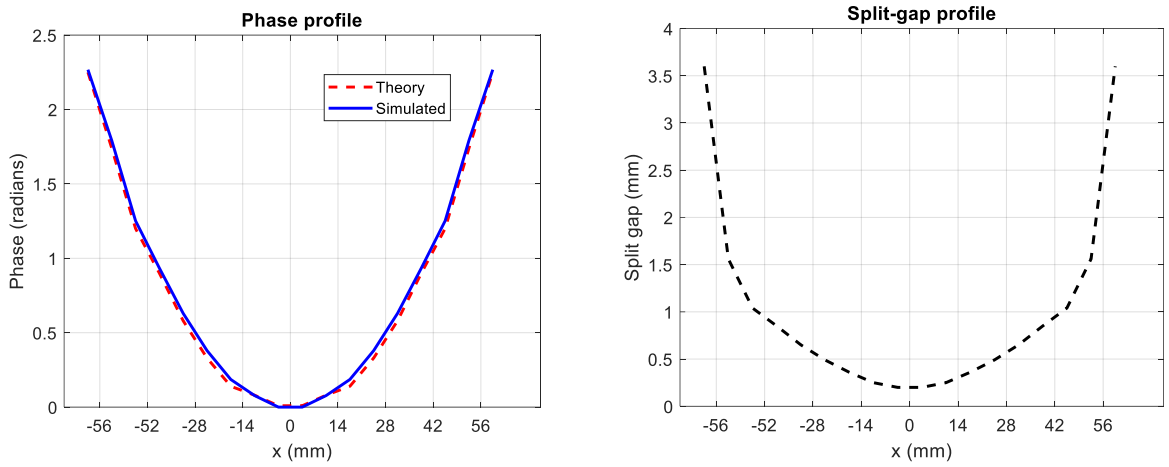

(a) (b)

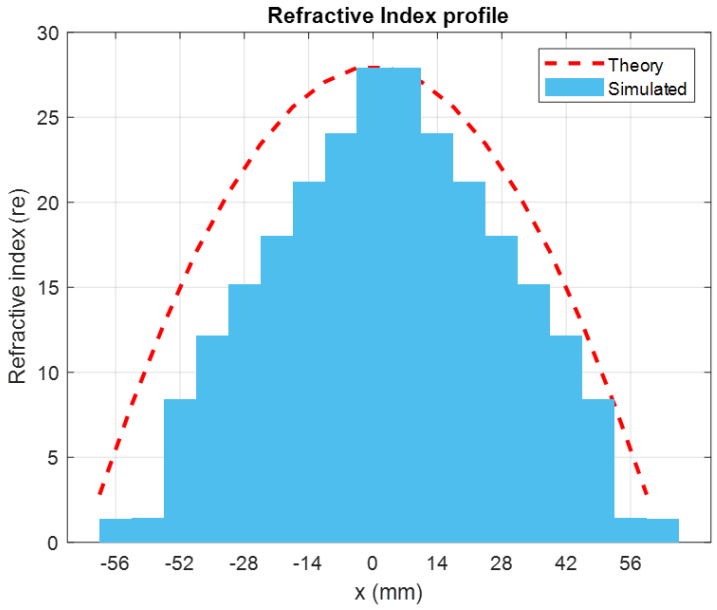

(c)

Figure 0-5 Simulated gradient profile. The center of the lens is at x=0. (a) Theoretical and simulated phase profile comparison. (b) Requisite split-gap profile. (c) Theoretical and simulated refractive index profile comparison.

the final lens design is also plotted in Fig. 5a. A higher phase shift is observed for larger split-gap unit cells as expected.

Electromagnetic parameter retrieval according to Appendix of [34] was done for the 18 unit cells to extract the refractive index profile. The highest refractive index (no in Equation 1) at the center of the GRIN lens is 27.91 for the proposed design at 8GHz. The simulated refractive index profile is plotted in Figure 5-5c. The theoretical refractive index profile according to (2) is

plotted as well to demonstrate the correlation between the geometric optics and full wave electromagnetism. The difference in the theoretical and simulated gradient index profile is due to the approximations of EM waves as straight rays in geometric optics which does not consider effects such as scattering and diffraction. Although it has been argued that assigning bulk material properties to metasurfaces using a variant of Nicholson Ross Weir method may produce ambiguous results [55-56], they can still be used to characterize metasurfaces if the thickness of the metasurface remains constant [19].

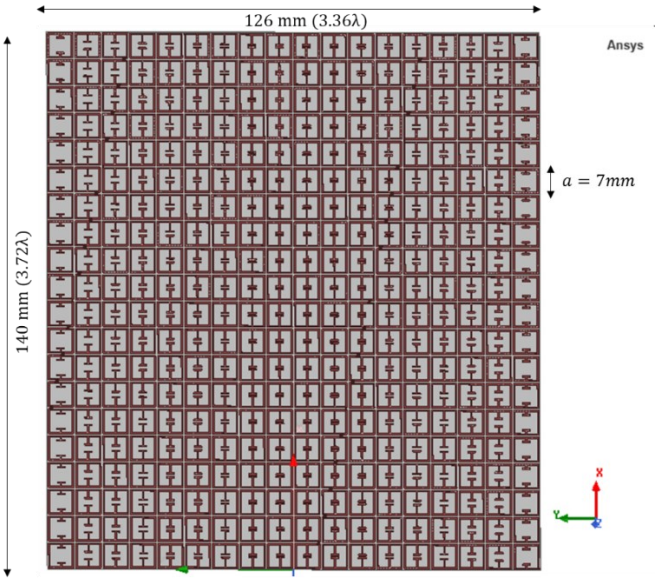

Figure 0-6 Proposed GRIN lens design. GRIN Lens Design. The lens design consists of 18x10 unit cells in the x-y plane.

The full GRIN lens design considered consists of 18x10 unit cells in the *x*-*y* plane as shown in Figure 5-5. The lens has a total dimension of 126 mm (3.36λ) x 70 mm (1.86λ) x 0.6 mm (.016λ). Full wave simulation of an incident spherical wave with *E* field polarized along the *x*-axis was done in Ansys HFSS to show the focusing action. A waveguide was used as the source of spherical waves and kept at a distance of 150 mm (4λ) from the lens. A focal spot is obtained around 110 mm (2.93λ) from the plane of the lens as seen from the *E* field distribution in Figure 5-6a. Figure 5-6b shows the full wave simulation without the GRIN lens. The source to focal spot distance

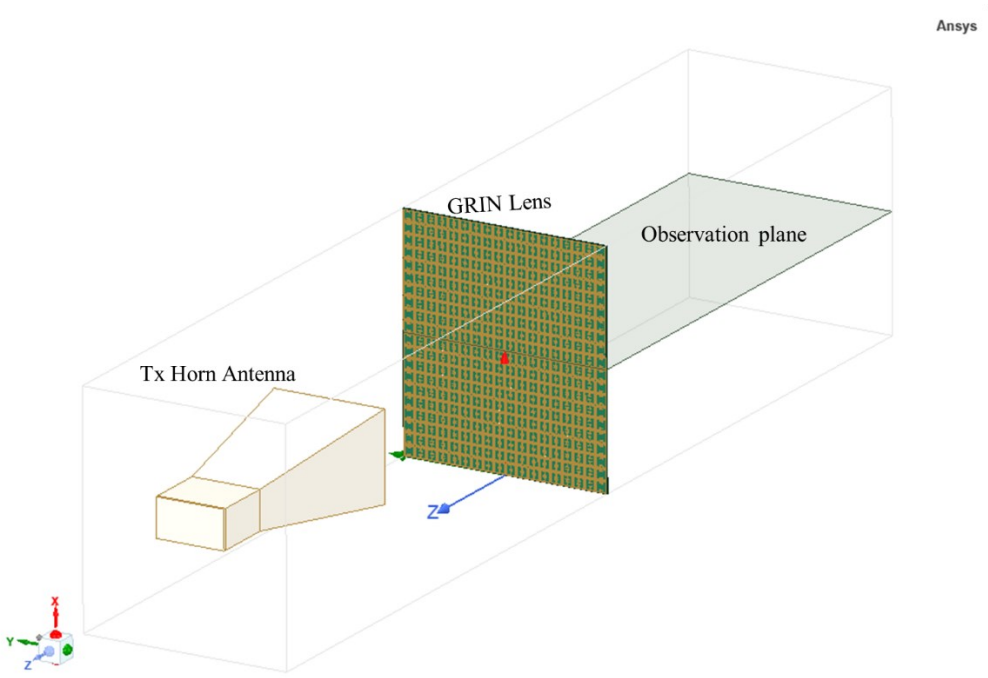

(a)

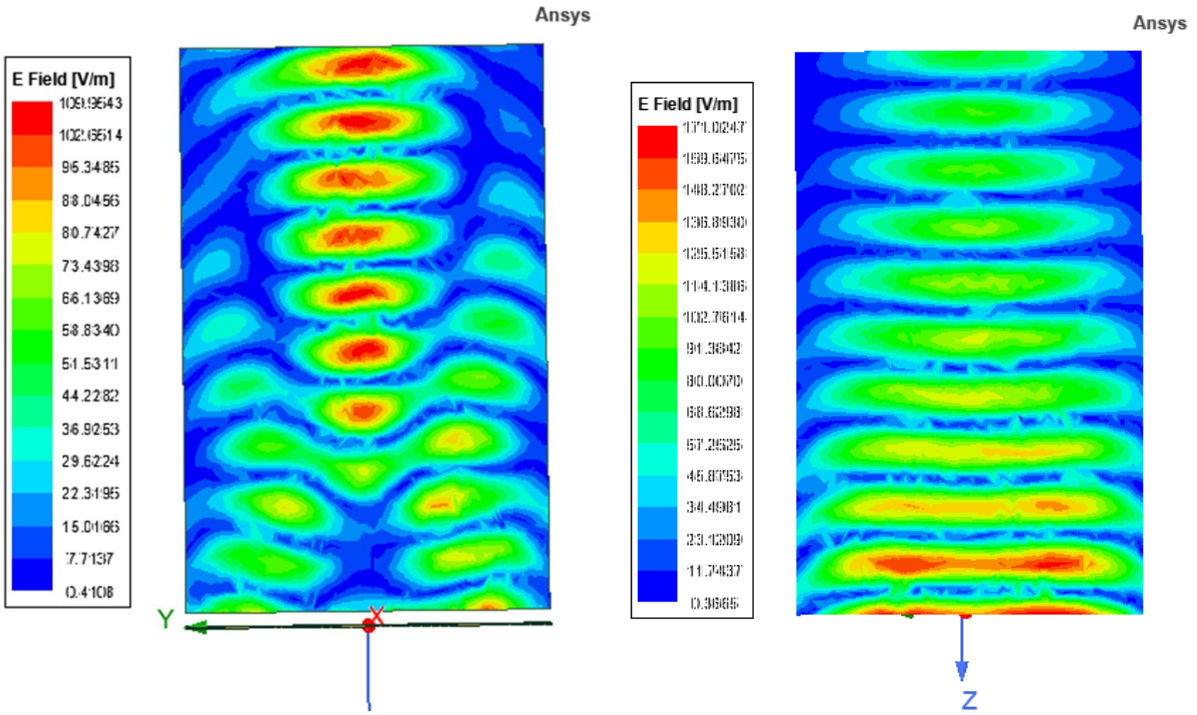

(b) (c)

Figure 0-7 (a) HFSS setup for focusing simulation (b) Simulated E field distribution with lens (c) Simulated E field distribution without lens.

(stand-off distance) is 6.94λ for GRIN lens while it was 2.29λ and 1.8λ for the S and C band NIM designs respectively.

Full wave simulation of incident plane waves was done in HFSS to illustrate the focusing action. The geometrical setup modeled by HFSS is shown in Figure 5-7a. The GRIN lens is placed on the *x*-*y* plane and centered at the origin. The gradient of index is along *y* while the wave propagation direction is along *z* direction. A horn antenna with its *E* field polarized along the *x*-axis is used as the source of incident EM waves and kept at a distance of 200 mm (5λ) from the lens. Open boundary conditions are used to simulate the structure in free space. The magnitude of the simulated *E* field distribution is plotted on a *y*-*z* observation plane on the other side of the lens. In Figure 5-7b, the waves can be seen to refract towards the center after passing through the GRIN lens and come to focus close to the designed focal length of 110 mm (2.93λ) from the plane of the lens. Figure 5-7c shows the full wave simulation without the GRIN lens. *E* field distribution without the lens shows the incident plane waves from the horn antennas propagating without any focusing action.

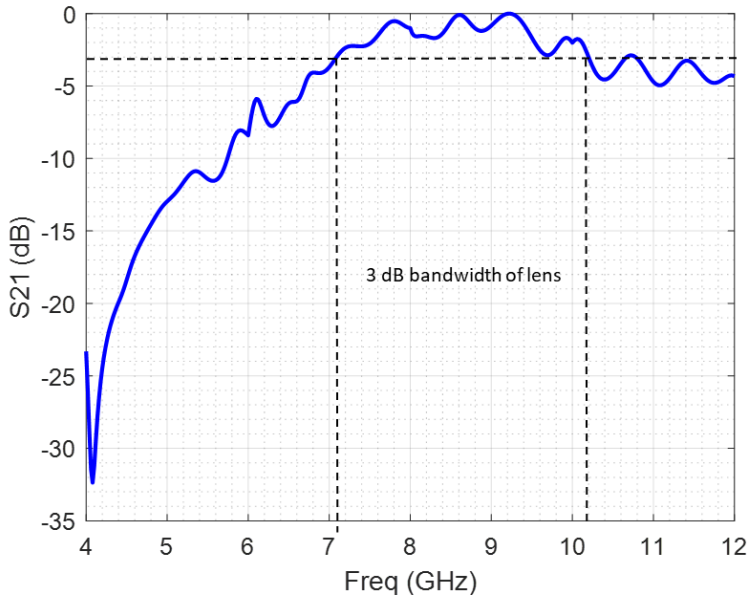

Figure 0-8 S_{21} simulation results of full lens for 3 dB bandwidth.

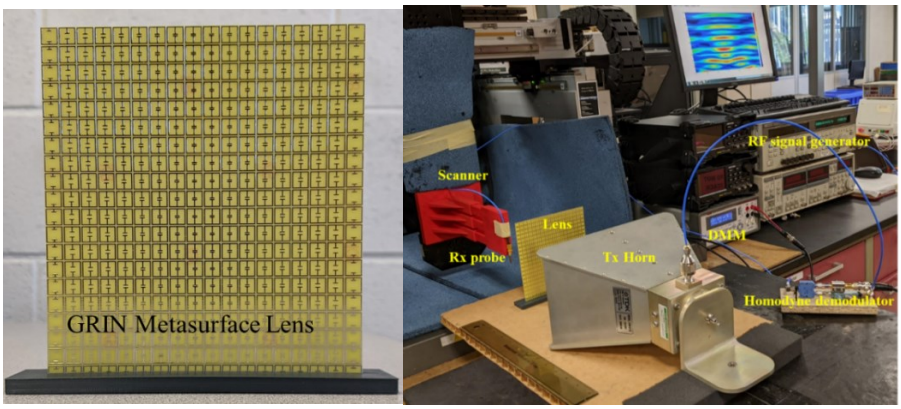

(a) (b)

Figure 0-9 (a) Fabricated GRIN Metasurface Lens. (b) Experiment setup using homodyne imaging system.

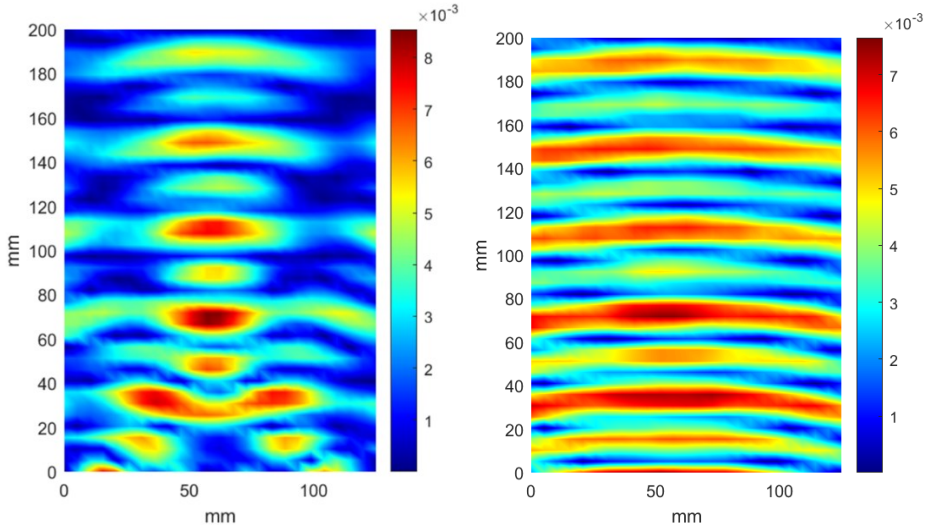

(a) (b)

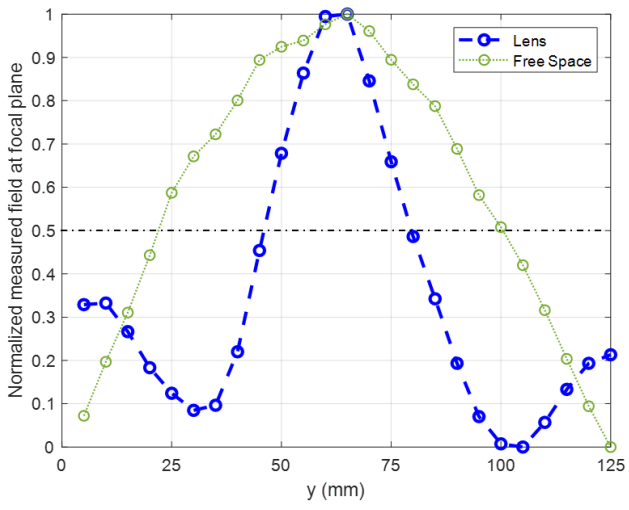

(c)

Figure 0-10 (a) Measured field distribution with lens. (b) Measured field distribution without lens. (c) Normalized measured field at focal plane.

Figure 5-8 plots the simulated S_{21} results of the full lens design using two waveguides as transmitter and receiver. From the graph, the 3 dB bandwidth for the proposed lens is 3.12 GHz (7.08 GHz to 10.2 GHz).

1.14 Experiment

A prototype of the proposed GRIN metasurface lens was fabricated for experimental verification. The fabricated lens is shown in Figure 5-9a. A homodyne detection scheme described in [34] was used to perform the microwave imaging experiments at 8 GHz. A wideband horn antenna was used as the source of plane waves. The horn was kept at 200 mm from the metasurface lens. A quarter wavelength monopole is used as the receiver to sample the field after it passes through the lens. The experimental setup is shown in Figure 5-9b. Figures 5-10a and 5-10b shows the measured field distributions with and without the lens. From the plots, focusing action of the fabricated metasurface lens is clearly observed and they match well with the numerical results as shown in Figure 5-7. The cross range field distribution in the focal plane (110 mm) with and without the lens is plotted in Figure 5-10c. The full width at half maxima (FWHM) at the focal plane with the lens is 33 mm (0.88λ) and is 77 mm (2.04λ) without the lens, indicating a resolution enhancement by a factor of 2.33 that is achieved with the proposed lens.

1.15 Proposed GRIN Metasurface Lens

1.15.1 Simulation

The GRIN lens described in the previous section has a gradient index in only one direction and hence the focusing action was in the azimuthal plane only. The same design concept was extended for a two directional gradient metasurface lens design and is reported in this section. The focusing action in this case will occur both in the vertical and horizontal plane and hence a point focus can be obtained for microwave imaging applications. The proposed GRIN lens design is shown in Figure 5-11 and consists of 17x17 unit cells with dimensions of 119 mm (3.2 λ) x 119 mm (3.2 λ) x 0.6 mm (0.016 λ).

The HFSS model setup to validate focusing action is shown in Figure 5-12. Two observation planes (both horizontal and vertical) are considered in this case. The solution frequency is 8 GHz, which is same as the 1D GRIN lens. The electric field distribution in the horizontal plane is shown in Figure 5-13a. A similar focusing action is observed with the GRIN lens, while the free space results show the incident plane waves without any focusing. The predetermined focal length for this design is 100 mm. The vertical observation plane is placed at the focal plane (100 mm from the GRIN metasurface lens) and the electric field distribution is plotted in Figure 5-14 to observe the point focusing action. Symmetric refraction of incident waves produces a circular confinement of electric field in the focal plane as observed in Figure 5-14a. The electric field distribution without the GRIN lens is plotted as well (Figure 5-14b) to indicate the resolution enhancement.

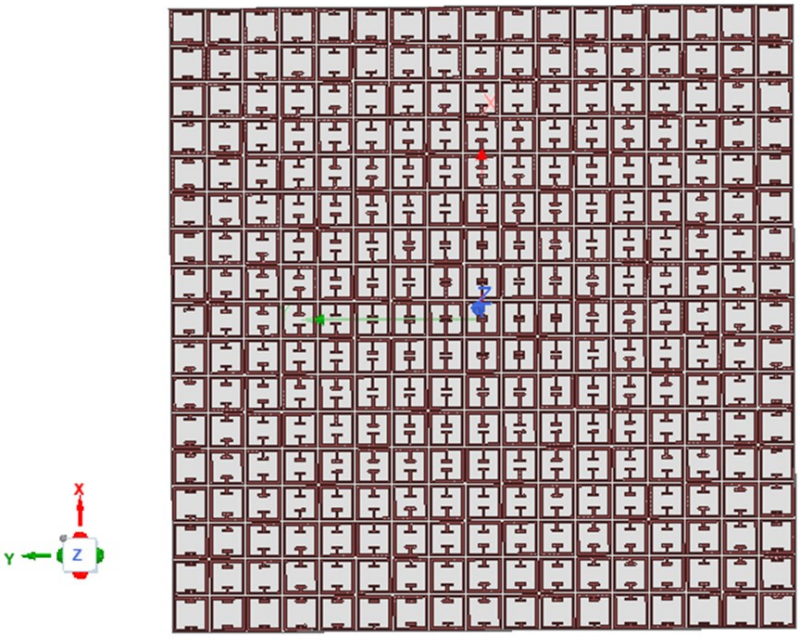

Figure 0-11 Proposed GRIN Metasurface Lens

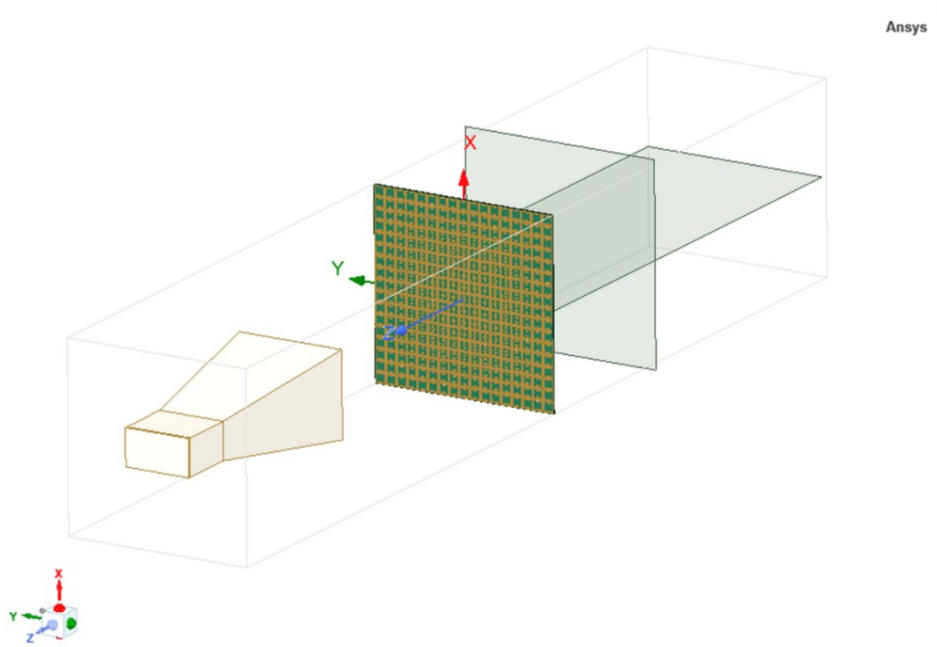

Figure 0-12 Ansys HFSS experiment setup.

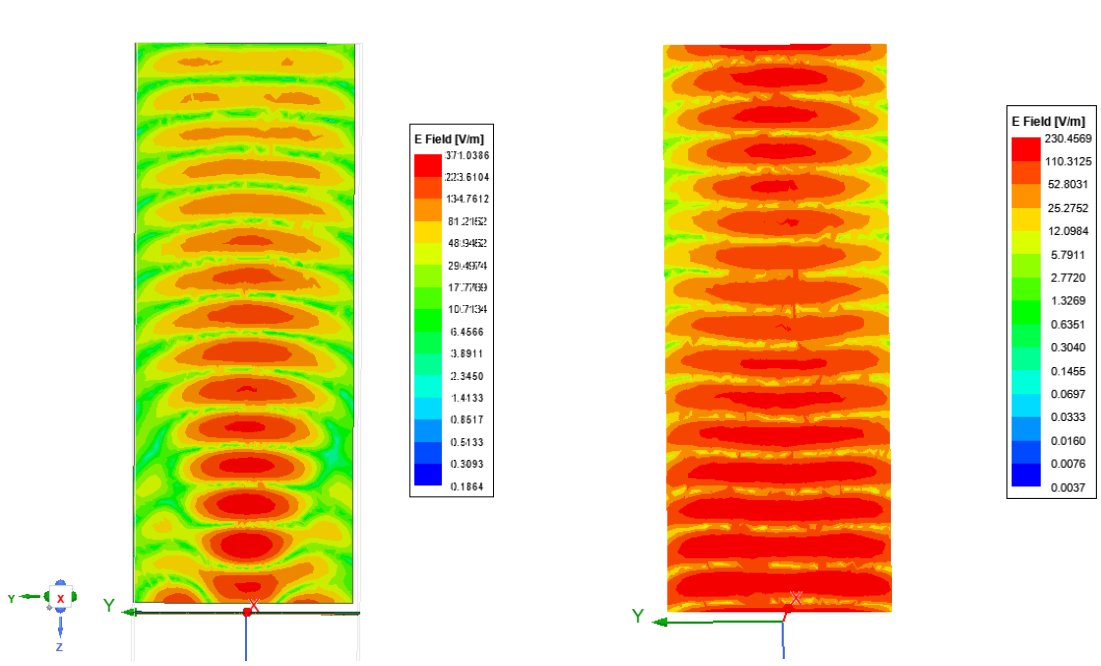

(a) (b)

Figure 0-13 Azimuthal plane electric field distribution (a) with lens (b) without lens

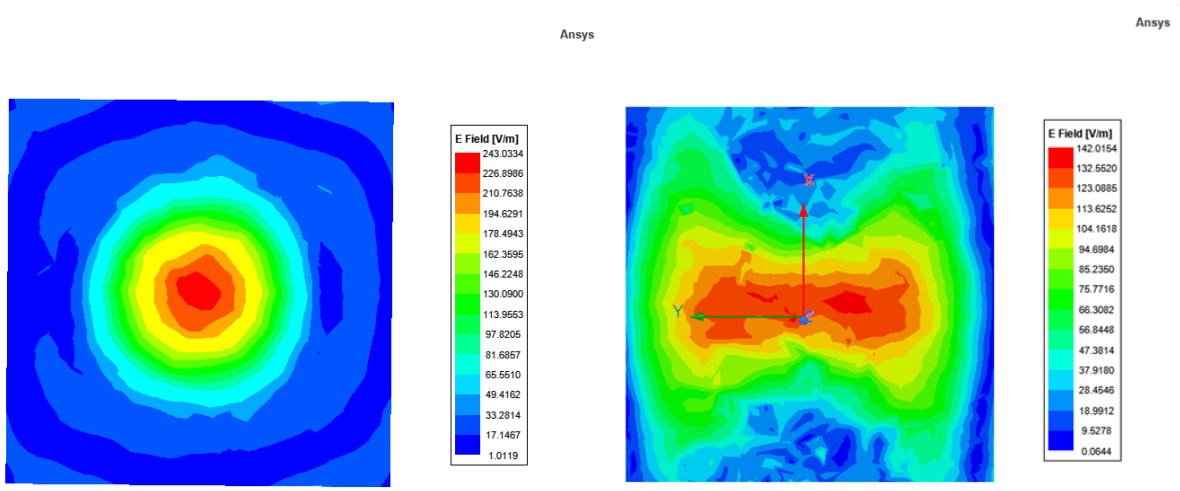

(a) (b)

Figure 0-14 Vertical plane electric field distribution (a) with lens (b) without lens.

1.15.2 Experiment

The prototype of the 2D GRIN lens is shown in Figure 5-15. The homodyne setup described in previous sections was used to perform the experiments. A horn antenna kept at a distance of 200 mm was used as the source of incident plane waves. A quarter wave monopole was used to sample the field distribution in the horizontal as well as the vertical plane. The experiments were performed without the lens as well to validate the focusing action of the lens. The horizontal field distribution is plotted in Figure 5-16 and compares well with the simulation results shown in Figure 5-13. The vertical observation plane is located 100 mm from the lens surface and the experimental results are shown in Figure 5-17. A circular focal spot is obtained with the GRIN lens as expected (Figure 5-17a). The experiment is repeated without the lens to calculate the resolution enhancment. The FWHM with lens is 40 mm (1.2λ) and without lens 70 mm (1.86λ) indicating a resolution enhancment by a factor of 1.5 (Figure 5-17c).

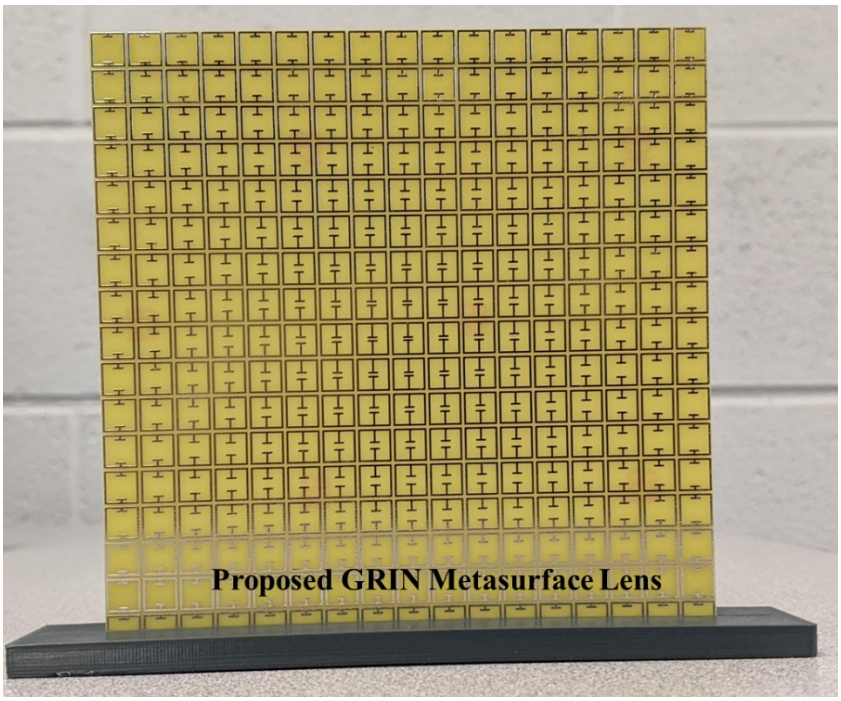

Figure 0-15 Prototype of proposed 2D GRIN Metasurface Lens

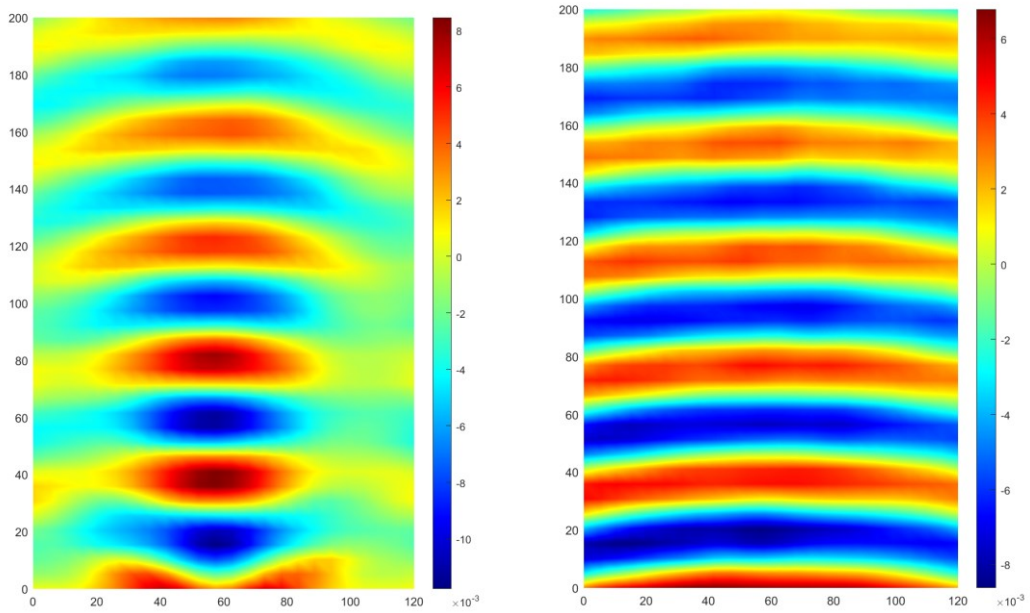

(a) (b)

Figure 0-16 Field distribution in horizontal plane (a) with lens (b) without lens

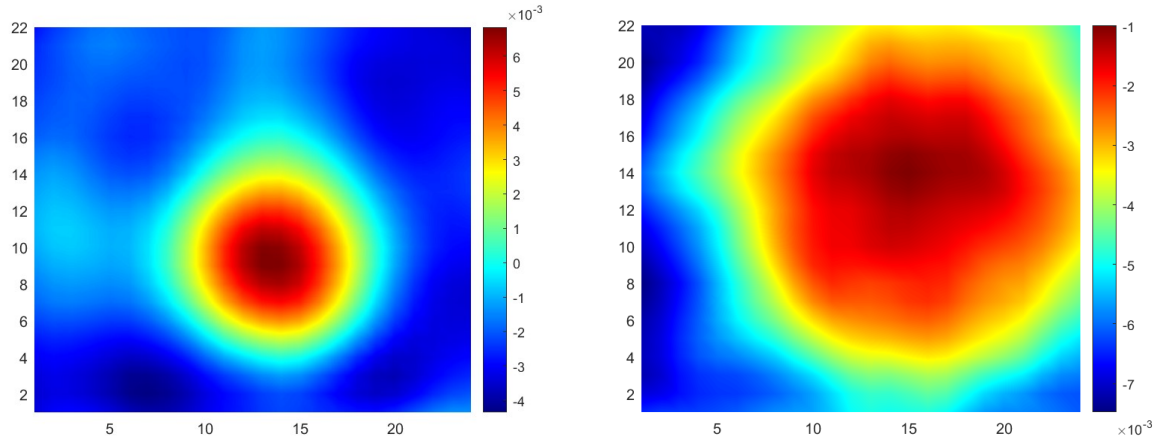

(a) (b)

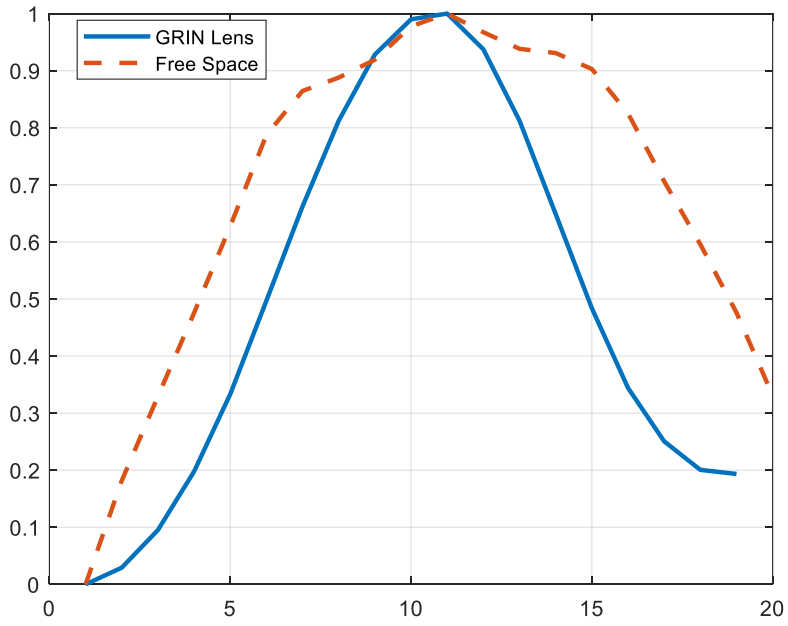

(c)

Figure 0-17 (a) Field distribution in vertical (focal) plane with lens (b) Field distribution in vertical (focal) plane with lens (c) Cross- range intensity profile comparison of lens and free space at focal plane.

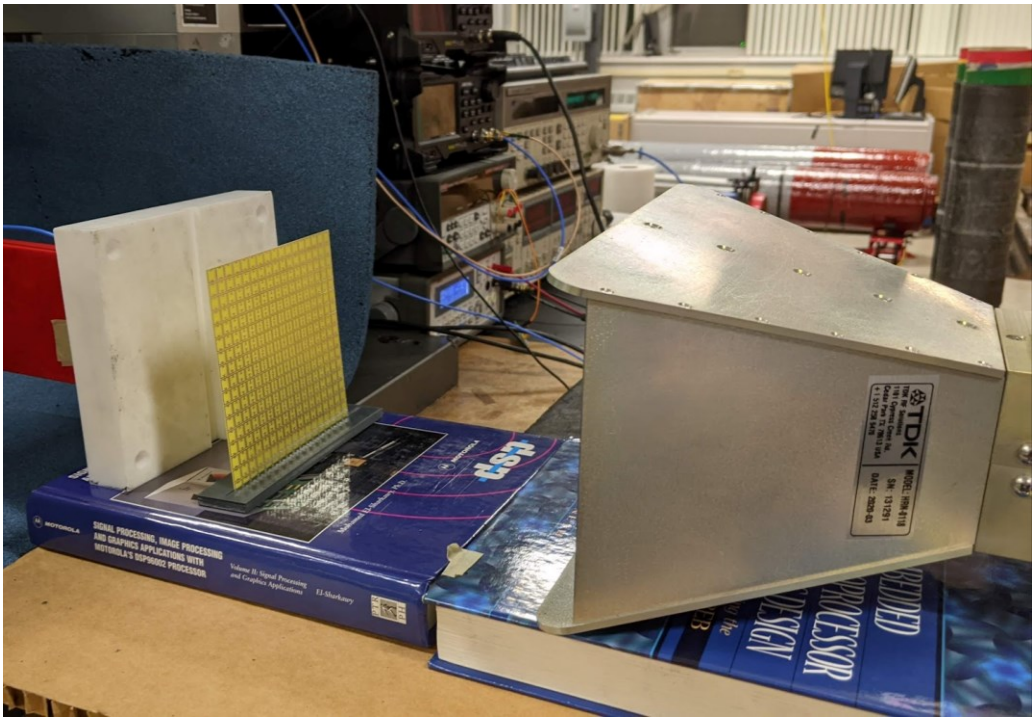

Figure 0-18 (a) Microwave NDE of groove in Teflon sample using GRIN lens

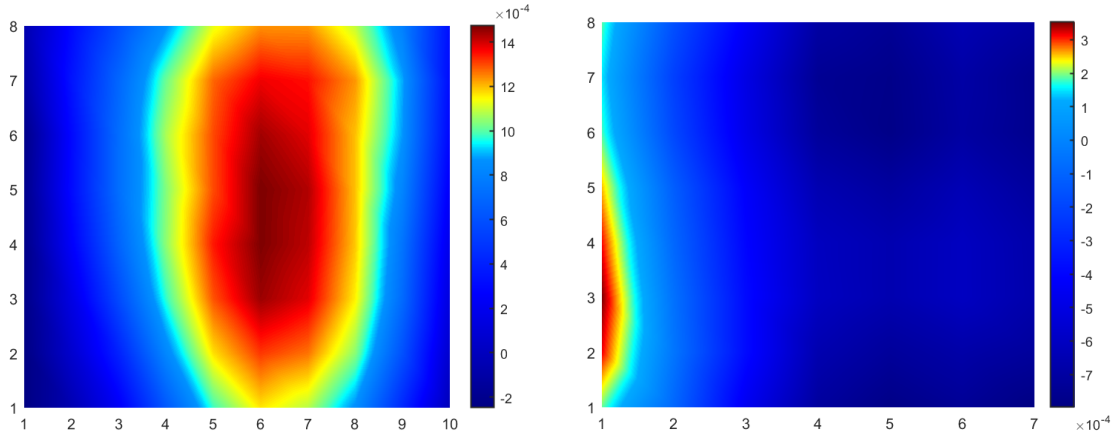

(a) (b)

Figure 0-19 NDE imaging results (a) with lens (b) without lens

Microwave NDE experiments were performed with the 2D GRIN lens to validate it's use as a imaging device. A machined groove of dimensions 15 mm x 5 mm along the length of the Teflon sample under test is treated as defect. The contributions due to the defect is measured by subtracting the signal from a similar healthy Teflon sample. The sample schematic and details is provided in section 4.3. The experiment setup is shown in Figure 5-18. The sample is located at

the focal plane of the lens. A quarter wave monopole is used to scan the vertical plane and sample the field distribution in transmission mode. The presence of the groove defect is indicated by the presence of the 1D strip maxima shown in Figure 5-19a. The experiments were performed without the lens (Figure 5-19b) to show that the groove defect can only be defected due to the resolution enhancment obtained using the proposed GRIN Metasurface lens.

This chapter presents a planar metamaterial (metasurface) lens design operating at 8 GHz. This lens does not operate on the principle of negative index metamaterials, but rather is a gradient-index lens, with a spatially varying refractive index perpendicular to the direction of propagation. The advantages of the gradient index lens over negative index lens are that the former is planar (more compact) wideband and can provide relatively larger source to focal point distances, which is not limited by the thickness of the lens.

Additional validation studies in this area involves the fabrication and experimental implementation of the proposed GRIN metasurface lens. Unit cell miniaturization technique for the GRIN lens will be studied to improve the effective medium response of the metasurface design and provide a smoother GRIN profile (Figure 5-4c). The resolution enhancement obtained using the GRIN lens for microwave imaging of subwavelength defects will be tested to validate the approach for NDE applications. The feasibility of using the GRIN lens as a microwave hyperthermia applicator will also be studied.

SUMMARY

1.16 Concluding Remarks

Far-field microwave imaging resolution is limited by the physics of diffraction. Subwavelength features cannot be detected with such far-field sensors. Metamaterials provide a means of achieving subwavelength resolution beyond the diffraction limit at far stand-off distances. The effective negative refractive index of metamaterial lenses results in focusing of propagating waves as well as amplification of evanescent wave components. This research reports the design of two such negative index metamaterial lenses, operating at microwave S and C bands for subwavelength NDE applications. The NIM lenses consists of a periodically arranged array of unit cells of SRR and wires. Existing literature on such periodic metamaterial structures employs EM windowing techniques for experimental implementation. In this research work, a homodyne detection scheme is proposed to be used in conjunction with the lenses to provide a system to be used in the field under practical conditions. Unit cell simulation studies of the two lens designs are presented. Left-handed focusing by experiment is also demonstrated. Subwavelength imaging of source and defect is exhibited to show the capability of NIM lenses in breaking the diffraction limit.

Finally, an alternative to the SRR-wire based metamaterial design is considered since the NIM lenses considered have inherent limitations. They are lossy and bulky in nature and the point source distance from the lens is limited by its thickness (2.13). A planar gradient index metamaterial lens with ELC as its unit cells is considered as the alternative. The direction of propagation in such a ELC GRIN lens is into the plane of the unit cell. Thus, the thickness of the metamaterial lens is only limited by the thickness of the substrate and can be considered as a planar

(metasurface) lens. Engineering of flat metamaterials or metasurfaces are desirable in terms of fabrication as well as implementation. A horn antenna can be used as a source for the GRIN lens focusing action. The source distance is not theoretically limited by any parameter in contrary to the NIM lens case. Prototypes of the GRIN Metasurface lens is fabricated for experimental verification.

1.17 Contributions

- Extensive research on fundamental properties of NIM structures have been conducted over the past couple of decades. This thesis focuses on the feasibility of using a NIM lens as a NDE imaging sensor for NDE applications.
- A homodyne detection architecture was proposed in conjunction with NIM lens for imaging in the field under practical conditions. The use of synchronous detection along with the NIM lens provides a fast and high SNR imaging systemthat can be used in the field under practical conditions. According to the author's best knowledge, 2D NDE imaging results of subwavelength defects inside GFRP composites samples using NIM lenses at large stand-off distances is reported for the first time.
- Reflection mode microwave NDE results of subwavelength defects is reported for the first time in literature. Reflection mode imaging provides a practical system that can be deployed in the field when there is only single side access to the samples under test.
- An alternative metamaterial lens design consisting of ELC unit cells is studied. Research on GRIN lens designs have been conducted mostly in the optical and THz regime. This thesis proposes a GRIN lens design at microwave frequencies. A novel microwave NDE method using GRIN lens design is proposed.

- This thesis looks at the topic of metamaterials and metasurfaces and provides a comparative study of their performance in the context of microwave imaging. Such a comprehensive study of metamaterials is done for the first time. Comments on the strengths and weaknesses of metamaterials and metasurfaces are presented to provide a holistic view on the subject.

1.18 Future work

As part of future study, unit cell miniaturization techniques will be considered since it will improve the effective medium response of the periodic metamaterial structures. An electromagnetic metamaterial is an engineered composite material comprising a periodic array of unit cells. These unit cells collectively exhibit macroscopically observed effective values of ϵ and μ that are not found in naturally occuring materials. For metamaterials to function properly, they must be operated in the effective-medium regime, i.e., the lattice constant or unit cell size should be much smaller than λ/4, where λ is the homogenized wavelength in the effective medium [52]. Under this condition a collection of metamaterial elements appears nearly homogeneous to incident waves and can be characterized by an effective ϵ and μ as discussed in the report. As the unit cell size approaches λ/4, diffraction effects become significant. These effects are detrimental to the performance of effective medium metamaterials in quasi-optical applications [76]. When the unit cell size is comparable to or larger than a quarter-wavelength, the effective material parameters lose their relevance [77].

Several approaches can be implemented to increase the effective medium ratio, for various types of metamaterial unit cells. These approaches are based on the idea of raising the overall inductance and capacitance of the unit cell structures, which results in decrease in their resonating frequencies (which in turn increases the effective medium wavelength). One way of achieving this

is to change the feature sizes of the structure, i.e., shorten gaps or lengthen wires to increase the capacitance and inductance, respectively. However, the realization of this approach can be limited by fabrication tolerances. As an alternative, increasing the permittivity or permeability of the dielectric substrate leads to a larger effective capacitance or inductance [77]. Another way is to integrate a surface-mounted capacitor onto the unit cells. The resonant frequency of the unit cells can be tuned down significantly using this approach [78]. However, loading the structure with lumped capacitive elements complicates the fabrication process.

In this work, we propose a practical approach to increasing the effective medium ratio for the GRIN lens design. The structure proposed in this work involves replacing the normal capacitive gap in the center of a conventional ELC resonator with an interdigital capacitor (IDC), as illustrated in Figure 6-1 to increase the capacitance [79].

Essentially, IDC's are widely used as lumped elements in microwave circuits with an aim to decrease their circuit board footprint. As such, its concept well suits design of metamaterials, where the unit cell needs to be much smaller than the homogenized wavelength. The feature size of an IDC does not need to be finer than the gap width of an ordinary ELC resonator to enhance the capacitance. The single layered PCB design of IDC-loaded ELC resonators eliminates additional fabrication steps that might be required in other approaches.

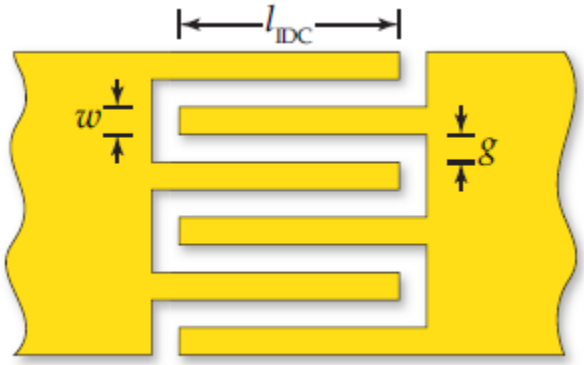

(a)

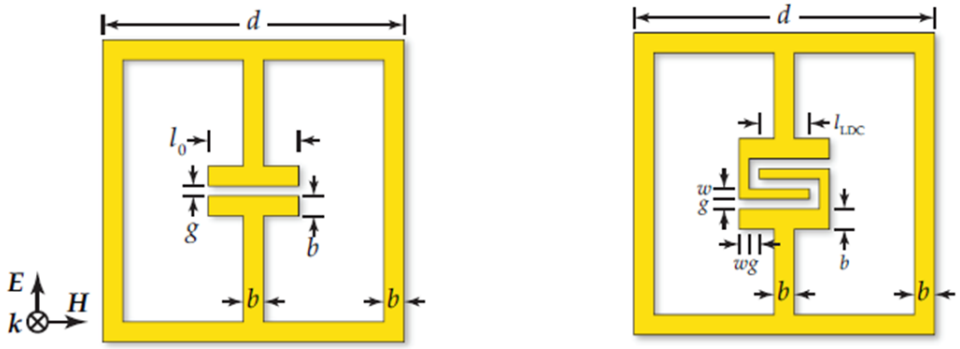

(b) (c)

Figure 0-1 (a) Inter Digital Capacitance (IDC) schematic (b) Conventional ELC unit cell (c) IDC loaded ELC unit cell [79]

Analytically, the capacitance of the IDC shown is a function of the finger length l_{IDC}, total number of fingers N, line width w, gap width g, and dielectric constant ϵ_r, as indicated in the following formula:

$$C_{IDC} = \frac{\epsilon_r 10^{-3}}{18\pi}\frac{K(k)}{K'(k)}(N-1)l_{IDC} \tag{0.1}$$

where the approximated ratio between the elliptic integrals of first kind $K(k)$ and its complement $K'(k)$ is given by equation.$k = tan^2[\frac{0.25w\pi}{w+g}]$.

An ordinary parallel-strip capacitor can be approximated as an IDC with N = 2, the capacitance of which can be deduced from Eq. (6.1) as

$$C_0 = \frac{\epsilon_r 10^{-3}}{18\pi}\frac{K(k)}{K'(k)}l_0 \tag{0.2}$$

where l_0 is the strip length as shown in figure. Provided that an IDC and a parallel-strip capacitor possess the same line width, gap width, and substrate type, their capacitances can be related through

$$C_{IDC} = (N-1)\frac{l_{IDC}}{l_0}C_0 \tag{0.3}$$

For an ELC resonator, if the inductance loop remains unchanged, it can be estimated from Eq. (6.3) that the new resonance frequency $f_{0,new}$ after IDC loading equals

$$f_{0,new} = \sqrt{\frac{l_0}{l_{IDC}(N-1)}} f_0 \tag{0.4}$$

where f_0 is the resonance frequency of a conventional ELC resonator. This simple model gives an impression for the expected change in the resonance frequency of IDC-loaded ELC resonators.

With that objective, an improved GRIN lens design with IDC loaded ELC will be numerically and experimentally studied in future work. The performance of both the conventional ELC and IDC loaded ELC design metasurface lenses for imaging purposes will be compared and presented in the future work.

Initial simulation study using Ansys HFSS was conducted to observe the effect of IDC loading in ELC unit cells. The unit cell model is shown in Figure 6-2 and the dimensions are equivalent to the one reported in section 5.2.1. An additional IDC is introduced at the center of the unit cell to observe the effect of the extra capacitance. It is observed that the resonating frequency of the nominal design is shifted from around 5.6 GHz (λ_o = 53 mm) to 3.6 GHz (λ_o = 83 mm). Hence, for the design unit cell size of a = 7 mm, the effective medium ratio (λ_o/a) improves from 7.57 to 11.85 by the introduction of the IDC at the center. Design and simulation of a metasurface lens consisting of ELC resonators must be studied in the future along with experimental verification of such a design.

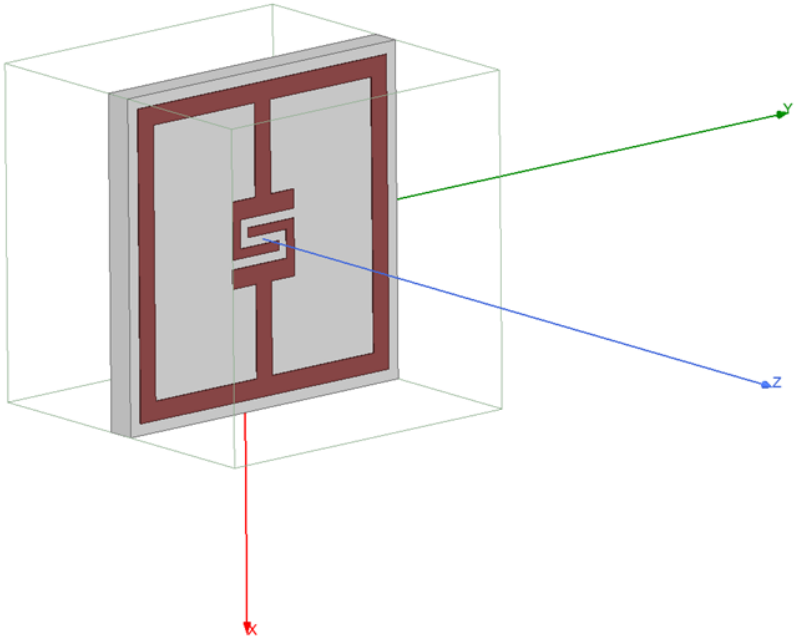

(a)

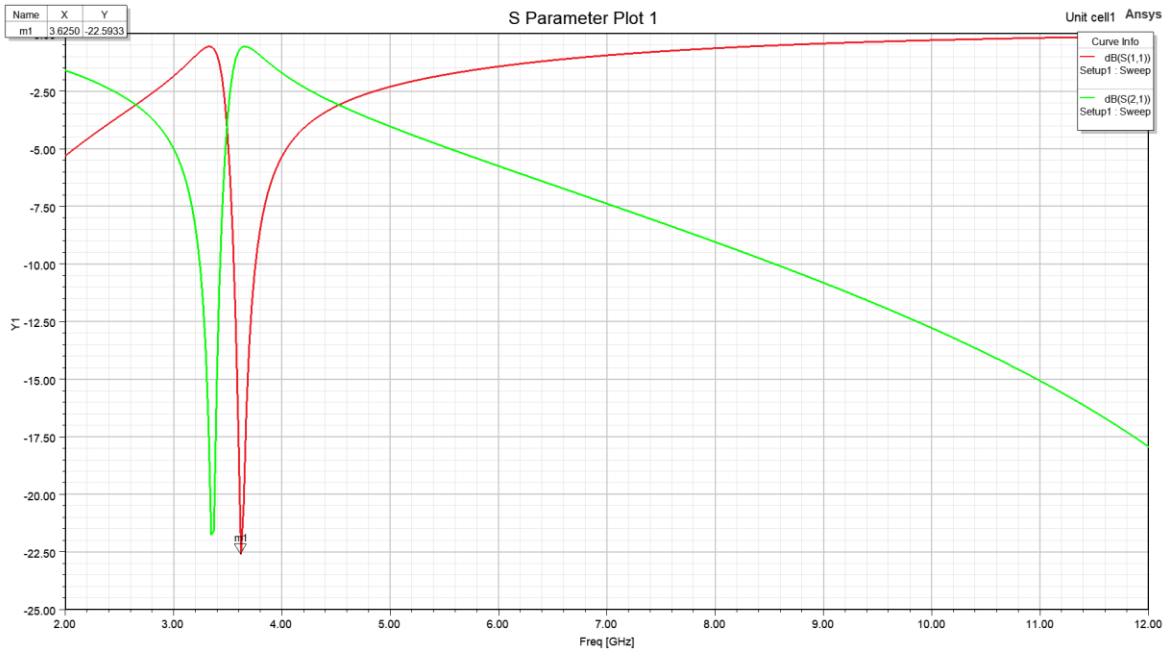

(b)

Figure 0-2 (a) Ansys HFSS unit cell model of IDC loaded ELC resonator. (b) Simulated S_{11} and S_{21}

Another possible application of GRIN lenses are for microwave hyperthermia. Hyperthermia is a technique that has gain increasing attention in the biomedical community as a complementary treatment of cancer [80]. External hyperthermia is the non-invasive alternative of

increasing the temperature of the target tissue by electromagnetic or ultrasound radiation into the affected area. In the treatment of cancer with external hyperthermia, it is desirable to apply the radiation in a localized point into the body. Tumors are heated by exposure to the radiation up to temperatures of 41º to 43º. The need for focusing a certain amount of energy into a specific area can be achieved by a dual GRIN lens system [81][82]. The amount of heat that is induced in tissues when radiated by microwaves systems is related to the Specific Absorption Rate, SAR, in (W/kg), or by the Power Loss Density, PLD, in (W/m3).

Figure 6-3 presents the dual GRIN lens approach for microwave hyperthermia. The system will consist of two planar GRIN lenses separated by a distance, *d*, see Figure 6-2. The plane wave produced by a microwave source will enter into Lens-2 and will be converted into a convergent spherical wave, whose focal length is larger than the distance separating the two lenses. The outgoing convergent spherical wave from Lens-1 is converted again into a more convergent wave by Lens-2, with an effective focal length shorter than that of both the lenses. Finally, by varying the separation *d* between the lenses, the effective focal point, F_{eff}, of the system can be controlled.

Figure 6-3 shows the dual GRIN lens approach where F_1 and F_2 are the focal lengths from Lens-1 and Lens-2, respectively. The radial axis of both lenses is aligned along the z-axis, as well as their focal points.

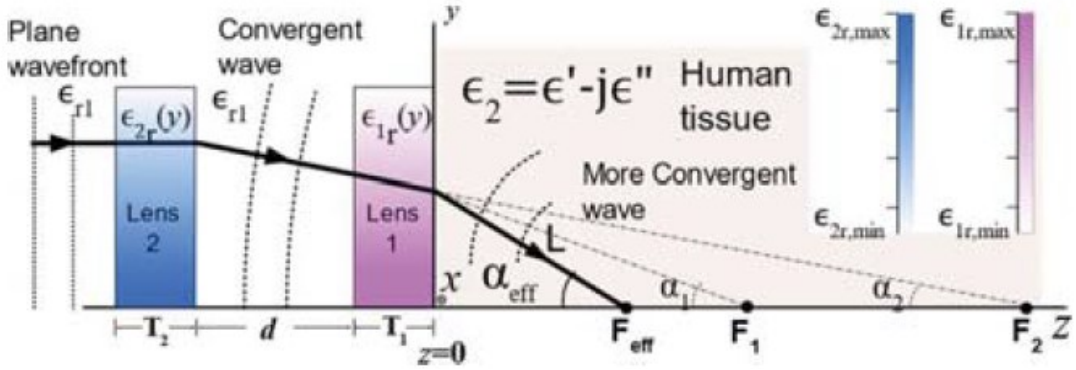

Figure 0-3 Dual GRIN lens system for Microwave Hyperthermia treatment [81].

The building blocks/unit cells of metamaterials are passive, and hence, once they are fabricated, the frequency response of metamaterials are fixed. Moreover, metamaterials work in a relatively narrow frequency regime which makes its application limited in terms of operating wavelength, λ and imaging resolution become restricted due to the narrowband nature of the NIM lens. A tunable or reconfigurable MM lens are composed of passive as well as active components. These tunable metamaterials allow greater degree of freedom in choice of operating wavelength by controlling the active components. The lens can be configured to work in a specific frequency regime depending on the composite structures under investigation. Higher frequency will allow for greater resolution of defect imaging within the structures while lower frequency allows for greater penetration. Work on developing and modifying metmaterial lens designs to make them tunable will be conducted under this major task. One of the approaches involving the previously discussed unit cell design is discussed below.

Split ring resonators (SRR) of unit cells can be modelled as a LC tank circuit, where the capacitance is given by the splits in the rings while the inductance is offered by the rings themselves. Figure 6-4 shows the circuit diagram of an SRR as a LC tank circuit.

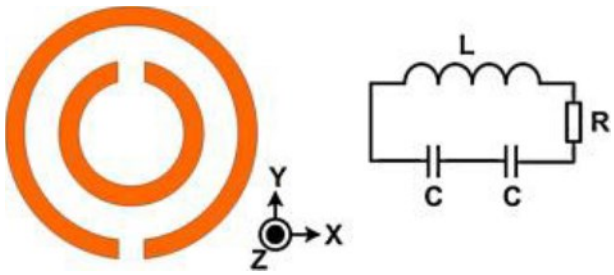

Figure 0-4 Circuit diagram of SRR unit cell as LC tank.

The resonant frequency of the split ring resonator is given by equation, $\omega_0 = \frac{2\pi}{\sqrt{LC}}$, where, L is the average inductance given by the rings and C is the capacitance due to the splits and the gap of the rings. When external capacitance is introduced in the SRR, the resonant frequency is shifted. Since the negative refractive index of the metamaterial occurs around this

resonant frequency, we can effectively change the frequency of operation of the NIM Lens by varying the external capacitance. Numerical simulations were done by loading the outer split of the SRR with an external capacitor to study its effect in changing the operating frequency.

Three case studies were conducted by loading the SRR unit cell with capacitor at three possible locations: inner split, outer split and the gap between the rings. The HFSS model for the three cases are shown in Figure 6-5. Parametric study for the three cases using various capacitance value was investigated to study the effect of tuning. The capacitance value is swept from 0.1 pF to 5 pF and the corresponding results for the three cases are plotted in Figure 6-6. It can be observed that the surface mount capacitor when placed at the outer split provides maximum tunability. This can be understood from the electric field distribution of a SRR unit cell. The simulated electric field distribution of a unit cell without any capacitor loading is presented in Figure 6-7a. The strongest electric field is at the outer split, thus corresponding to maximum tunability achieved when tunable capacitance is placed at the split of the outer ring. The comparison of change in resonant frequency for the two cases is shown in Figure 6-7b. Future work will involve the experimental implementation of such tunable unit cells to fabricate active metamaterial lenses for microwave imaging.

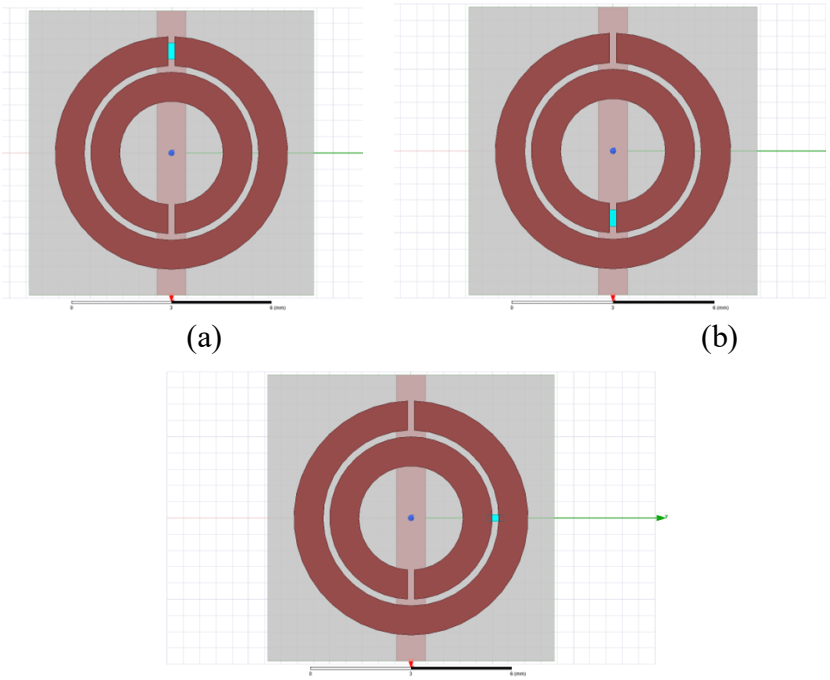

Figure 0-5 SRR unit cell model with capacitor loading at (a) outer split (b) inner split (c) gap.

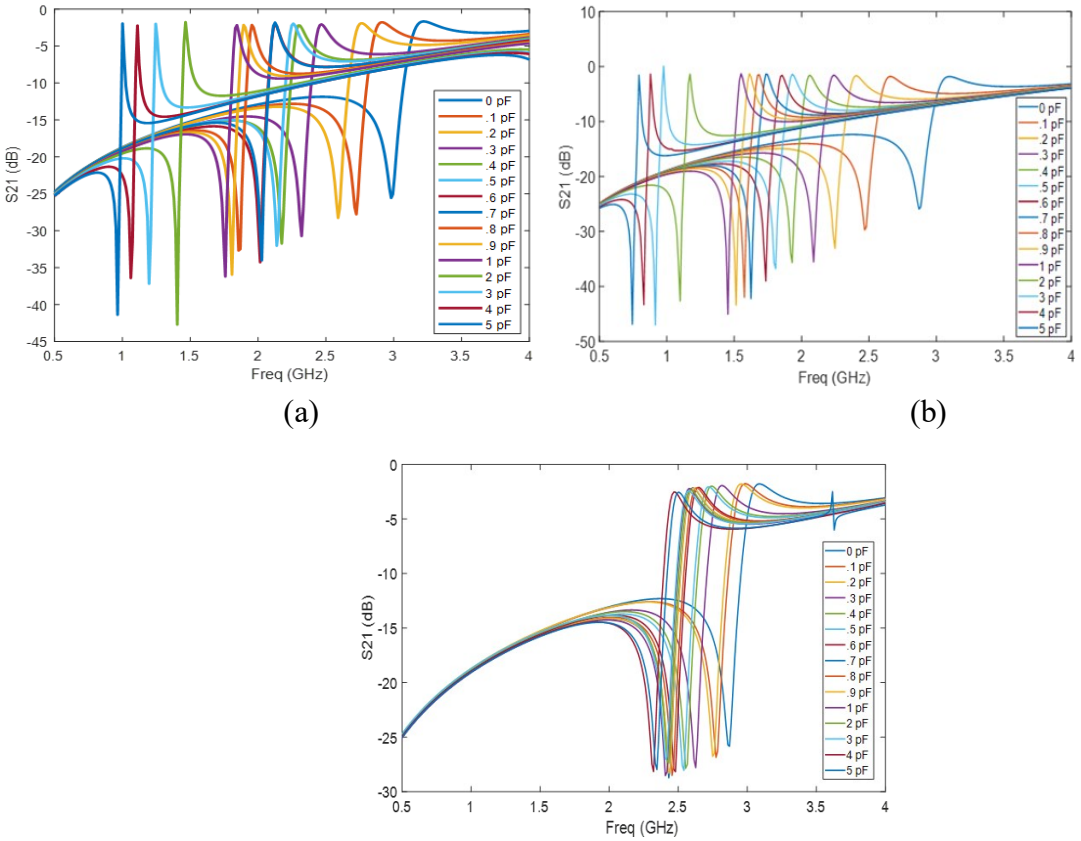

(a) (b)

(c)

Figure 0-6 Resonant peak variation with capacitance for (a) inner split case (b) outer split case (c) gap case.

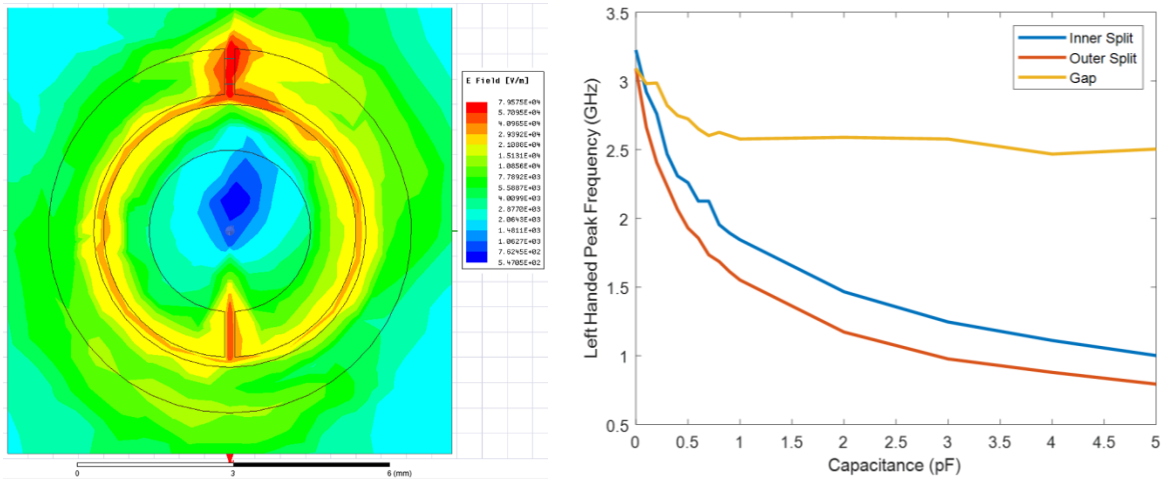

(a) (b)

Figure 0-7 (a) Electric field distribution of SRR unit cell (b) Variation of resonant frequency with tuning capacitor.

Finally, future work to investigate a more general approach to design of metamaterials will be undertaken. In current practice, the design of metamaterials relies on a trial-and-error process, usually involving numerical methods such as Finite-Difference-Time-Domain (FDTD) or Finite Element Method (FEM) to iteratively solve the appropriate Maxwell's equations. Therefore, development of new metamaterials designs with a set goal of performance characteristics tends to be a cumbersome process. It is proposed that exploring inverse design approaches to generate new metamaterial designs by optimizing an objective function describing the desired performance can have potential applications [83]. Data-driven methods based on machine learning (ML) solve the optimization problem from statistical perspectives, unlike numerical calculations. This will expedite the design of new metamaterial lenses and could provide with multiple designs for similar set of properties.

REFERENCES

[1] M. Ahadi, M. Isa, M. I. Saripan, and W. Z. W. Hasan, "Three dimensions localization of tumors in confocal microwave imaging for breast cancer detection," *Microw. Opt. Technol. Lett.*, vol. 57, no. 12, pp. 2917–2929, 2015, doi: 10.1002/mop.29470.

[2] I. J. E. Bridges *et al.*, "United States Patent (19)," no. 19, 2000.

[3] A. J. Witten, J. E. Molyneux, and J. E. Nyquist, "Ground Penetrating Radar Tomography: Algorithms and Case Studies," *IEEE Trans. Geosci. Remote Sens.*, vol. 32, no. 2, pp. 461–467, 1994, doi: 10.1109/36.295060.

[4] B. Panzner, A. Joestingmeier, and A. Omar, "Ka-band dielectric lens antenna for resolution enhancement of a GPR," *ISAPE 2008 - 8th Int. Symp. Antennas, Propag. EM Theory Proc.*, pp. 31–34, 2008, doi: 10.1109/ISAPE.2008.4735132.

[5] D. M. Sheen, D. L. McMakin, and T. E. Hall, "Three-dimensional millimeter-wave imaging for concealed weapon detection," *IEEE Trans. Microw. Theory Tech.*, vol. 49, no. 9, pp. 1581–1592, 2001, doi: 10.1109/22.942570.

[6] M. Q. Feng, F. De Flaviis, and Y. J. Kim, "Use of Microwaves for Damage Detection of Fiber Reinforced Polymer-Wrapped Concrete Structures," *J. Eng. Mech.*, vol. 128, no. 2, pp. 172–183, 2002, doi: 10.1061/(asce)0733-9399(2002)128:2(172).

[7] A. J. Bahr, "Experimental Techniques in Microwave NDE," vol. 14, pp. 593–600, 1995.

[8] S. Kharkovsky and R. Zoughi, "Microwave and millimeter wave nondestructive testing and evaluation- overview and recent advances," *IEEE Instrum. Meas. ...*, no. April, 2007, [Online]. Available: http://www.researchgate.net/publication/3421067_Microwave_and_millimeter_wave_nondestructive_testing_and_evaluation_-_Overview_and_recent_advances/file/3deec52002717b46d4.pdf.

[9] X. D. Xiang and C. Gao, "Quantitative complex electrical impedance microscopy by scanning evanescent microwave microscope," *Mater. Charact.*, vol. 48, no. 2–3, pp. 117–125, 2002, doi: 10.1016/S1044-5803(02)00277-2.

[10] C. P. Vlahacos, R. C. Black, S. M. Anlage, A. Amar, and F. C. Wellstood, "Near-field scanning microwave microscope with 100 μm resolution," *Appl. Phys. Lett.*, vol. 69, no. 21, pp. 3272–3274, 1996, doi: 10.1063/1.118033.

[11] L. Markley and G. V. Eleftheriades, "Two-dimensional subwavelength-focused imaging using a near-field probe at a λ/4 working distance," *J. Appl. Phys.*, vol. 107, no. 9, 2010, doi: 10.1063/1.3407518.

[12] R. K. Raney, "Synthetic Aperture Imaging Radar and Moving Targets," *IEEE Trans. Aerosp. Electron. Syst.*, vol. AES-7, no. 3, pp. 499–505, 1971, doi: 10.1109/TAES.1971.310292.

[13] C. G. Stephanis and G. D. Hampsas, “Imaging with Microwave Lens,” *IEEE Trans. Antennas Propag.*, vol. 28, no. 1, pp. 49–52, 1980, doi: 10.1109/TAP.1980.1142287.

[14] M. Cheney and B. Borden, “Problems in synthetic-aperture radar imaging,” *Inverse Probl.*, vol. 25, 2009, doi: 10.1088/0266-5611/25/12/123005.

[15] S. Mukherjee, A. Tamburrino, M. Haq, S. Udpa, and L. Udpa, “Far field microwave NDE of composite structures using time reversal mirror,” *NDT E Int.*, vol. 93, no. September 2017, pp. 7–17, 2018, doi: 10.1016/j.ndteint.2017.09.008.

[16] S. Mukherjee, X. Shi, Y. Deng, and L. Udpa, “A Hybrid Microwave NDE System for Rapid Inspection of GFRP Composites,” *Mater. Eval.*, vol. 78, no. 8, pp. 963–975, 2020, doi: 10.32548/2020.me-04098.

[17] A. Schuster, *An introduction to the theory of optics*. United Kingdom, 1904.

[18] V. G. Veselago, “THE ELECTRODYNAMICS OF SUBSTANCES WITH SIMULTANEOUSLY NEGATIVE VALUES OF ϵ AND μ,” *Sov. Phys. Uspekhi*, vol. 10, no. 4, pp. 509–514, Apr. 1968, doi: 10.1070/PU1968v010n04ABEH003699.

[19] L. I. Mandel’shtam, “Group velocity in crystalline arrays [in Russian],” *Zh. Eksp. Teor. Fiz*, vol. 15, pp. 475–478, 1945.

[20] D. V. Sivukhin, “The Energy of Electromagnetic Fields in Dispersive Media [in Russian],” *Opt. Spektrosk*, vol. 3, pp. 308–312, 1957.

[21] D. R. Smith, W. J. Padilla, D. C. Vier, S. C. Nemat-Nasser, and S. Schultz, “Composite Medium with Simultaneously Negative Permeability and Permittivity,” *Phys. Rev. Lett.*, vol. 84, no. 18, pp. 4184–4187, May 2000, doi: 10.1103/PhysRevLett.84.4184.

[22] J. B. Pendry, A. J. Holden, D. J. Robbins, and W. J. Stewart, “Magnetism from conductors and enhanced nonlinear phenomena,” *IEEE Trans. Microw. Theory Tech.*, vol. 47, no. 11, 1999, doi: 10.1109/22.798002.

[23] J. B. Pendry, A. J. Holden, W. J. Stewart, and I. Youngs, “Extremely low frequency plasmons in metallic mesostructures,” *Phys. Rev. Lett.*, vol. 76, no. 25, 1996, doi: 10.1103/PhysRevLett.76.4773.

[24] R. A. Shelby, D. R. Smith, and S. Schultz, “Experimental Verification of a Negative Index of Refraction,” *Science (80-.).*, vol. 292, no. 5514, pp. 77 LP – 79, Apr. 2001, doi: 10.1126/science.1058847.

[25] T. J. Cui, D. R. Smith, and R. Liu, *Metamaterials*. Boston, MA: Springer US, 2010.

[26] J. B. Pendry, “Negative refraction makes a perfect lens,” *Phys. Rev. Lett.*, vol. 85, no. 18, 2000, doi: 10.1103/PhysRevLett.85.3966.

[27] D. R. Smith, J. B. Pendry, and M. C. K. Wiltshire, “Metamaterials and negative refractive

index," *Science (80-.).*, vol. 305, no. 5685, pp. 788–792, 2004, doi: 10.1126/science.1096796.

[28] D. R. Smith, D. Schurig, M. Rosenbluth, S. Schultz, S. A. Ramakrishna, and J. B. Pendry, "Limitations on subdiffraction imaging with a negative refractive index slab," *Appl. Phys. Lett.*, vol. 82, no. 10, 2003, doi: 10.1063/1.1554779.

[29] A. Grbic and G. V. Eleftheriades, "Overcoming the Diffraction Limit with a Planar Left-Handed Transmission-Line Lens," *Phys. Rev. Lett.*, vol. 92, no. 11, 2004, doi: 10.1103/PhysRevLett.92.117403.

[30] E. Ozbay, Z. Li, and K. Aydin, "Super-resolution imaging by one-dimensional, microwave left-handed metamaterials with an effective negative index," *J. Phys. Condens. Matter*, vol. 20, no. 30, 2008, doi: 10.1088/0953-8984/20/30/304216.

[31] T. Roy, E. T. F. Rogers, and N. I. Zheludev, "Sub-wavelength focusing meta-lens," *Opt. Express*, vol. 21, no. 6, 2013, doi: 10.1364/oe.21.007577.

[32] X. Zhang and Z. Liu, "Superlenses to overcome the diffraction limit," *Nat. Mater.*, vol. 7, no. 6, pp. 435–441, 2008, doi: 10.1038/nmat2141.

[33] L. Leggio, E. Dadrasnia, and O. de Varona, "Microwave focusing within arbitrary refractive index media using left-handed metamaterial lenses," *Prog. Electromagn. Res. M*, vol. 45, 2016, doi: 10.2528/PIERM15072807.

[34] J. J. Chen, T. M. Grzegorczyk, B.-I. Wu, and J. A. Kong, "Limitation of FDTD in simulation of a perfect lens imaging system," *Opt. Express*, vol. 13, no. 26, 2005, doi: 10.1364/opex.13.010840.

[35] P. Tassin, I. Veretennicoff, and G. Van der Sande, "Veselago's lens consisting of left-handed materials with arbitrary index of refraction," *Opt. Commun.*, vol. 264, no. 1, 2006, doi: 10.1016/j.optcom.2006.02.013.

[36] S. Mukherjee, X. Shi, L. Udpa, S. Udpa, Y. Deng, and P. Chahal, "Design of a Split-Ring Resonator Sensor for Near-Field Microwave Imaging," *IEEE Sens. J.*, vol. 18, no. 17, 2018, doi: 10.1109/JSEN.2018.2852657.

[37] E. L. Chuma, Y. Iano, G. Fontgalland, and L. L. Bravo Roger, "Microwave sensor for liquid dielectric characterization based on metamaterial complementary split ring resonator," *IEEE Sens. J.*, vol. 18, no. 24, pp. 9978–9983, 2018, doi: 10.1109/JSEN.2018.2872859.

[38] A. Ali, M. El Badawe, and O. M. Ramahi, "Microwave Imaging of Subsurface Flaws in Coated Metallic Structures Using Complementary Split-Ring Resonators," *IEEE Sens. J.*, vol. 16, no. 18, pp. 6890–6898, 2016, doi: 10.1109/JSEN.2016.2587738.

[39] M. Puentes, M. Scḧußler, A. Penirschke, C. Damm, and R. Jakoby, "Metamaterials in microwave sensing applications," *Proc. IEEE Sensors*, no. 1, pp. 2166–2171, 2010, doi: 10.1109/ICSENS.2010.5690570.

[40] R. Melik, E. Unal, N. K. Perkgoz, C. Puttlitz, and H. V. Demir, “Metamaterial-based wireless strain sensors Metamaterial-based wireless strain sensors,” *Proc. IEEE Sensors*, vol. 011106, no. 2009, pp. 2173–2176, 2014.

[41] A. Ebrahimi, W. Withayachumnankul, S. Al-Sarawi, and D. Abbott, “High-sensitivity metamaterial-inspired sensor for microfluidic dielectric characterization,” *IEEE Sens. J.*, vol. 14, no. 5, pp. 1345–1351, 2014, doi: 10.1109/JSEN.2013.2295312.

[42] M. Tabib-Azar and M. A. H. Chowdhury, “A 10 GHz metamaterial sensor to detect SARS COV-2 and dust particles in free space,” *IEEE Sens. J.*, vol. 22, no. 13, pp. 12846–12851, 2022, doi: 10.1109/JSEN.2022.3178049.

[43] A. Savin, A. Bruma, R. Steigmann, N. Iftimie, and D. Faktorova, “Enhancement of spatial resolution using a metamaterial sensor in nondestructive evaluation,” *Appl. Sci.*, vol. 5, no. 4, 2015, doi: 10.3390/app5041412.

[44] D. Shreiber, M. Gupta, and R. Cravey, “Microwave nondestructive evaluation of dielectric materials with a metamaterial lens,” *Sensors Actuators, A Phys.*, vol. 144, no. 1, 2008, doi: 10.1016/j.sna.2007.12.031.

[45] D. C. Noll, D. G. Nishimura, and A. Macovski, “Homodyne Detection in Magnetic Resonance Imaging,” *IEEE Trans. Med. Imaging*, vol. 10, no. 2, pp. 154–163, 1991, doi: 10.1109/42.79473.

[46] B. A. Munk, *Metamaterials: Critique and Alternatives*. Wiley, 2009.

[47] P. M. Valanju, R. M. Walser, and A. P. Valanju, “Wave Refraction in Negative-Index Media: Always Positive and Very Inhomogeneous,” *Phys. Rev. Lett.*, vol. 88, no. 18, p. 187401, Apr. 2002, doi: 10.1103/PhysRevLett.88.187401.

[48] A. A. Houck, J. B. Brock, and I. L. Chuang, “Experimental Observations of a Left-Handed Material That Obeys Snell’s Law,” *Phys. Rev. Lett.*, vol. 90, no. 13, p. 137401, Apr. 2003, doi: 10.1103/PhysRevLett.90.137401.

[49] K. Aydin, K. Guven, M. Kafesaki, L. Zhang, C. M. Soukoulis, and E. Ozbay, “Experimental observation of true left-handed transmission peaks in metamaterials,” *Opt. Lett.*, vol. 29, no. 22, p. 2623, Nov. 2004, doi: 10.1364/OL.29.002623.

[50] K. Aydin, K. Guven, C. M. Soukoulis, and E. Ozbay, “Observation of negative refraction and negative phase velocity in left-handed metamaterials,” *Appl. Phys. Lett.*, vol. 86, no. 12, p. 124102, Mar. 2005, doi: 10.1063/1.1888051.

[51] A. Alù, “First-principles homogenization theory for periodic metamaterials,” *Phys. Rev. B - Condens. Matter Mater. Phys.*, vol. 84, no. 7, 2011, doi: 10.1103/PhysRevB.84.075153.

[52] B. A. Slovick, Z. G. Yu, and S. Krishnamurthy, “Generalized effective-medium theory for metamaterials,” *Phys. Rev. B - Condens. Matter Mater. Phys.*, vol. 89, no. 15, 2014, doi: 10.1103/PhysRevB.89.155118.

[53] K. Li, S. J. McLean, R. B. Greegor, C. G. Parazzoli, and M. H. Tanielian, “Free-space focused-beam characterization of left-handed materials,” *Appl. Phys. Lett.*, vol. 82, no. 15, pp. 2535–2537, 2003, doi: 10.1063/1.1567454.

[54] E. Ozbay, K. Aydin, E. Cubukcu, and M. Bayindir, “Transmission and reflection properties of composite metamaterials in free space,” *IEEE Trans. Antennas Propag.*, vol. 51, no. 10, pp. 2592–2595, 2003.

[55] K. Aydin, I. Bulu, and E. Ozbay, “Focusing of electromagnetic waves by a left-handed metamaterial flat lens,” *Opt. Express*, vol. 13, no. 22, 2005, doi: 10.1364/opex.13.008753.

[56] M. Gokkavas *et al.*, “Experimental demonstration of a left-handed metamaterial operating at 100 GHz,” *Phys. Rev. B - Condens. Matter Mater. Phys.*, vol. 73, no. 19, pp. 4–7, 2006, doi: 10.1103/PhysRevB.73.193103.

[57] V. A. Podolskiy and E. E. Narimanov, “Near-sighted superlens,” vol. 30, no. 1, pp. 75–77, 2005.

[58] S. Datta *et al.*, “Negative index metamaterial lens for subwavelength microwave detection,” *Sensors*, vol. 21, no. 14, pp. 1–16, 2021, doi: 10.3390/s21144782.

[59] S. Datta, X. Shi, S. Mukherjee, Y. Deng, and L. Udpa, “Model-Based Study of a Metamaterial Lens for Nondestructive Evaluation of Composites,” *J. Nondestruct. Eval. Diagnostics Progn. Eng. Syst.*, vol. 3, no. 4, 2020, doi: 10.1115/1.4047027.

[60] A. M. Nicolson and G. F. Ross, “Measurement of the Intrinsic Properties Of Materials by Time-Domain Techniques,” *IEEE Trans. Instrum. Meas.*, vol. 19, no. 4, 1970, doi: 10.1109/TIM.1970.4313932.

[61] W. B. Weir, “Automatic Measurement of Complex Dielectric Constant and Permeability at Microwave Frequencies,” *Proc. IEEE*, vol. 62, no. 1, 1974, doi: 10.1109/PROC.1974.9382.

[62] X. Chen, T. M. Grzegorczyk, B. I. Wu, J. Pacheco, and J. A. Kong, “Robust method to retrieve the constitutive effective parameters of metamaterials,” *Phys. Rev. E - Stat. Physics, Plasmas, Fluids, Relat. Interdiscip. Top.*, vol. 70, no. 1, 2004, doi: 10.1103/PhysRevE.70.016608.

[63] S. Arslanagić *et al.*, “A review of the scattering-parameter extraction method with clarification of ambiguity issues in relation to metamaterial homogenization,” *IEEE Antennas Propag. Mag.*, vol. 55, no. 2, 2013, doi: 10.1109/MAP.2013.6529320.

[64] E. J. Rothwell, J. L. Frasch, S. M. Ellison, P. Chahal, and R. O. Ouedraogo, “Analysis of the Nicolson-Ross-Weir method for characterizing the electromagnetic properties of engineered materials,” *Prog. Electromagn. Res.*, vol. 157, 2016, doi: 10.2528/PIER16071706.

[65] H. Ku, H. Wang, N. Pattarachaiyakoop, and M. Trada, “A review on the tensile properties of natural fiber reinforced polymer composites,” *Compos. Part B Eng.*, vol. 42, no. 4, pp.

856–873, 2011, doi: 10.1016/j.compositesb.2011.01.010.

[66] L. Mohammed, M. N. M. Ansari, G. Pua, M. Jawaid, and M. S. Islam, “A Review on Natural Fiber Reinforced Polymer Composite and Its Applications,” *Int. J. Polym. Sci.*, vol. 2015, 2015, doi: 10.1155/2015/243947.

[67] C. Soutis, “Fibre reinforced composites in aircraft construction,” *Prog. Aerosp. Sci.*, vol. 41, no. 2, pp. 143–151, 2005, doi: 10.1016/j.paerosci.2005.02.004.

[68] K. Senthil, A. Arockiarajan, R. Palaninathan, B. Santhosh, and K. M. Usha, “Defects in composite structures: Its effects and prediction methods - A comprehensive review,” *Compos. Struct.*, vol. 106, pp. 139–149, 2013, doi: 10.1016/j.compstruct.2013.06.008.

[69] D. R. Smith, J. J. Mock, A. F. Starr, and D. Schurig, “Gradient index metamaterials,” *Phys. Rev. E - Stat. Nonlinear, Soft Matter Phys.*, vol. 71, no. 3, pp. 1–6, 2005, doi: 10.1103/PhysRevE.71.036609.

[70] D. Schurig, J. J. Mock, and D. R. Smith, “Electric-field-coupled resonators for negative permittivity metamaterials,” *Appl. Phys. Lett.*, vol. 88, no. 4, pp. 1–3, 2006, doi: 10.1063/1.2166681.

[71] W. J. Padilla, M. T. Aronsson, C. Highstrete, M. Lee, A. J. Taylor, and R. D. Averitt, “Electrically resonant terahertz metamaterials: Theoretical and experimental investigations,” *Phys. Rev. B - Condens. Matter Mater. Phys.*, vol. 75, no. 4, pp. 1–4, 2007, doi: 10.1103/PhysRevB.75.041102.

[72] O. Quevedo-Teruel *et al.*, “Roadmap on metasurfaces,” *J. Opt. (United Kingdom)*, vol. 21, no. 7, 2019, doi: 10.1088/2040-8986/ab161d.

[73] D. Kitayama, M. Yaita, and H.-J. Song, “Laminated metamaterial flat lens at millimeter-wave frequencies,” *Opt. Express*, vol. 23, no. 18, p. 23348, 2015, doi: 10.1364/oe.23.023348.

[74] P. Pushkar and V. R. Gupta, “A design rule for an ELC resonator,” *ICIIECS 2015 - 2015 IEEE Int. Conf. Innov. Information, Embed. Commun. Syst.*, pp. 17–20, 2015, doi: 10.1109/ICIIECS.2015.7193147.

[75] J. W. Allen and B.-I. Wu, “Design and fabrication of an RF GRIN lens using 3D printing technology,” *Terahertz, RF, Millimeter, Submillimeter-Wave Technol. Appl. VI*, vol. 8624, p. 86240V, 2013, doi: 10.1117/12.2000708.

[76] T. Koschny, P. Markoš, E. N. Economou, D. R. Smith, D. C. Vier, and C. M. Soukoulis, “Impact of inherent periodic structure on effective medium description of left-handed and related metamaterials,” *Phys. Rev. B - Condens. Matter Mater. Phys.*, vol. 71, no. 24, pp. 1–22, 2005, doi: 10.1103/PhysRevB.71.245105.

[77] C. Caloz, A. Lai, and T. Itoh, “The challenge of homogenization in metamaterials,” *New J. Phys.*, vol. 7, 2005, doi: 10.1088/1367-2630/7/1/167.

[78] K. Aydin and E. Ozbay, “Capacitor-loaded split ring resonators as tunable metamaterial components,” *J. Appl. Phys.*, vol. 101, no. 2, 2007, doi: 10.1063/1.2427110.

[79] W. Withayachumnankul, C. Fumeaux, and D. Abbott, “Compact electric-LC resonators for metamaterials,” *Opt. Express*, vol. 18, no. 25, p. 25912, 2010, doi: 10.1364/oe.18.025912.

[80] I. Toseroni, S. Ciampa, and M. Cavagnaro, “Human body models for validation studies of deep hyperthermia,” *Int. J. RF Microw. Comput. Eng.*, vol. 28, no. 3, 2018, doi: 10.1002/mmce.21207.

[81] F. Albarracin-Vargas, F. Vega, C. Kasmi, F. Alyafei, and C. Baer, “Dual Graded Index Dielectric Lens System for Hyperthermia,” *2020 33rd Gen. Assem. Sci. Symp. Int. Union Radio Sci. URSI GASS 2020*, no. September, pp. 2–5, 2020, doi: 10.23919/URSIGASS49373.2020.9232223.

[82] S. Zhang, R. K. Arya, S. Pandey, Y. Vardaxoglou, W. Whittow, and R. Mittra, “3D-printed planar graded index lenses,” *IET Microwaves, Antennas Propag.*, vol. 10, no. 13, pp. 1411–1419, 2016, doi: 10.1049/iet-map.2016.0013.

[83] W. Ma, F. Cheng, Y. Xu, Q. Wen, and Y. Liu, “Probabilistic Representation and Inverse Design of Metamaterials Based on a Deep Generative Model with Semi-Supervised Learning Strategy,” *Adv. Mater.*, vol. 31, no. 35, pp. 1–9, 2019, doi: 10.1002/adma.201901111.